Simultaneous Multispectral Imaging: Using Multiview Computational Compressive Sensing

by

Farnoud Kazemzadeh

A thesis
presented to the University of Waterloo
in fulfillment of the
thesis requirement for the degree of
Doctor of Philosophy
in
Systems Design Engineering

Waterloo, Ontario, Canada, 2016

I hereby declare that I am the sole author of this thesis. This is a true copy of the thesis, including any required final revisions, as accepted by my examiners.

I understand that my thesis may be made electronically available to the public.

Abstract

Multispectral imaging is traditionally performed using a combination of an imaging device with a filter bank such as a filter wheel or a form of tunable filter, or a combination of many imaging devices with various spectral beam splitting optics. The complexity and size of these devices seem to be the limiting factor of their adoption and use in various fields that could potentially benefit from this imaging modality. With the advent of nanophotonics, there has been a surge in single camera, snapshot, multispectral imaging exploiting the capabilities of nanotechnology to devise pixel-based spectral filters. This new form of sensing, which can be classified as compressive sensing, has its limitations. One example is the laborious process of fabricating the filter bank and installing it into a detector since the detector fabrication process is completely removed from the filter fabrication process.

The work presented here will describe an optical design that would enable a single-camera, simultaneous multispectral imaging via multiview computational compressive sensing. A number of points-of-view (POVs) of the field-of-view (FOV) of the camera are generated and directed through an assortment of spectral pre-filters en route to the camera. The image of each of the POVs is then captured on a different spatial location on the detector. With the spectral response of the detector pixels well characterized, spatial and spectral compressive sensing is performed as the images are recorded. Various computational techniques are used in this work which would: register the images captured from multiple views resulting in even more sparsely sensed images; perform spatial interpolation of the sparsely sampled spectral images; implement hyper-focusing of the images from all POVs captured as some defocusing will happen as the result of the discrepancy in the optical paths in each view; execute numerical dimensionality reduction analysis to extract information from the multispectral images.

The spectral imaging capabilities of the device are tested with a collection of fluorescent microspheres. The spectral sensing capability of the device is examined by measuring the fluorescent spectra of adulterated edible oils and demonstrating the ability of the imaging system to differentiate between various types of oil as well as various levels of contamination. Lastly, the system is used to scrutinize samples of black ink from different pen manufacturers, and is able to discriminate between the different inks.

Acknowledgments

I would like to express my gratitude to my two co-supervisors, professors David Clausi and Alexander Wong, you have both been amazing mentors for me academically, professionally, and personally. Thank you for giving me opportunities and encouraging me and allowing me to grow as a scientist, a researcher, and an academic under your guidance. David, thank you for refusing to sign my paperwork! Alex, thank you for never saying 'No' to me and letting me explore and try out all of the crazy ideas I dreamed up. I look forward to many more collaborations in the future both academically and professionally.

I would sincerely like to thank my Ph.D. committee members Dr. David Clausi and Dr. Alexander Wong from the department of Systems Design Engineering at the University of Waterloo, Dr. Simarjeet Saini, from the department of Electrical and Computer Engineering at the University of Waterloo, Dr. Kostadinka Bizheva and Dr. Brian McNamara, from the department of Physics and Astronomy at the University of Waterloo, as well as Dr. Qiyin Fang, from the department of Engineering Physics at McMaster University for their time and commitment. Your valuable insight and guidance has improved the quality of my thesis and made me a better scientist.

Many thanks to Dr. Monica Emelko from the department of Civil and Environmental Engineering at the University of Waterloo for allowing me the use of her research laboratory along with the specialized equipment required to carry out some of the studies in this thesis. Special thanks to Dr. Chao Jin and soon-to-be-doctor Mr. Iman Khodadad for their help and guidance in preparation of some of the fluorescent samples used in this thesis.

Many thanks to the various individuals in the University of Waterloo Engineering Machine Shop for their help and guidance regarding design and manufacturing of products over the past few years. I would specifically like to thank Mr. Rick Forgett for always making himself available to help and guide me. Rick I hope cutting expensive optics equipment, manually, was as enjoyable for you as it was for me.

To my colleagues in the Vision and Image Processing lab at the University of Waterloo: I have cherished my time in the lab together with you, thank you for your commitment to science and engineering and for the culture of productivity and constant challenge. It's OK, we will move eventually!

To Dr. Brian McNamara and Dr. Gretchen Harris, even though my research interests diverted from looking for and solving the questions about our universe, I want you to know that at heart, I am still an Astrophysicist. I thank you for your support and encouragement over the past 10 years and I look forward to many more years of collaboration and friendship.

Lastly, but most importantly, I would like to thank my family for all of their love and encouragement. To my parents, Kazem and Farjam, who raised me with a love for knowledge and instilled in me the drive and perseverance to always strive to be the best. To my brother, Behnoud, who has always been a breath of fresh air when I needed it. To my son, Emmett, for being an uplifting and rejuvenating part of my life for as long as you have been in this world. And most of all to the love of my life, my rock, and my best friend, my wife Nicole, who has stuck with me through thick and thin and around the world, literally, encouraging me and allowing me to pursue my dreams and supporting me in every way so I could accomplish the lofty goals I set out for myself.

Thank you.

Dedication

I dedicate this work to my wife and son.

Table of Contents

List of Tables

List of Figures

Nomenclature

α	Angle of incidence of a beam of light and a diffraction grating with respect to the surface normal
β	Angle between the transmitted beam of light and a diffraction grating with respect to the surface normal
$\epsilon_r(\lambda)$	Relative electric permittivity
$\hat{f}$	The most probable desired hyper-focused image
κ	Molar extinction coefficient
Λ	A set of eigenvalues
$\mathfrak{F}^{-1}$	Inverse Fourier transform
$\mathfrak{F}$	Forward Fourier transform
$\mathfrak{f}$	The desired hyper-focused image
$\mathfrak{m}$	Ratio of the complex refractive index of a particle to the complex refractive index of the medium
$\mathfrak{S}$	A set of pixel locations in an imaging system
μ_x	Average value of image x
μ_y	Average value of image y

$\mu_r(\lambda)$	Relative magnetic permeability
$\nabla I(i,j)$	The gradient magnitude of the image I
Σ	Ideal standard deviation of the hyper-focusing PSF
$\sigma_D N$	Standard deviation in the dark noise
σ_N	Standard deviation in the number of detected photons
$\sigma_R N$	Standard deviation in the read noise
σ_x^2	Total variance in image x
σ_y^2	Total variance in image y
σ_{xy}	Covariance of two images x and y
$\mathbf{A}$	Transformation operator
$\mathbf{B}$	An image pixel
$\mathbf{f}(x_i, y_j, z_{ij})$	Original image
$\mathbf{I}$	The identity matrix
$\mathbf{T}(x_i, y_j, z_{ij})$	Transformed two-dimensional image
θ_B	Blaze angle of a diffraction grating
θ_i	Incident angle
θ_r	Reflected angle
$\widehat{I}_i$	The Stoke's vector of incident light
$\widehat{I}_s$	The Stoke's vector of scattered light
ξ^2	Variance of the nonstationary expectation
a	Radius of scattering particle

c	concentration
D	Aperture of an optical element
d	Distance between two adjacent grooves on a diffraction grating
$d\lambda$	Spectral resolution of a spectrograph
DN	Dark noise of detector pixel
$E[.]$	The expected value
f	Focal length of an optical element
$f/\#$	F-number of an optical element
f_s	Nonstationary PSF as a function of location in an image
FM_{Tenen}	The Tenengrad focus metric
G	Groove density of a diffraction grating
g	The captured defocused image
H	Ideal kernel size of the hyper-focusing PSF
H_a	The optical aberrations
I_a	Measured intensity of light after absorption
I_i	Intensity of the incident light
j	Diffraction order
m	Number of rows in a matrix
N	Total number of detected photons
n	Number of columns in a matrix
$n(\lambda)$	Refractive index

P	Mean number of detected photons
$Prob(N)$	Poisson probability distribution function
r	Distance from particle to location of observation
RN	Read noise of detector pixel
S	Covariance matrix
S_i	Size of the object being imaged
S_o	Size of the image of the object
t_e	Exposure time
w_{nm}	Generic transformation element
x_i	The i^{th} column of a matrix
y_i	The j^{th} row of a matrix
z	Distance traveled by light
CCD	Charge Coupled Device
CNR	Contrast-to-noise ratio
dSI	Discrete spectral imaging
DSLR	Digital single lens reflex
FOV	Field-of-view
FWHM	Full-width-half-maximum
LED	Light emitting diode
MAP	Maximum A Posteriori
NA	Numerical aperture of an optical element

NIR	Near infrared.
PCA	Principal component analysis
POV	Point-of-view
PSF	Point spread function
QE	Quantum efficiency
RGB	Red, green, and blue
SNR	Signal-to-noise ratio
SSIM	Structural similarity
SWIR	Short wave infrared.
UV	Ultraviolet

Chapter 1

Introduction

Imaging or digital imaging is the process of observation and recording of the intensity of the electromagnetic spectrum. Only the visible (400 - 700 nm) and the near infrared (NIR) (700 - 1100 nm) regions of the electromagnetic spectrum will be considered in the context of the work presented here. The two aforementioned regions will be referred to as 'light'. The observed or recorded intensity of light is dependent on either of the attenuation of light that interacts with an object and is reflected or scattered by it, or alternatively the intensity in the emission of light from an object. Independent of the process that makes the light available for imaging, the recorded signal can be used to extract information about an object. The recorded signal is acquired using an imaging device which includes some form of image forming, light focusing, refractive (lenses) or reflective (mirrors) component in conjunction with a pixelated detector which can discretely digitize the incoming light to which it is sensitive.

The primary colors of light - red, green, and blue - exist in the visible region of the spectrum and are responsible for the color vision of humans. Using these three spectral channels the color pigment of an object can be discerned. If the same object was observed in many more spectral channels other than the three primary channels, other information about the object could be derived. These information may include chemical composition and state variables such as temperature, pressure, etc. By going beyond the visible region and performing spectral imaging into the NIR region, other information that is not necessarily available in the visible region can be acquired.

The process of performing imaging in multiple color (spectral) channels is referred to as multispectral imaging. Usually the number of channels is limited to fewer than ten and anything beyond that number may be considered hyperspectral. The capture of multispectral images requires the use of a spectral filter accompanying an imaging device. The applications of multispectral imaging are vast and can range from astrophysics to microscopy, food processing and precision agriculture, defense and security, environmental monitoring, geological mapping, mineralogy, disaster assessment, and many more.

The process of capturing multispectral images is often sequential and there is a need to exchange spectral filters after every image acquisition. This is typically done using a rotating filter wheel containing different colored spectral filters or using an acousto-optical or liquid-crystal tunable filter. This process can be problematic if the sample is in motion or exhibits any transient properties that are of interest for observation as there is time required between each capture as the spectral filter is changing.

Simultaneous multispectral imagers exists and are often used for airborne or space borne applications. These device use a series of beamsplitting and spectral filtering optics in combination with a number of imaging devices. The number of imaging devices is proportional to the number of spectral channels required. Evidently, such devices are extremely expensive, bulky, and difficult to align and keep aligned therefore they are not easily adaptable for many applications of multispectral imaging.

The advancements in computing has given rise to a new field of sensing named compressive sensing. Compressive sensing allows for making incomplete measurements and uses advanced algorithms to complete the measurements before any formal processing can take place. In the sense of imaging this would mean only using $\sim$30% of the available pixels in a detector, randomly distributed, to perform the image acquisition and using interpolation algorithms to estimate the pixel values that are missing. This method is mainly used to speed up the data acquisition process as well as reduce the complexity of the imaging device.

Recently, researchers have employed the concept of compressive sensing in building micron-sized spectral filters that can be placed in front of a pixel on a detector. These spectral filters exploit nanophotonic technologies for their operation and many spectral transmission properties can be created to enable simultaneous multispectral compressive sensing. Although in principle these filters operate well, even though they require heavy al-

gorithmic implementation, they have certain limitations which can prevent wide adaptation across many verticals. One difficulty is the laborious process of fabricating the spectral filter array and installing it into the detectors since the detector fabrication process is completely removed from the filter fabrication process.

Currently, there exists no solution to capturing simultaneous multispectral images across multiple spectral channels, in the visible and the NIR wavelength range, that can maintain spectral fidelity of the images and at the same time does not involve the use of costly processes and equipment to enable the capability. The purpose of the work presented here is to use the concept of compressive sensing to perform simultaneous multispectral imaging across the visible and the NIR wavelength ranges on a single detector using a novel optical implementation that would enable the view of multiple angles of an object concurrently. Each of the views that are created are spectrally filtered and enter the imaging device simultaneously. The spectral channels maintain their true spectral intensity as they are not altered through various interpolation algorithms by the imaging device. The system is designed to be modular and versatile and can serve to satisfy the requirements of many applications.

1.1 Imaging

Imaging or digital imaging is the process of observation and digital recording of the intensity of the electromagnetic spectrum. The region of concern of the work presented here is limited to the visible and the NIR portion of the electromagnetic spectrum. These two regions will be referred to as 'light'. The observed or recorded intensity of light is dependent on the attenuation of light that interacts with an object and is reflected or scattered by it or alternatively the intensity in the emission of light from an object. Independent of the process that makes the light available for imaging, the recorded signal can be used to extract information about an object. The recorded signal is acquired using an imaging device which includes some form of image forming, light focusing, refractive (lenses) or reflective (mirrors) component with conjunction with a pixelated detector which can discretely digitize the incoming light to which it is sensitive.

The primary colors of light - red, green, and blue - exist in the visible region of the

spectrum and are responsible for the color vision of humans. Using these three spectral channels the color pigment of an object can be discerned. If the same object was observed in many more spectral channels other than the three primary channels other information about the object can be derived. These information may include chemical composition and state variables such as temperature, pressure, etc. By going beyond the visible region and performing spectral imaging into the NIR region, other information that are not necessarily available in the visible region can be acquired.

1.1.1 Multispectral Imaging

The concept of imaging depends on the sole criterion that the target of interest reflects, absorbs, or emits electromagnetic radiation based on its molecular composition and its micro- and macro-scale structure and state. In principle, different material (of differing molecular composition) remit radiation of various wavelengths differently. Based on the imaged electromagnetic radiation it is possible to determine the molecular composition of the target, therefore identifying it.

In normal photography, the visible wavelengths of the electromagnetic spectrum (400 - 700 nm) are registered as an image. This wavelength range is split into three smaller contiguous regions: red, green, and blue (RGB) and the amount of light measured from these regions by the camera is balanced and co-added to produce an image. Depending on the illuminating light source other electromagnetic wavelengths may be accessible. For example, the Sun, a 'white light' source, irradiates a target at sea level with a continuum of light of wavelength 350 - 9000 nm, with a few gaps. Figure 1.1 demonstrates the accessible regions of the electromagnetic spectrum of solar radiation at sea level. In the γ- and X-ray wavelength range, the atmosphere is completely opaque and in the radio wavelength range the atmosphere is virtually transparent but this is beyond the scope of the current work. Conversely, Mercury fluorescent lamps are strong line emitters in the visible region only. In the context of this work, multispectral imaging refers to observation of a target in the visible and NIR wavelengths, hence, a white light source is necessary for such observations.

In the 17^{th} century, Sir Isaac Newton showed that sunlight can be disassembled using a glass prism [25]. Newton was able to definitively disassemble the visible wavelength range into seven regions and this was the beginning of multispectral approach of studying

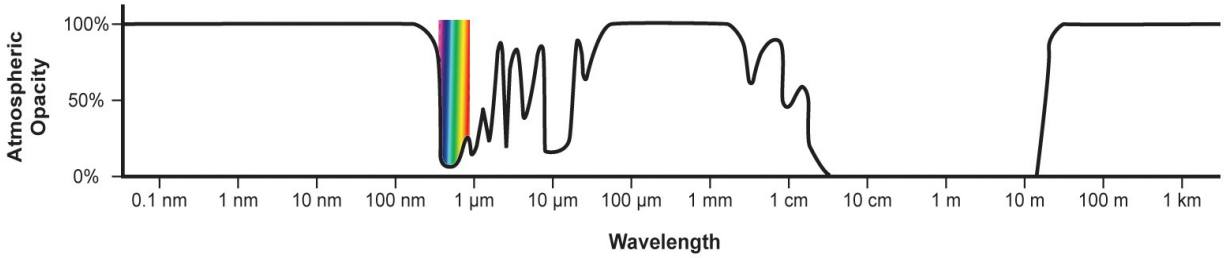

Figure 1.1: The opacity of Earth's atmosphere to solar irradiation, the visible wavelength regions is highlighted [110].

light. This simple experiment lead to many discoveries when it was established that the reflected, emitted, or remitted light from different material can be coded in the observed radiation. Optical filters were created to either suppress or transmit certain colors of light in this range and many objects, terrestrial or extra-terrestrial, were observed using this technique.

The NIR wavelength range was discovered in the mid 18^{th} century by Sir William Herschel. He stumbled upon this discovery while performing an experiment to measure the temperature of the seven colors discovered by Newton. He found an increase in temperature as he moved from blue to red wavelength. He measured the maximum temperature in the dark region (no visible light is observed) just beyond the color red [58].

Other regions in the electromagnetic spectrum (γ-rays, X-rays, microwaves, sub-millimeter, and radio) were discovered thereafter and their usefulness was proven in many fields of science, namely astronomy and astrophysics. These wavelengths are not examined for the purposes of this work and will not be discussed.

Aside from astronomy, which strives to access the entire electromagnetic spectrum available, most terrestrial applications use the visible, NIR, and short-wave infrared (SWIR). In general, the visible wavelength refers to light of wavelength 0.4-0.7 μm, NIR 0.7-1.0 μm, and SWIR 1.0-2.5 μm [39]. Some examples of terrestrial application that utilize the multispectral approach are Earth observation, defense and military, security, criminology, medicine, pharmacology, food engineering, and visual arts assessment and conservation.

Earth observation is an 'umbrella' term that includes the study of the Earth's physical, chemical, and biological systems from airborne or spaceborne platforms. These studies

include: land use, deforestation, agriculture, climate science, etc. As an example, for agricultural use, the health and potential yield of a crop can be estimated using the quotient of different NIR bands with comparison to some imagery in visible bands [109]. In defense, military, and security, images from different bands can be used to confirm the location of buildings, bunkers, vehicles, identification of banned substances, etc. In medicine and pharmacology multispectral imaging has been used for studying the human skin, measuring blood oxygenation levels, chemical contents of drugs, etc. [43, 46]. Fruit grade and quality can be determined by observing localized spectral discrepancies in the crop, as well as the level of fermentation of wine and beer can be determined using this approach [131]. Recently Fischer and Kakoulli [39] demonstrate the merits of using multispectral imaging systems to aid with preservation and conservation of visual arts.

The multispectral imaging approach has proven useful in many fields of science for research and development as well as everyday commercial and household applications. As the technology advances the imaging systems will follow suit and many more applications will be discovered.

1.1.2 Multispectral Imaging Devices and Techniques

The simplest form of multispectral imaging is the decomposition of an imaging device whose detector uses a Bayer color filter array in order to make observations in the three visible primary colors, red, green, and blue (RGB). This method is very simple and can be done using image processing software that is available free of charge [92]. The spectral bands are highly dependent on the spectral response or sensitivity of the detector and will vary between different detectors. This method is not a very accurate radiometric representation of field-of-view (FOV) because detectors using color filter arrays need to interpolate the missing spectral information in a given detector pixel using its neighboring pixels which do not contain similar spectral information therefore, contaminating the spectral data. By extension, the three-channel RGB images can be converted into various other color spaces, decomposed, and enhanced to extract features [82], however, at that point the integrity and fidelity of the data is compromised for any diagnostic considerations.

There exist two alternate, and perhaps more accurate methods for multispectral imaging. Multiple spectral images can be captured by using spectral bandpass filters in combi-

nation with a monochromatic detector and sequentially imaging the target. These filters are designed to accurately transmit a wavelength range of interest while suppressing all other wavelengths. The number of spectral filters is proportional to the number of spectral channels desired. As previously discussed most multispectral imaging device perform this task using a sequential process. These devices use a rotational filter wheel [40, 132] containing spectral filters, that is placed in front of the imaging optics of the device and is used to only allow a certain range of the wavelengths to enter the instrument. Alternatively, acousto-optical and liquid crystal tunable filters could be used instead of the filter wheels [11, 36, 51, 54, 68].

Another sequential method can be used which does not lend itself to all applications and requires controlled and predictable environment in which it needs to operate. This method would use various light sources at different spectral emissions to illuminate the target and acquire the image of the light that is reflected or scattered back from the target using a monochromatic imaging device [3, 45, 139]. The main disadvantages of all sequential multispectral imaging techniques and instruments are complicated in nature and time consuming for acquisition therefore non-preferential when imaging dynamic FOVs introducing motion blur which degrades the spatial resolution and the overall image quality or transient events.

Simultaneous multispectral imaging is possible using a combination of various beam-splitting and spectral filtering optics and numerous monochromatic detectors, the number of which would be proportional to the desired number of wavelength channels [86, 112]. In this setup the number of channels is limited because of the cumulative transmission loss, drop in efficiency, as the light passes through various optical elements. There is also a high probability that the images downstream will have aberrations again as a result of traversing through various optics. Alternatively, a series of cameras, each with their own filters, can be used to image the FOV at different viewpoints [37, 128, 133], which requires post processing to register and align the acquired images. The disadvantage of such devices is the complexity and cost of instruments themselves. Additionally, these instruments require careful alignment and occasional realignment and servicing for optimal operation.

A single-camera multispectral imaging device has been proposed which uses an optical augmentation to an image capturing device which allows simultaneous multispectral imaging [84]. Their instrument uses the working principles of a kaleidoscope to reproduce the

image of the FOV of the camera many times and uses a bandpass filter array to filter each reproduced image before image acquisition. This device acquires multiple spectral channels in the visible region for a single viewpoint which provides the benefit of not needing to register the spectral images post acquisition. This imaging device is operationally limited to the visible region of the electromagnetic spectrum, has low spatial resolution since the detector area is being shared among nine separate replicated images, optical aberrations are reintroduced into the images as a result of re-imaging using simple lenses, and the spectral fidelity of the images is not maintained because spectral mixing occurs as the result of their projection design. Other simultaneous multispectral imagers have been proposed and tested where modifications have been made to the imaging system and a color filter array has been introduced in the path of the beam accompanied by various beam steering and splitting components [111, 137].

Detector-based color filter arrays have been proposed for performing simultaneous multispectral imaging where each spectral filter covers and array of pixels sine there are limitations to the miniaturization of these filters [90, 91, 104], all operating in the visible wavelength range. The first multispectral color filter that allowed for imaging beyond the visible wavelengths replaced one of the green pixels in a traditional Bayer color filter array with an NIR filter [55].

The advancements in nano-photonics have given rise to spectral filtering capabilities via spectral filters that are microns in size. A collection of these filters have been fabricated into an array and placed directly on a monochromatic detector with the size of each array element matching the size of the pixels in the detector. In a sense, a new form of color filter array has been developed where the filtering need not be limited to the visible wavelength range and the number of channels becomes arbitrary and selectable. The filters in this case are composed of vertical nanowires constructed to transmit a specific wavelength of light and allow it to reach the detector [27, 99, 100].

It is important to note that the color filter arrays discussed here all require the implementation of advanced image reconstruction algorithms to approximate the intensity value in pixels that have no information in various channels. The larger the number of spectral channels the fewer number of pixels on a detector that are making measurements at a given channel and therefore the need for a very robust reconstruction algorithm.

1.2 Compressive Sensing

The concept of compressive sensing was first introduced as a way of reducing the copious amount of data generated and their storage in various signal-generating fields [34]. This concept hinges on the assumption that there exists a nominal number of incomplete or under-sampled measurement points which the complete, fully-sampled, signal can be generated with high accuracy and specificity. It is therefore a necessary requirement that compressive sensing hardware be accompanied by reconstruction algorithms which are capable of reproducing the complete signal that would resemble the actual signal as closely as possible [6, 22]. These reconstruction algorithms are designed specifically for each application as some prior knowledge about the data and the acquisition system is required for achieving good results in reconstruction. Having this prior knowledge will allow the sampling rate of the data to be pushed well under the Nyquist-Shannon sampling theory which states that a signal can be perfectly reconstructed given that the highest frequency in the data is less than half of the sampling rate [94]. There are many fields that reap the benefits of using compressive sensing without any adverse affects to the quality of the results such as photography [35, 108], holography [19, 106], medical imaging [80, 81, 77], and astronomy [16].

The proliferation of custom-built spectral filter arrays in conjunction with the advances in nanophotonics has enabled simultaneous MS imaging by facilitating for wavelength filtering on the imaging detector at the pixel level. Such compressive sensing-based approaches can greatly improve acquisition time by allowing for simultaneous capture of multiple wavelengths, greatly reduce the complexity of the optics in the instrument since filtering is achieved at the detector level, as well as facilitate for more compact and easy-to-use instrument producing more accurate spectral images. Naturally, as the number of spectral channels increases the more sparse the information in each channels is. The trend in performing multispectral imaging using multiple channel pixel-based color filter array is growing, therefore the need for advanced algorithms used for reconstruction of the compressive sensing simultaneous multispectral imaging is growing as well [79, 90, 99, 100, 135, 137].

1.3 Computational Imaging

Computational imaging is a growing field in which the complexity of the image acquisition instrument is removed from the optical implementation and placed on the algorithmic post-processing after the image acquisition. This form of imaging is used to improve the performance of cameras or extract features from images that were otherwise not accessible. Computational imaging covers a wide range of applications namely, panoramic imaging, high dynamic range imaging, light-field imaging, and three-dimensional imaging [65, 67, 93]. There exists various algorithmic solutions and implementations of computational imaging however only a few of these are employed in this work. The topics included in this section are meant to serve as supplementary information to the content presented in Chapter 4.

1.4 The Design Motivations

As mentioned previously, the multispectral imagers in use acquire images sequentially and those that perform simultaneous imaging are limited in the number of spectral bands being imaged. For sequential imagers there is time delay as the system is changing between bandpass filter and there is the possibility of the images being misaligned after acquisition which requires manual post-processing of the images and any transient phenomena can be missed. Almost all multispectral imaging solutions are devices that are not hand-held (table top or on a cart) and often require operational training.

The principal goal of this research is to simultaneously (single acquisition) acquire several spectral images of a field-of-view using a hand-held, point-and-shoot, instrument.

The high level design requirements of the imaging device are:

- Illuminate the target with light in the visible and the near infrared, or, to create a device capable of inducing emission in the mentioned range as demonstrated in § 3.2 and Chapter 5;
- Be capable of imaging in the 400-1100 nm range as demonstrated in § 3.5;

- Perform multispectral imaging in single acquisition (simultaneously) as demonstrated in § 3.5 and Chapter 5;
- Have a field-of-view of $\sim$ 30 mm in diameter as demonstrated in § 3.2;
- Be capable of imaging at a modest spatial resolution ($\sim$ 200 μm) to allow for visualization of fine structure in the imaging field-of-view as demonstrated in § 5.1.

1.5 Structure of the Thesis

This thesis is divided into seven chapters (including the introduction chapter). Chapter 2 provides a general overview of the systems design and explicitly outlines the specific contributions of this work. Chapter 3 outlines the design and characterization of the instrument that enables simultaneous multispectral imaging using multiview computational compressive sensing across the visible and the NIR wavelength regions. Chapter 4 presents the computational imaging technique that is required to accompany the hardware implementation of the instrument to complete the system. In Chapter 5 the imaging system is put to the test by examining its performance capabilities. Lastly, Chapter 6 provides a summary of the work presented, a list of limitations of the system, some immediate areas of research for expanding on the work presented, as well as the potential impact that such a system could have in several application fields.

Chapter 2

System Overview and Contributions

This chapter presents the system to be designed and studied, as well as the system's architecture including the various components of the instrument that collect light as an input and generate multispectral images as output. The aim of this work is to create a multispectral imaging device that is able to capture the image of an FOV across multiple spectrally unique wavelength ranges in the electromagnetic spectrum in a simultaneous manner via a novel, multi-view optical implementation of compressive sensing. As previously discussed, sequential multispectral imagers are costly and lack the time resolution that may be required for imaging. Simultaneous multispectral imagers are bulky, complex, costly to build and/or fabricate (in case of the multispectral color filter arrays), and not easily usable. The proposed multiview optical implementation of compressive sensing allows for the use of rudimentary optical components which are all stationary and easily adaptable for any off-the-shelf imaging device. The instrument has high time-resolution capability in contrast to sequential imagers. It does not suffer from efficiency losses as a result of the light interacting with many optical components in contrast to the beamsplitting imagers. In addition it is very easily assembled and does not suffer from high alignment tolerances in contrast to the pixel-based filtering imagers. Similar to the pixel-based filtering imagers, the instrument presented in this work will make use of compressive sensing techniques to perform the multispectral imaging.

Figure 2.1 shows the high level design of the system including the main components of the instrument. These components are presented in two main categories of hardware and

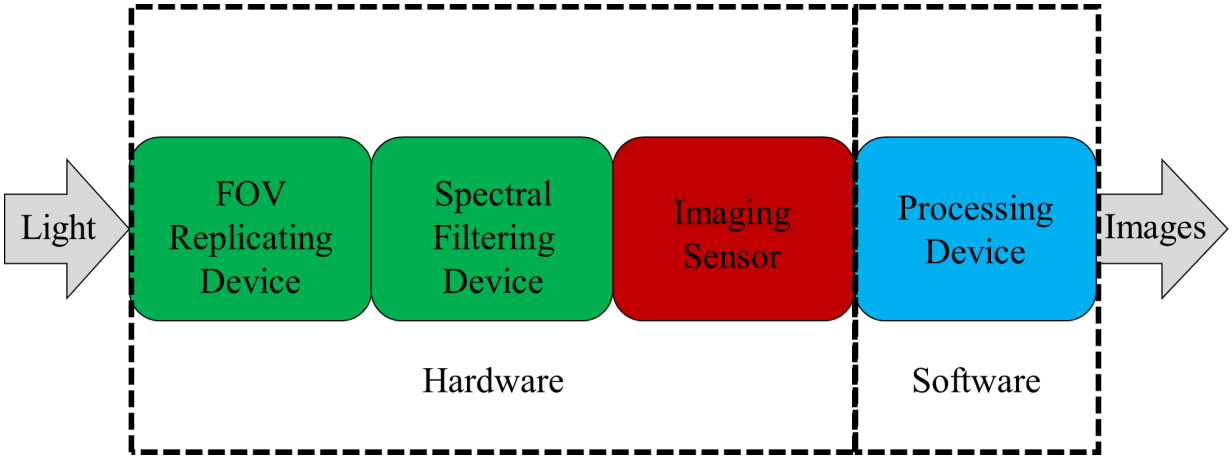

Figure 2.1: The system's architecture of the device presented in this work.

software. The hardware category consists of the components which accept the incoming light, replicate the FOV, perform spectral filtering, and record the multiple images of the FOV. The software category will then manipulate the images captured to create a multispectral image cube, enabling various applications of the device.

The system is designed to perform multispectral imaging simultaneously, across the visible and the NIR regions of the electromagnetic spectrum in six spectrally unique channels. The incoming light, reflected or scattered off of an object, enters the system and encounters the FOV replicating device which is a series of mirrors positioned obliquely to the optical axis of the imaging device. These mirrors are used to steer the light that would have otherwise missed the imaging device, into it. As such, each of the mirrors presents a unique point-of-view (POV) of the object to the imaging device. The light redirected by each of the mirrors as well as the light traveling along the optical axis of the instrument encounter a series of spectral filters in the spectral filtering device and are separated into four large regions of the electromagnetic spectrum spanning the visible and the near infrared wavelength regions. The light is then imaged by the imaging device which consists of image forming optics and a detector with a Bayer color filter array. The spectral properties of the pixel-based filters in this array facilitate the six-channel multispectral imaging in a compressive sensing manner. A more in-depth representation of the hardware implementation of the work is presented in Chapter 3.

After the capture of the multiple POVs, each in a specific spectral range, the computational imaging aspect of this work commences. First, the captured raw images are dissociated based on the spectral filter transmission properties into the six appropriate spectral channels. These six images will be spatially sparse depending on which of the filters in the color filter array is utilized to create that channel. Actual measured data will be present in one out of every four pixels in the red and the blue channels and one out of every two pixels in the green channels of the color filter array. This process results in a pseudo-random spectral imaging pattern of the FOV. The next step in the computation imaging process is to reconstruct the compressive sensing grid. This is done by remapping the pseudo-random sampling of the six spectral images, or rather their pixel locations captured by the camera to the compressive sensing grid. There exists a set transformation matrices that would remap the pixels in the imaging device to the compressive sensing grid. The remapping is carried out through the use of registration techniques to obtain the calibration and remapping parameters. The result of the remapping is a pixel space in which the majority of the pixels contain no information and a select few contain spectral information from six spectral bands. The purpose of multispectral imaging is to create an image hyper-cube in which all pixels are represented in all spectral channels. An interpolation technique is used to evaluate the intensity value at the pixel locations where no measurement is performed in each one of the six channels independently. Some defocusing and image degradation will occur as a result of the replication of the FOV and the process of compressive sensing, therefore a hyper-focusing process is implemented to correct these shortcomings in each spectral band. Finally, the fully-sampled multispectral hyper-cube can be used for multispectral analysis and the component analysis is done to extract information from the dataset. A more in-depth representation of the computational imaging implementation of the work is presented in Chapter 4.

A more specific breakdown of the contributions of this work are presented below:

1. A method for and optical design of a FOV replicating device, enabling the multiview imaging capability, § 3.2;

2. A method for and optical design of a simultaneous spectral filtering device from visible to the near infrared, § 3.5;

3. A design and implementation of a housing and an attachment mechanism for the FOV

replicating and the spectral filtering devices for adaptation to any image capturing device, § 3.6;

4. A method of performing spectral characterization of an image capturing device, § 3.4.2;

5. Additional characterization of the image capturing device (i.e., noise floor, dead pixels, quantum efficiency, white balancing, etc.), § 3.4;

6. A method of performing spectral compressive sensing via simultaneous multispectral imaging on a single imaging device, § 4.2;

7. A method and implementation of a hyper-focusing technique for addressing any defocusing aberration in any image capturing device, § 4.3;

8. Interpretation of extracted information from multispectral data using dimensional reduction analysis, § 5.

Chapter 3

Multiview Optical Spectral Imaging

As mentioned in Chapter 1, there exist snapshot multispectral imaging systems that use a collection of different dichroic beamsplitters in conjunction with as many lens-detector combinations as the desired number of wavelength. These systems are extremely costly to build, large in size and non-portable, and very complex to keep aligned and in a usable form. Almost all of the mainstream multispectral imagers, capable of imaging in higher than five spectral bands, acquire images sequentially. This means that there is wasted time as the system is changing between bandpass filters and there is the probability of the images being misaligned after acquisition which requires manual post-processing of the images. Additionally, multispectral imaging of a transient phenomena is not possible.

This work sets out to devise an imaging instrument to simultaneously (single acquisition) acquire several spectral images of a FOV using a point-and-shoot, non-contact instrument which is easy to use and requires minimal training using the concept of multiview computational compressive sensing. In principle, the optical design presented here can be installed on any camera system and used for the purpose of simultaneous multispectral imaging.

This chapter presents the design of the attachment to the camera that enable the system to function as a concurrent imaging device across multiple spectral bands in the visible and the NIR imaging. This design includes the manual white balancing of the camera after the removal of the NIR cut-off filter; further understanding and characterization of some of the properties of the detector such as the quantum efficiency, the noise floor, the non-

usable pixels and the spectral characteristics of Bayer RGB filters [10] integrated into the detector; location and orientation of the FOV replicating optics; inclusion of spectral filters in the beam path to enable multispectral imaging across visible and NIR wavelength range; possible design of light sources accompanying the imaging instrument enabling imaging in reflectance or fluorescence mode; and finally the structural design of the attachment to be integrated onto an imaging device.

3.1 Light-Matter Interaction

In general, light rays generated by a source will propagate in the medium and encounter boundaries when arriving at new media. When light interacts with a medium it can be reflected from the surface of a material, which is referred to as specular reflection. It can travel directly through a material without interacting with it, which is referred to as direct transmission. Other than the two outcomes mentioned above, light will interact with the material and be scattered inside the material. The light is then destined to either be absorbed by the material or emerge via diffuse reflection or transmission [15, 74].

Light is said to be interacting when it encounters a change in the index of refraction

$$n(\lambda) = \sqrt{\epsilon_r(\lambda)\ \mu_r(\lambda)} \tag{3.1}$$

where $\epsilon_r(\lambda)$ is the electric permittivity and $\mu_r(\lambda)$ is the electric permeability of the material relative to that of the vacuum both being a function of wavelength λ. These values differ for different materials and are well understood for almost all materials. At these interfaces, light is destined to one or all of the above-mentioned situations. For reference, the index of refraction of air is ~ 1.0.

For the purposes of the work presented here only one form of absorption and scattering will be considered. More specifically, in case of fluorescence, § 5.1 and § 5.2, absorption will be an elastic process with a Stoke's shift emission, and scattering will be mostly dominated by Mie scattering, § 5.3. In both cases presented below absorption is governed by the Beer-Lambert's law which is represented as [89, 124]

$$I_a = I_i e^{-\kappa(\lambda)cz}, \tag{3.2}$$

where I_a is the measured intensity of light after absorption takes place, I_i is the incident intensity of light, $\kappa(\lambda)$ is the molar excitation coefficient which is a function of wavelength of light, c is the concentration, and z is the distance traversed within that material. Note that in single instance scattering or reflectance measurement the distance traveled would be twice that of the distance traveled in transmission measurements. In diffuse reflectance measurement which is result of a number of continuous scattering events within an object, the piecewise summation of the Beer-Lambert law can be considered the net effect of which is the decrease in the intensity of the remitted light.

3.1.1 Mie Scattering

Mie scattering theorized by Gustav Mie in 1908 explains the interaction of light of wavelength similar to the size of particle or molecule it is interacting with [87]. The complex theory is evaluated numerically under the assumption that the particle in question is spherical and the light is monochromatic (single wavelength). If interaction with multiple particles is desired, each particle has to be considered separately and the total effect would be the summation of the individual interactions [74, 119].

Scattering is capable of changing the light polarization after the scattering event, therefore the process of scattering can be described by a Mueller matrix that transforms the Stokes vectors of the incident light beam to that of the scattering light beams as a function of the scattering angle. The scattering angle is defined as the angle by which the scattered beam is subtended with respect to the direction of travel of the incident beam. Mie scattering can therefore be represented in terms of a series expansion as [74]

$$\widehat{I}_s = \frac{16\pi^2 a^6}{\lambda^4 r^2} \left\| \frac{\mathfrak{m}^2 - 1}{\mathfrak{m}^3 + 2} \right\|^2 \begin{bmatrix} \frac{1}{2}(1 + cos^2\theta) & \frac{1}{2}(cos^2\theta - 1) & 0 & 0 \\ \frac{1}{2}(cos^2\theta - 1) & \frac{1}{2}(1 + cos^2\theta) & 0 & 0 \\ 0 & 0 & cos\theta & 0 \\ 0 & 0 & 0 & cos\theta \end{bmatrix} \widehat{I}_i, \tag{3.3}$$

where $\widehat{I}_i$ is the Stoke's vector of the incident light beam, $\widehat{I}_s$ is the Stoke's vector of the scattered light beam, λ is the wavelength of light, a is the radius of the scattering particle, $\mathfrak{m}$ is the ratio of the $\widehat{n}_2$ which is the complex index of refraction of the particle to $\widehat{n}_1$ which is the complex index of refraction of the medium, r is the distance from the center of the

particle to the observation point of the scattered beam. The first element of the Stoke's vector is the intensity of the beam, therefore in this case $\widehat{I}_s^0$ is the intensity of the light beam after Mie scattering.

3.1.2 Fluorescence

Many biological and natural materials give off light of a particular color when exposed to light of another color. If the emitted light occurs rapidly after excitation, the process is referred to as fluorescence. Fluorescent materials are extremely useful as labels or indicators in many biological applications. The photophysics of fluorescence is relatively simple. The incoming light, at appropriate wavelength, is absorbed by one of the electrons in an electron pair in the ground state of the molecule and is excited to a higher state. This electron consequently loses energy via emission and de-excites and returns to the ground state shortly there after (on time scales of $\sim$ 10 ns) [89].

Fluorescence emission is isotropic, meaning it has no preferred beaming directionality and is in general much weaker than the intensity of the excitation light. Furthermore, fluorescence emission is influenced by some state variables such as temperature, pressure, and other surrounding molecules that may act to enhance or attenuate the fluorescent emission of the molecule of interest.

Fluorescent material may emit light at longer wavelengths than the excitation wavelength this phenomenon is called Stoke's shift emission and is based on Stoke's law [114]. Large Stoke's shifts are desired in fluorescent imaging to differentiate between the excitation and the emission spectra clearly without the use of costly and complicated optical setups. At times the emission wavelength can be shorter than the excitation wavelength which is referred to as anti-Stoke's shift and is prevalent in Raman emission however, anti-Stoke's fluorescent emission has been shown using incoherent excitation sources [78].

3.2 Light Source Design

For applications of the system that are to be carried out without the presence of the appropriate illumination source, on-board illumination has to be designed and utilized. To

manage the scope of the work only two modes of imaging, reflectance and fluorescence, are considered.

Generally, since the quantum efficiency (QE) of the NIR region of the detector is so much lower than the visible range, capturing a well-exposed image in the visible range would result in under-exposure in the NIR range. Conversely, capturing a well-exposed image in the NIR range would over-expose the image in the visible range. This problem can be addressed by introducing an appropriate neutral density filter, with appropriate optical density, to the POVs of the system, observing in the visible range (in this case POVs I and II, demonstrated later), to equalize the visible sensitivity to the NIR, as closely as possible.

3.2.1 Reflectance Mode

The appropriate design of a light source that would enable imaging in reflectance mode is extremely important especially if neutral density filters are not used for POVs I and II. If the neutral density filters are used, appropriate illumination will negate the need for long integration times. To avoid over- or under-exposure of any images captured using the system, appropriate and equalized illumination should be present for the spectral channels observable by the system.

There exists numerous suppliers with various collections of light emitting diodes (LEDs) with emission covering the entire visible-NIR spectral range. Based on the QE of the system, the optical power of the NIR LEDs has to be many times larger than the optical power of the LEDs in the visible range in order to equalize apparent power across spectral sensitivity range of the detector.

This experimental light source was numerically simulated and its emission spectrum as well as the resulting equalized spectral efficiency are shown in Figure 3.1. Since spectral channel three (CH3) has the highest efficiency among the six channels then the remaining five channels would be boosted with respect to it. In the visible range, channels 1 and 2 had to be boosted by a factor of 2.38 and 2.19 times, respectively, and in the NIR range channels 4, 5, and 6 had to be boosted by a factor or 7.81, 20.37, and 134.2, respectively. This means that if a costume light source were to be employed with the imaging system, the optical emission power of channels 1, 2, 4, 5, and 6 have to be larger than the emission power of

channel 3 by the numbers quoted. Using this setup, at a given integration (exposure) time all channels will be equally exposed and therefore the signal-to-noise ratio across all six channels will be optimized which will lead to images of better optical quality.

For the purpose of this research work, the design and implementation of the custom light source was deemed to be out of scope. A fiber-coupled Halogen Tungsten light source was used to illuminate the FOV of the instrument with sufficient optical power in the visible and the NIR spectral regions. The spectral shape as well as the spatial profile of the light from this light source is not uniform with larger optical power in the NIR compared to the visible range.

3.2.2 Fluorescence Mode

The phenomenon of fluorescence is described in § 3.1.2. Dependent on the chemical composition of the chromophores or the fluorophores, the appropriate and corresponding excitation wavelength of light should be used to illuminate the sample. Short wavelength, high energy, light sources emitting in the ultraviolet (UV) and violet wavelengths range, 360 - 410 nm, perform quite well in exciting the electrons in a molecule and will induce fluorescence. However, if the actual excitation wavelength of a material is spectrally different from the nominal excitation wavelength, the emission signal will be considerably weaker than if the material was illuminated at the appropriate excitation wavelength. Lasers, with high temporal coherence (resulting from a very small spectral bandwidth) are also a great fluorescence inducing excitation source.

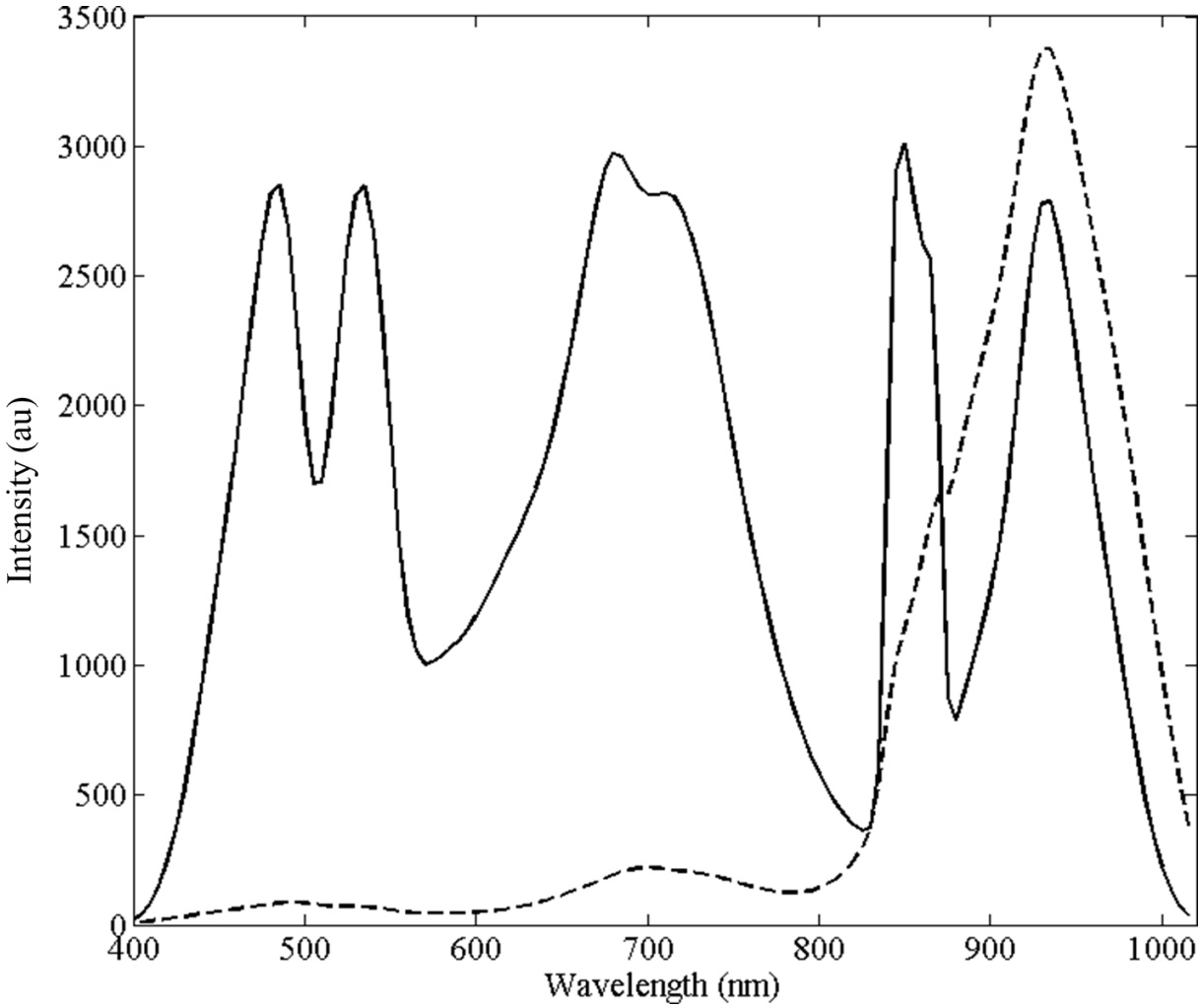

Figure 3.1: The emission spectrum of the hypothetical, costume, light source (dashed line) that is required in order to equalize the sensitivity of the system, across the entire spectrum (solid line).

3.3 Field-of-View Replicating Optical Design

One unique design aspect of the proposed system is its ability to image the same FOV in six spectral channels spanning 400 - 1000 nm simultaneously on the same detector. Figure 3.7 shows the division of the detector where the numerals in the figure denote the POV number as imaged on the detector. The light from each one of the POVs is filtered independently on its way to the detector. This means that each POV will have to observe the same FOV.

A field-of-view replicating mechanism can be designed that will redirect the light coming off of the target and would otherwise not enter the imaging system, back into the imaging system. Generally, if an object is isotropically illuminated it will scatter light in the hemisphere above it nearly isotropically, meaning the scattered light does not have a preferred direction therefore no beaming occurs. More formally the object can be viewed in the 2π steradian in the direction of the light source providing the illumination. The lens in an imaging system is only capable of sampling a very small portion of the scattered light and the portion of the solid angle is not observed by the lens and therefore not imaged.

The replicating optical design directs the beams scattered by the object, that would have otherwise not been observed by the camera, into the camera and therefore an image of the object is observed by the camera through the reflection. Figure 3.2 shows the principle based on which the replicator operates. The replicating elements are planar mirrors that are placed obliquely to the optical axis of the imaging system. The law of optical reflection is described by Fermat's principle [8, 18, 63] to be

$$n_1 sin(\theta_i) = n_2 sin(\theta_r), \tag{3.4}$$

where n_1 and n_2 are the refractive indexes of the medium from which the light is in pre-reflection and post-reflection, respectively, in this case $n_1 = n_2 = n$ which is the refractive index of air and is equal to ~ 1. The θ_i and θ_r are the angle that the incoming light and the reflected light form with the normal vector to the surface of the reflector. In the current design of the instrument there are four replicating mirrors, South, East, North, West and are denoted views II, III, IV, and V with view I being the real image of the object along the principal axis of the system.

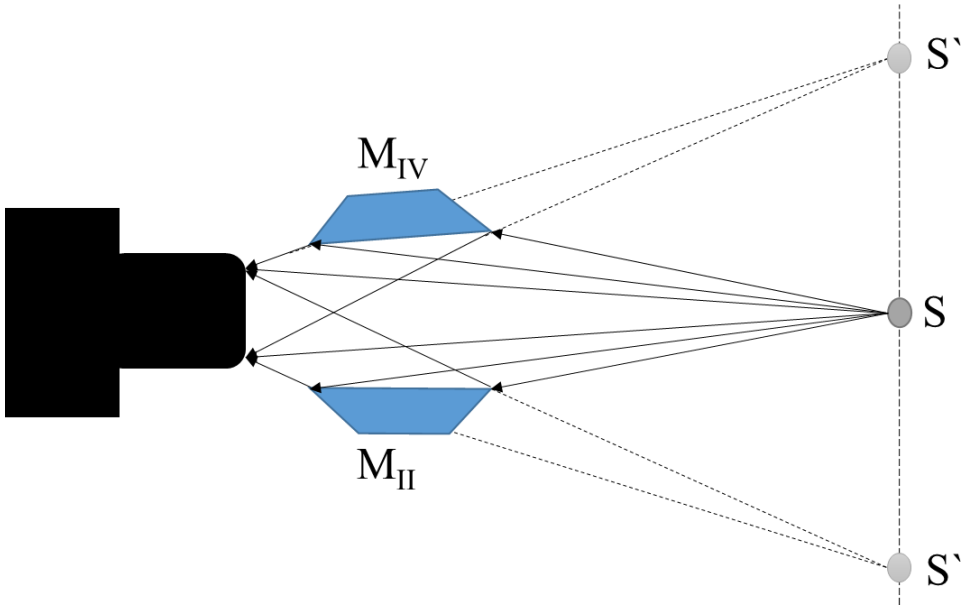

Figure 3.2: The side-view of the setup is shown here with only two (North and South) of the four FOV replicating mirrors (M) shown, with Each and West being out of the page and in the page, respectively. S denotes the object being imaged and S‘ represent the imaginary object resulting from the reflection through the mirrors.

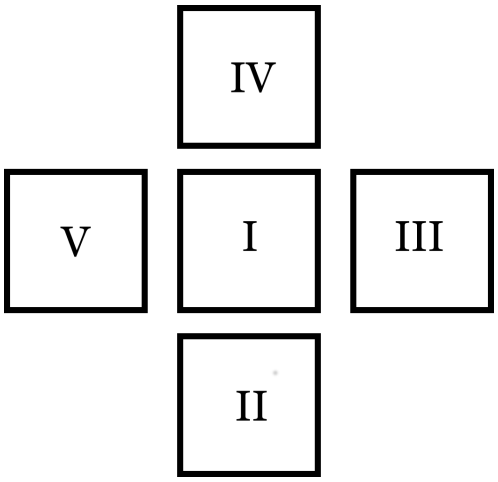

Figure 3.3: The five POVs as seen by the system.

Each of the views, as observed by the instrument, shown in Figure 3.3 present a different POV of the object. This means that to enable multispectral imaging producing an image cube, two spatial dimensions and one spectral dimension, accurate registration of the POVs II, III, IV, and V to POV I is required. This is explored further in § 4.1. Additionally, having access to different POVs of the same object can enable three-dimensional reconstruction of the features in the object being imaged. This capability has been showcased in Kazemzadeh *et al.* [65], however further extensions of this topic is beyond the scope of this work.

Proper placement of the replicating mirrors is required for the system to function as designed. The distance between the mirrors and the imaging lens is prescribed as part of the design of the camera attachment considering the space requirement for the spectral filters and the locking mechanism onto the camera lens. This will be discussed in detail in § 3.6. While the distance between the camera lens and the mirrors has been determined, two important factors about the location and attitude of the mirrors remain to be determined. These factors are: 1. the lateral distance between the face of the mirror and the principal optical axis of the system; and 2. the pitch, or rather the angle by which the face of the mirror will be subtended to the principal optical axis of the system.

A grid search approach, implemented using the testing hardware, was employed to find the optimal values for the radial distance between the mirror and the optical axis as well as the appropriate angle for the pitch of the mirror. The optimization criteria was to maximize the area of a circular spot as observed via the replicating elements (POV II, III, IV, and V) compared to the area of the same object as observed in the main view of the system (POV I).

The experiment was carried out once for the horizontal replicators, POVs III and V, and one for the vertical replicators, POVs II and IV. The spots tested were circular in shape and ranged in the size 43, 48, and 55 mm in diameter for the horizontal tests and 33, 38, 43 mm for the vertical tests. The range in the size of the spots tested in the horizontal and vertical directions are different since in the horizontal direction the replicated FOV is in fact larger because of the imaging aspect ratio imposed on the imaging device. The spots which were designed to have a uniform green color were located $\sim$ 180 mm away from the camera lens, centered on the principal optical axis. The mirrors were mounted on a rotational stage which was then mounted on a linear stage. The linear stage was used to

translate the mirror radially away from the optical axis and the rotational stage was used to subtend the mirror face to the optical axis.

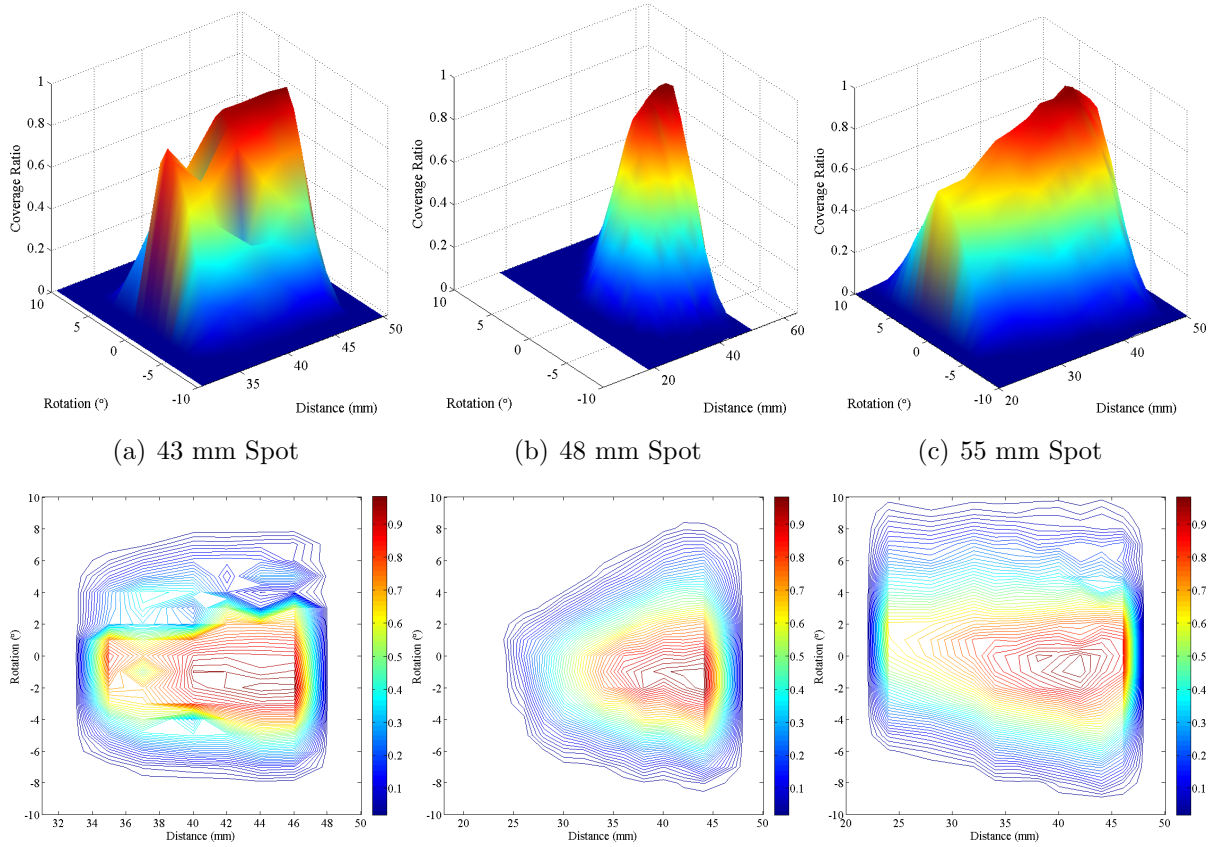

(a) 43 mm Spot (b) 48 mm Spot (c) 55 mm Spot

(d) 43 mm Spot (e) 48 mm Spot (f) 55 mm Spot

Figure 3.4: The coverage ratio of the replicating optics in the horizontal direction resulting from a grid search by varying the radial distance and pitch angle of the mirror with respect to the optical axis of the instrument. The three-dimensional space (a, b, and c) as well as the two-dimensional coordinate (d, e, and f) of the maximum coverage are represented.

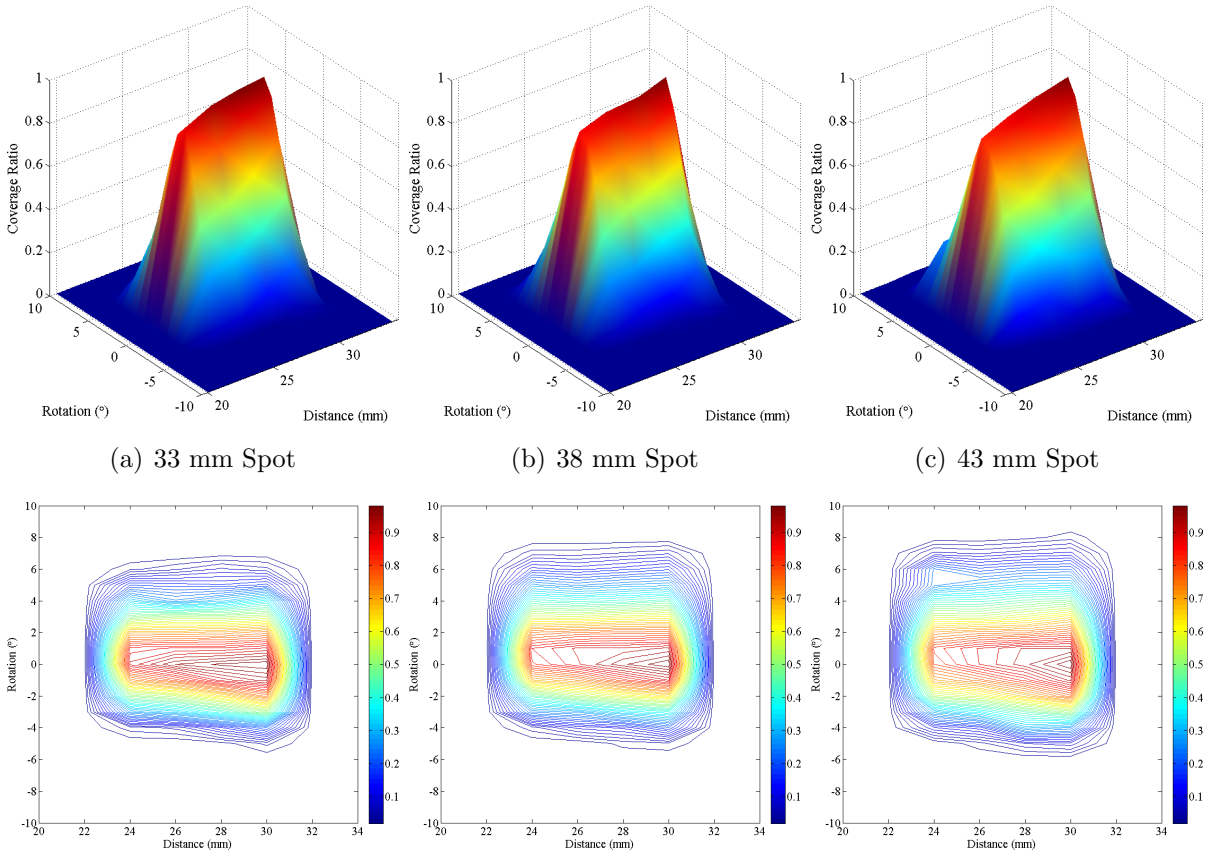

(a) 33 mm Spot (b) 38 mm Spot (c) 43 mm Spot

(d) 33 mm Spot (e) 38 mm Spot (f) 43 mm Spot

Figure 3.5: The coverage ratio of the replicating optics in the vertical direction resulting from a grid search by varying the radial distance and pitch angle of the mirror with respect to the optical axis of the instrument. The three-dimensional space (a, b, and c) as well as the two-dimensional coordinate (d, e, and f) of the maximum coverage are represented.

At each radial distance and angle an image was captured using the camera. The ratio of the observed spot through the mirror and the actual image of the spot was calculated by first converting the color space of the image from a Euclidean three-color, RGB, space to a cylindrical-coordinate representation of the the same color model, HSV color space [47] . Hue, saturation, and value color space is a color space in which the color (hue) is represented as a degree value from 0 - 360°, the color tone (saturation) is represented in the radial direction, and the intensity (value) is presented as the height of the cylinder. This is preferred space for evaluation of the coverage ratio of the replicated images since the green spots can be completely and easily identified as foreground in the captured images and by simply counting the number of pixels in the actual image and the replicated image of the spot and maximizing the ratio between the two the appropriate radial distance and the pitch angle of the replicating mirrors can be determined.

Figures 3.5 and 3.4 show the result of the grid search approach across a plane defined by radial distance between the mirror and the optical axis and the pitch angle as well as the resulting coverage ratio of a spot of a particular size. The pitch angle was varied through 21° from -10° to +10° and the radial distance was increased from 30 mm to 50 mm for the horizontal POVs and 20 mm to 35 mm for the vertical POVs. The discrepancy between the radial distance in the horizontal and vertical direction is in accordance to the aspect ratio of the camera itself.

Based on the experimental results the best radial location and pitch angle was determined to be 43 mm at -1.7° and 30 mm at -0.3° in the horizontal and vertical directions, respectively. The negative angle means that the mirrors are pitched inward, facing the camera. When the mirrors are situated in these ideal location the largest sample size that can reliably be observed in all five POVs is 30 mm in diameter. Figure 3.6 shows the captured image of a checkerboard pattern by the FOV replicating optics as observed by the detector. Note that the pattern imaged has a length of 25 mm on a side with a diagonal length of 35 mm, which is beyond the designed specifications mentioned above.

The mirrors used in the replicating component are front surface reflecting silver mirrors from Thorlabs [117]. These mirrors are capable of achieving reflection efficiency in excess of 98% when used in high angle of incidence mode across the spectral regions observable by the system. The angles of incidence of light onto the mirrors in the system are approximately 23.8° and 18.2° in the horizontal and vertical directions, respectively, therefore no efficiency

losses are expected as a result of the replication of the FOV. Oblique reflections do however scramble polarization information encoded in the incoming beam [20], the treatment of this phenomenon is beyond the scope of the work presented here.

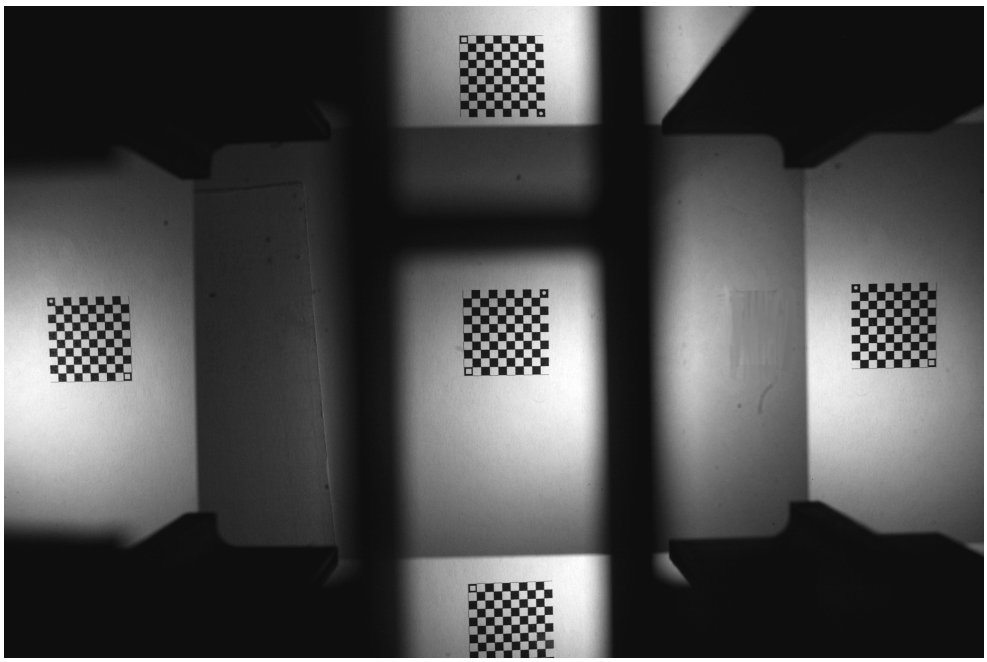

Figure 3.6: A checkerboard pattern was imaged using the instrument after the proper design and placement of the FOV replicating optics. Note, there are no spectral filters present in this image and all POVs are observing the same spectral region.

3.4 The Imaging Device

The popularity, ease of use, high pixel resolution, and superb imaging quality of digital single-lens reflex (DSLR) cameras has led to the acceptance and employment of these cameras in many fields of science and technology. To this end, a DSLR camera was chosen to be the imaging device platform for the work presented. Enabling the simultaneous multispectral image acquisition using the imaging device requires the addition of two hardware components to the imaging device: the FOV replicating device and the spectral filtering

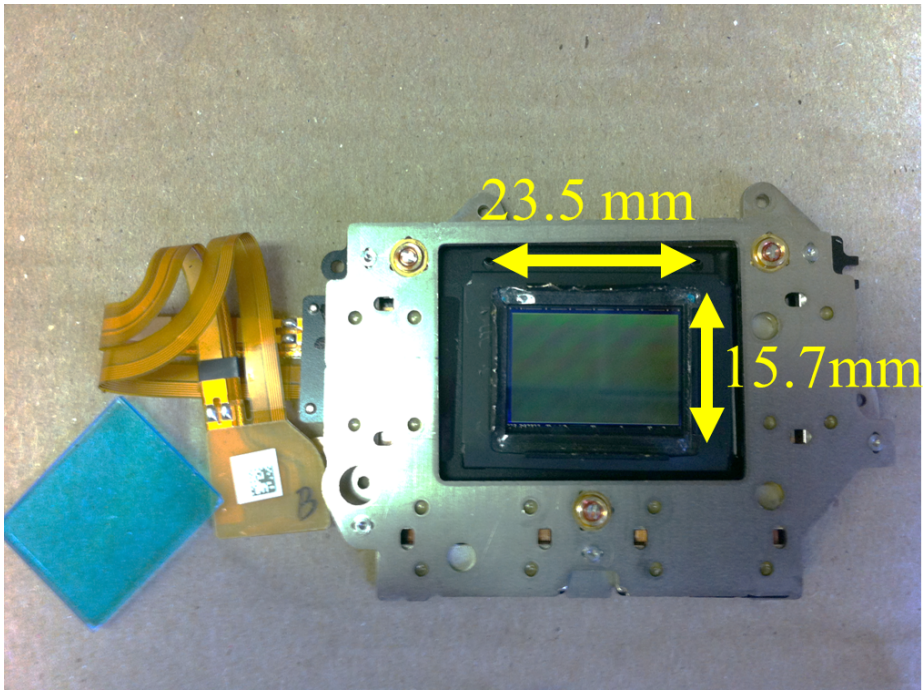

Figure 3.7: The CCD detector assembly of Pentax K100 D Super DSLR camera. The blue piece of glass is the IR-cut filter which was removed from the detector assembly.

device. The two aforementioned devices will work as a unit installed in front of the imaging device and will act to replicate the light containing information about the FOV into a number of POVs and spectrally filtering each view before the light beams enter the imaging device to be captured and recorded.

Today, the technology and optics used in high-end DSLR camera is far beyond what is available for lab use as far as complex lens design, size and resolution of the detector, integrability, and portability. To this end a Pentax K100 D Super DSLR camera with a six megapixel charged coupled device (CCD) detector was chosen as a system baseline for the proposed work. The CCD in this camera is capable of detecting photons at wavelengths approaching 1050 nm. Camera manufacturers install an NIR cut-off filter into their camera designs which acts to suppress light of wavelengths larger than ~ 650 nm, hence improving the RGB color levels and the sharpness of the image. For the purpose of creating an imaging device that can register NIR light, the NIR cut-off filter has to be removed from

the camera. Figure 3.7 shows a picture of the camera CCD assembly without the NIR cut-off filter (the blue piece of glass in the figure). The camera was subsequently reassembled and restored back to working condition.

Imaging in the NIR bandwidth requires the presence of NIR light. As was discussed in Chapter 1, the Sun illuminates the Earth, at the surface, with visible and IR light which enables NIR imaging of natural scenery with the modified camera for applications such as agriculture and forestry, etc. However, if the proposed system is to be used in an indoor environment with residential or commercial lighting (LED, fluorescent, incandescent), no NIR light will be present to illuminate the sample if it does not emit at these wavelengths. In the reflectance imaging mode, a broad band continuum light source, such as a Tungsten-Halogen light source supplied by Avantes (AvaLight-Hal) [5], can be used for illumination of the target FOV to provide both visible and infrared illuminating light. In fluorescence mode, the appropriate LEDs or lasers with peak emission matching the excitation wavelength of the chromophores or the fluorophores can be used to illuminate the FOV [72], alternatively, an ultraviolet source can be used which tends to activate the chromophores and fluorophores as well.

All the studies carried out in this work, the systems design, the computational imaging, and the applications, use the raw sensor readout from the camera. As previously discussed, consumer digital cameras use a color filter array, a Bayer pattern, to produce a color image. As a result, no one pixel is making observation in all three bands, therefore, various interpolation algorithms are used to estimate the missing two colors of a given pixel. These algorithms use the value of the neighboring pixels that are not necessarily the same color for this estimation. This cross spectral smearing will degrade the spectral fidelity of the image and render it useless for any radiometric measurement and analysis. Additionally, the detectors in the camera have very large bit depths, up to 16 bits, while the processed images out of the camera has a depth of only 8 bits. This introduces quantization errors in the measurements which then again degrades its radiometric value. By accessing the raw sensor readout, the high bit depth capability is preserved and even though the spectral images are not complete, due to use of a color filter array, advanced interpolation algorithms can be used to estimate the missing values in specific channels while preserving the spectral fidelity of the images.

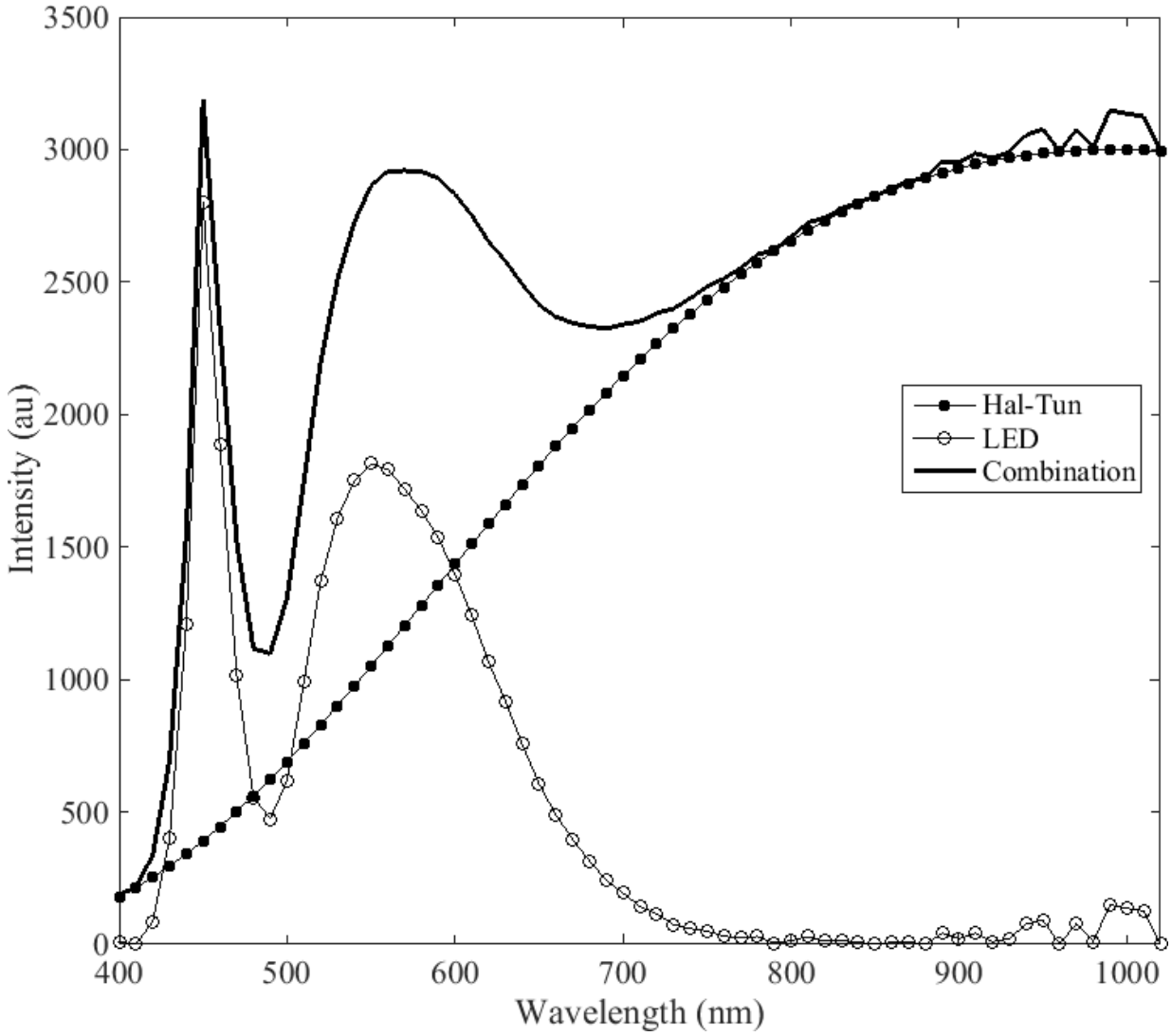

Figure 3.8: The light source combination utilized to white balance the modified Pentax DSLR. The connected-filled-circle curve represents the spectrum of the Halogen-Tungsten source, the connected-empty-circles shows the spectrum of the white LED source, and the solid line denotes the additive response of the two light sources.

3.4.1 White Balance Calibration

White balancing is used to artificially and computationally alter the spectral response of a camera to compensate for changes in scene illumination, depending on the light source [56]. These alterations are achieved by simply multiplying the RGB channels by a constant. Consumer cameras are manufactured with a series of default set of white balance presets all assuming that camera's optics will not be modified. In the case of the system proposed here, the NIR cutoff filter is removed hence the detector now has access to far more wavelengths of light than it did previously. As a result the preset white balance settings will perform sub-optimally and since the red channel has a stronger response in the NIR range all images captured by the camera, if demosaiced by the camera, will have a red hue.

In order to remedy this and capture images that are still aesthetically appealing, a custom white balance is defined for the camera to use. A white balancing target (Edmund Optics) [96], that has 99% reflectance across ultraviolet-visible-near infrared is used for this purpose. To ensure that there is optimal access to all wavelengths in the visible and the NIR by the camera, two light sources were used to illuminate the target, see Figure 3.8 for the spectral output of the two sources. In the same figure the spectrum of the addition of the two light sources are shown and that is the light that the camera is forced to detect and utilize to define the white balancing weights. Note that comparable power is observed across the spectrum where the detector seems to be sensitive, specifically, in the blue range below 500 nm, in the green and red range and likewise in the NIR range.

3.4.2 Detector Characterization

The camera detectors themselves are poorly characterized by their suppliers, however they are designed to perform their required tasks sufficiently well. If off-the-shelf consumer cameras are to be used, then their detector chips will have to be characterized to better understand their behavior in response to impinging light. Some of the most important factors in detector characterization are quantum efficiency, read-noise, dark current, and spectral responsiveness.

The imaging detectors that are manufactured mainly for scientific, commercial, consumer use are generally manufactured using silicon-based photosensors. These photosen-

sors tend to be sensitive to the wavelengths in the $\sim$ 300 - 1100 nm range, however, the level of sensitivity is not equal across the spectrum. The sensitivity is dependent upon on the efficiency of the Silicon photosensor to convert photons, at a particular wavelength, to a digital count through the analog-to-digital converter. This conversion efficiency is often referred to as the 'quantum efficiency' (QE) of the detector which is not constant across the aforementioned wavelength range. Figure 3.9 shows an approximation of the QE of the Pentax K100 D Super DSLR detector with peak efficiency at $\sim$ 570 nm. The figure is presented in normalized intensity for the purposes or demonstrating the relative differences in sensitivity at various wavelengths. Determining the absolute efficiency is beyond the scope of this work. The QE presented is an approximation of the true QE which is computed by the summation of the spectral response of the three color filters on the camera's CCD as discussed in §3.4.2. Note that QE efficiency of a detector encompasses certain error parameter associated with the detector such as the read noise and dark noise, however, for the purposes of this work these two parameters are not determined since absolute radiometry of observations is not a concern and beyond the scope. Additionally, the equipment used for characterization limited the spectral bandwidth to 400 - 1000 nm, omitting the UV region of the spectrum, however extrapolating the QE curve in Figure 3.9 using a monotonically decreasing function, the complete QE curve can be approximated.

For most scientific and commercial uses, a monochromatic detector is used which means that the sensitivity of the detector pixels are not limited to a specific region of the spectrum inherently. However, color detectors exist which include pixel-based filters that attempt to sample a specific region of the spectrum at the given specific pixel. These filters are generally designed and optimized for operation in the visible region of the spectrum ($\sim$ 400 - 700 nm) more specifically sampling three different windows - RGB - adhering to the human vision capabilities [4].

Even though the color filters are specifically designed to achieve high performance, which is measured by throughput efficiency, in the visible range of the electromagnetic spectrum, they will also have some performance in the NIR region as well. This response is however suppressed by the use of a NIR blocking filter placed in front of the detector to reject these wavelengths from illuminating the detector pixels.

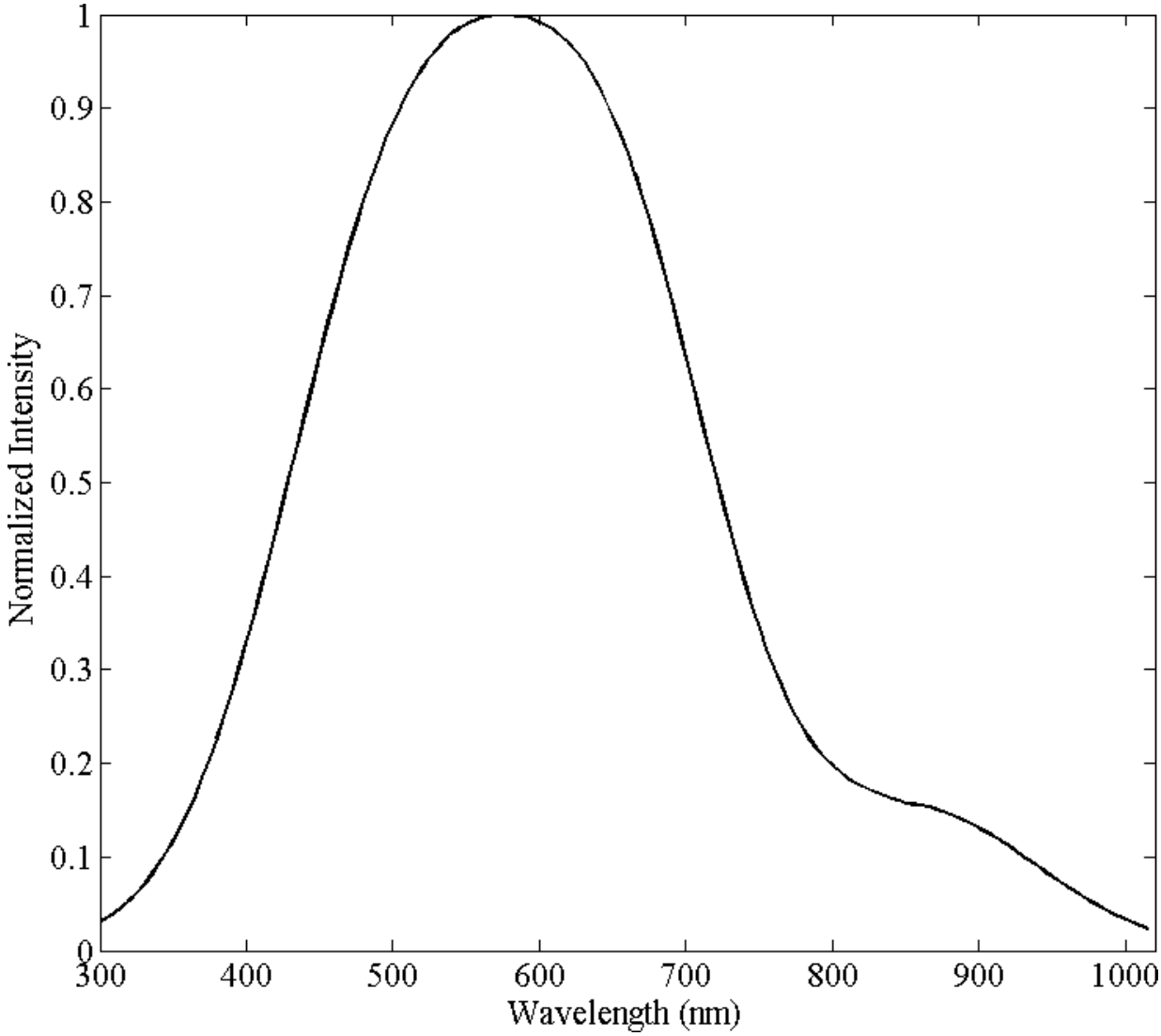

Figure 3.9: The approximate quantum efficiency of the imaging device.

Quantum Efficiency

The quantum efficiency is the ratio of the number of photons observed by a single pixel to the number of electrons that are released from the photodetector junction, assuming the photon energy is higher than the semiconductor bandgap energy. This ratio is strongly dependent on the wavelength of the photons incident on the detector as well as the material of which the detector is made (e.g., Si for the visible and NIR, InGaAs for the mid-wave infrared, ZnO for the ultraviolet, etc.). For the purposes of this study, in-depth investigation of quantum efficiency is deemed to be beyond the scope.

Sources of Noise

There exists many types of noise that will get introduced into any observations made using a detector and the level of detail used in describing them is application dependent. Shot noise is deemed to be the most predominant source and can be attributed to discrete nature of photons. The dark noise, also known as the thermal noise or dark current, is the systematic noise floor that exists in any electronic device due to thermal generation and diffusion of electrons which tends to increase with temperature of the device. It can be reduced using various cooling methods. The read noise and amplifier noise are additive noises which tend to behave like 'white noise' and add to the noise floor of the detector. When the analog signal is digitized by the analog-to-digital converter, quantization noise is also added to the digital signal [56].

The ratio between the peak signal level and the variance in the noise level contributions of all the possible sources determined the signal-to-noise-ratio (SNR) of an imaging device. In any optical photon counting application the statistics of the photons collected are of great interest. A detector is exposed to incoming radiation, light, for a specific duration of time. For every incoming photon there exists a probability inducing a release of an electron in the detector pixel circuitry which is known as the quantum efficiency of the detector. The release of the electrons in the detector are measured as a voltage change which is an accumulative process of the exposure time of the detector. Following photon collection, this voltage value can be divided by the duration of the exposure time which will result in the average optical power of the light observed by the detector's active area.

The signal in a photon sensing device is the number of photons received from the source. There exists no correlation between the photons emitted from a source, therefore the photon counting process can be modeled as a Poisson process. A Poisson process gives the probability of a number of independent, uncorrelated, events taking place in a given amount of time [52]. The Poisson probability distribution of photon arrival is,

$$Prob(N) = \frac{P^N exp(-P)}{N!}, \tag{3.5}$$

where N is the number of photons counted and P is the mean number of detected photons or the Poisson rate [7]. The mean optical power can be computed as $\frac{P}{t_e}$, where t_e is the exposure time.

In photon sensing systems the above-mentioned noise sources can be quantified as: Shot noise $\sigma_N = \sqrt{N}$; read noise $\sigma_{RN} = \sqrt{RN^2}$; dark noise $\sigma_{DN} = \sqrt{DN}$, the sum of which is the noise in the system providing the SNR of

$$SNR = \frac{N}{\sqrt{N + RN^2 + DN}}. \tag{3.6}$$

For applications that are not photon-starved, meaning there is ample light to perform the sensing in the SNR takes a limited form of

$$SNR = \frac{N}{\sqrt{N}} = \sqrt{N}, \tag{3.7}$$

as contribution of the read noise and dark noise become insignificant compared to the contribution from the shot noise.

All noise sources mentioned above will appear as variations on the signal measured by the detector. However with the exception of the shot noise and the amplification noise, which have temporal variations, all other noise sources can be assumed to be consistent from pixel to pixel across the detector and will have a constant biasing effect on the signal amplitude, which can be measured using a dark-field image, on every pixel. The proper characterization of these noise sources are therefore challenging and quite involved and deemed to be beyond the scope of this work, however, this noise floor is measured.

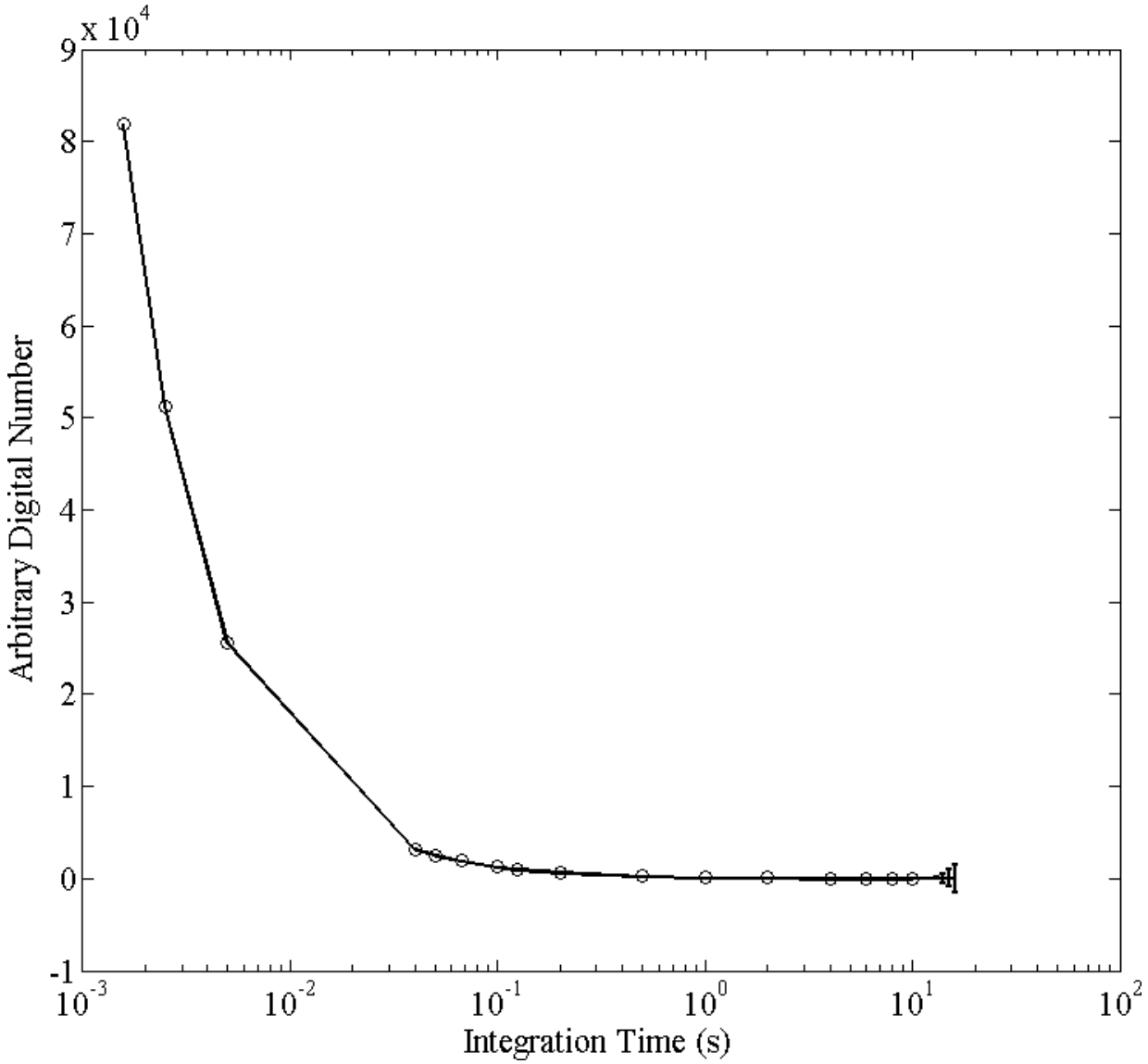

Figure 3.10: The mean noise level of the detector pixels at different exposure times. The variance on the mean is plotted as an error bar at every integration time. The variance is only noticeable at longer integration times.

Noise Floor

The concept of noise floor introduced here is to consider the consortium of all sources of noise as observed on the raw image output of the Pentax DSLR used in this work. To this end, a series of images, at different integration times, are captured with the camera aperture closed which prevents any light to be registered on the detector thereby suppressing any shot noise.

Figure 3.10 shows the mean noise level as a function of the exposure time. The noise level shown is identical across the collection of the three color, RGB, filters. The noise has a perfect power law distribution with a power of -1. The mean noise is lower at longer integration times however the variance is higher since hot pixels tend to diverge from the mean more readily and their effect is more pronounced.

The statistical tendencies, mean, median, and mode, of the noise level at a given integration time are identical. This suggests that the noise at a specific integration time has a uniform distribution and as postulated before can simply be considered to be a global offset to be negated from the captured image data.

Dead/Hot Pixels

Hot pixels are individual and isolated pixels on a detector array that tend to have higher than normal charge leakage. Every pixel on a detector has charge leakage which tends to increase with increasing integration time. However, there are some pixels on every detector that can have run-away charge leakage and are thereby deemed to be hot pixels.

The hot pixels of the Pentax DSLR are shown in Figure 3.11. There are a total of 27 hot pixels that have been detected in a dark frame with integration time of ten seconds. These pixels had a value that was in excess of 30 times larger than the mean value among more than six million pixels. The coordinate of these pixels are noted and the intensity value belonging to these pixels will be interpolated when performing observations.

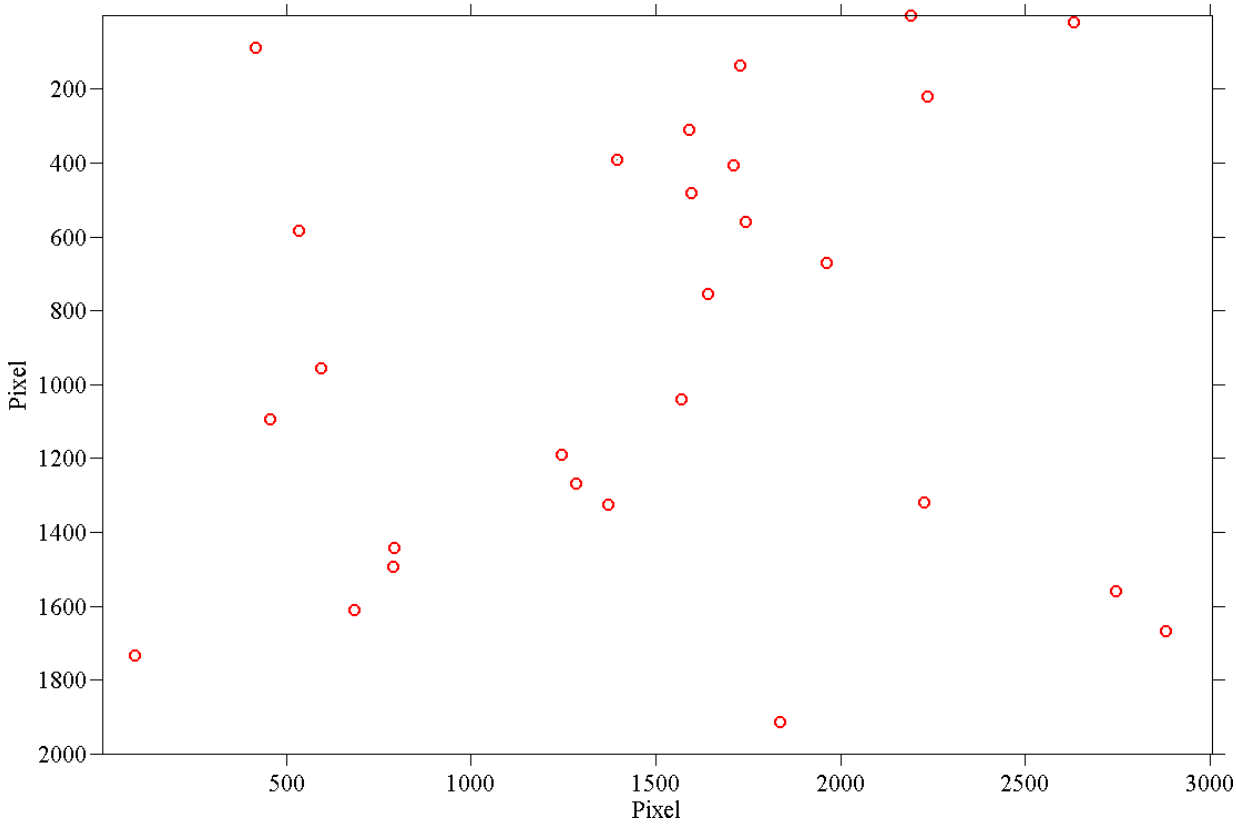

Figure 3.11: Hot pixels in Pentax DSLR CCD sensor array are identified.

Spectral Response

A high quality spectral imaging system has as many different detectors as the required spectral channels. In such an instrument, a collection of chromatic beamsplitters and spectral filters work in concert to separate out different spectral bands as the light propagates through the instrument on its way to the detectors to be recorded.

For cameras catering to the subjective sensation of colors catering to human visual system, the three primary colors, RGB, are required and sufficient. Through additive mixing any color can be created through the correct mix of the RGB color pallet. Therefore, in order to capture a color image of a scene, all three of the RGB spectral channels are required.

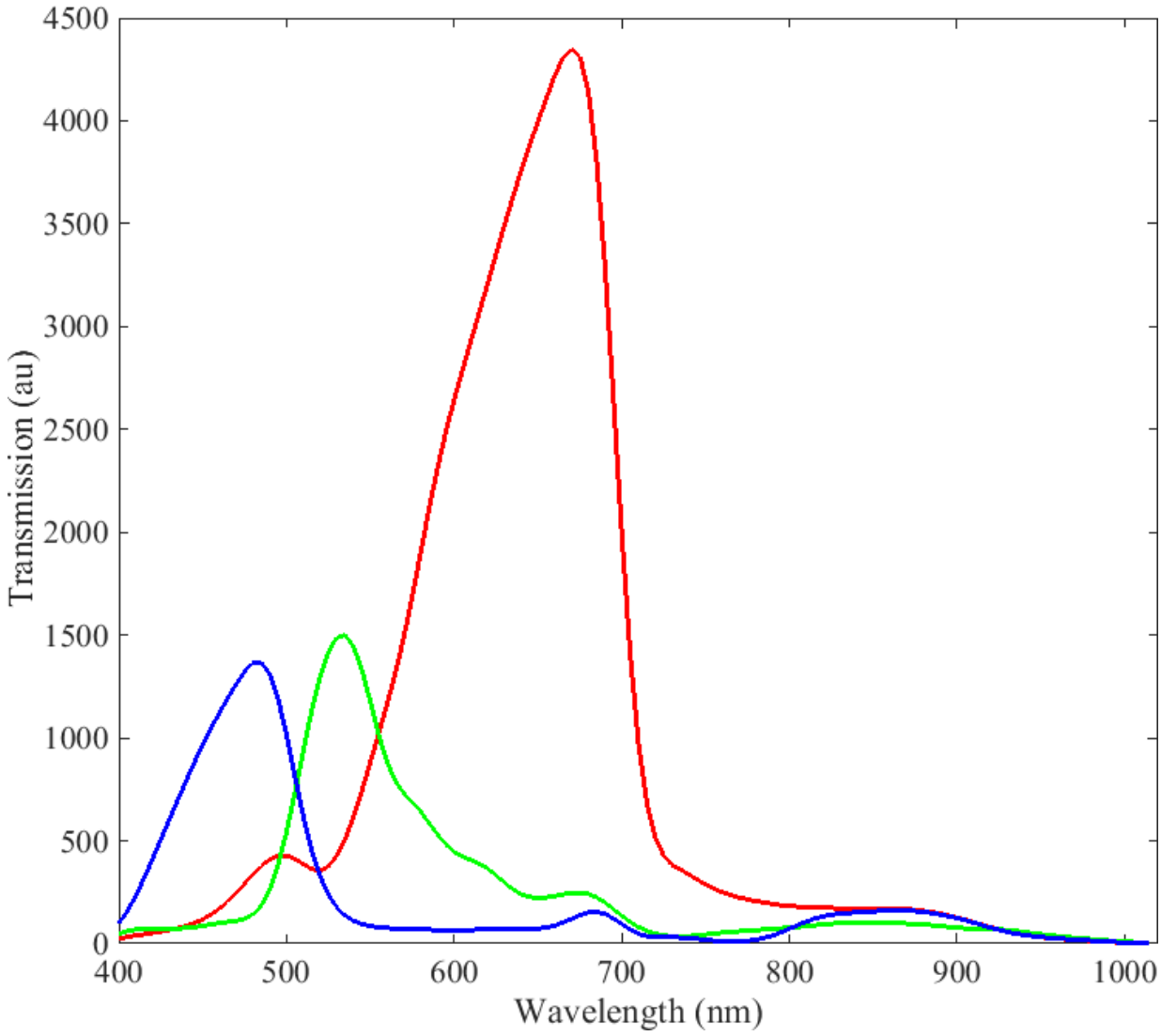

Figure 3.12: The spectral response curves of the RGB pixel-based filters integrated on the Pentax DSLR CCD. The blue, green, and red curves demonstrates the behavior of the blue, green, and red spectral filters, respectively.

Capturing the RGB channels of the same scene can be done using the types of high quality spectral imaging system. However, this is a costly and unnecessarily complex device. Rather than using such an instrument a selection of red, green, and blue color filters are integrated on the detector pixels to sample the corresponding region of the visible spectrum. These color filters are systematically mosaiced in groups of four and cover the entire detector, as in every pixel on the detector is sampling the light in one of these three colors.

Typically, in a foursome of pixels, arranged two by two, one pixel observes in the red region, two pixels in the green, and one pixel in the blue. This leads to a 25% total number of pixels sampling the red regions of the visible spectrum, 50% sampling the green, and 25% sampling the blue. This arises from the intricacies in the human vision system which uses the green portion of the spectrum to discern details and red and blue are used for color perception [56].

These three color filters, RGB, are designed to have peak performance in the corresponding visible regions of the electromagnetic spectrum and the peak central wavelengths and bandwidths varies by manufacturer. These filters, however, will have some response in the NIR region of the spectrum as well. In consumer cameras this effect is negated by the introduction of an NIR blocking filter which does not allow any light beyond $\sim$ 675 nm to propagate trough to the detector.

Understanding the spectral response of each of the RGB color filters is important in the context of this work. The relative spectral response of the RGB color filter are measured and shown in Figure 3.12. The area enclosed by each of the RGB channels is normalized to unity and the resulting characteristic spectral response curves are shown in Figure 3.13. Note that the spectral response curves in actuality are not very smooth, containing high frequency fluctuations superposed on the general trend. The curves shown in Figures 3.12 and 3.13 have been smoothed by convolving a Gaussian kernel (variance of 9 nm) with the raw data to act as a low-pass filter.

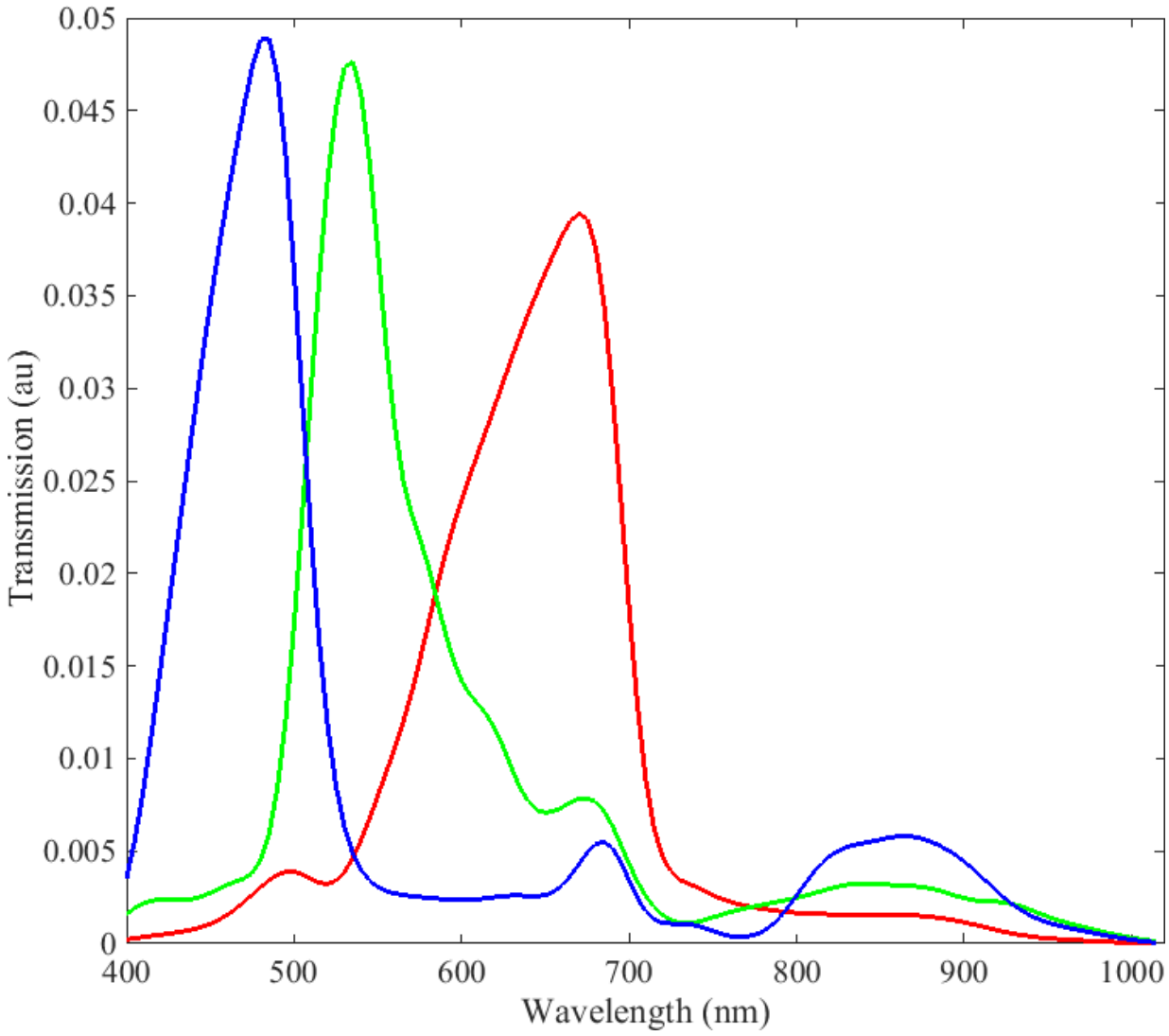

Figure 3.13: The normalized spectral response curves of the RGB pixel-based filters integrated on the Pentax DSLR CCD. The blue, green, and red curves demonstrates the behavior of the blue, green, and red spectral filters, respectively.

The spectral response, which is the relative acceptance of photons at a specific wavelength, is possibly the most important aspect of the instrumentation design and characterization. This property is measured by using the camera to image the exit pupil of a monochrometer.

A monochrometer is an optical device that can be tuned to transmit a narrowband of the spectrum, selectable from a region of the broadband radiation available. A Visible-NIR Czerny-Turner monochrometer [28] was designed and built for the purposes of measuring the spectral response of Pentax CCD and to estimate its quantum efficiency.

A Czerny-Turner monochrometer uses an exit slit placed at the effective focus of a spectrometer. By scanning the exit slit along the spectrum generated by the spectrometer, wavelength selection can be done. The light that then propagates from the exit slit will be a narrow band selection of the original broad band light beam that entered the spectrometer. The exit pupil can then be imaged using the camera and the image of the slit, at a specific wavelength, can be used to determine the transmission efficiency of the Bayer filter at that wavelength. The exit slit was scanned across the spectrum generated by the spectrometer at 5 nm intervals and the light propagating through the slit was observed using the camera.

Refer to Appendix A for more detail on the design specifications of the monochrometer and Appendix B for its usage procedures.

3.5 Multispectral Capability

The multispectral capability of the device is enabled when each of the POV of the imaging device travels through a field filter which transmits a specific region in the visible to NIR (400 - 1000 nm) wavelength range, and rejects the remainder. The light that is transmitted through the field filters is then allowed into the camera and convolved with the spectral response of the RGB filters that are part of the CCD pixels before it is registered and recorded by the camera.

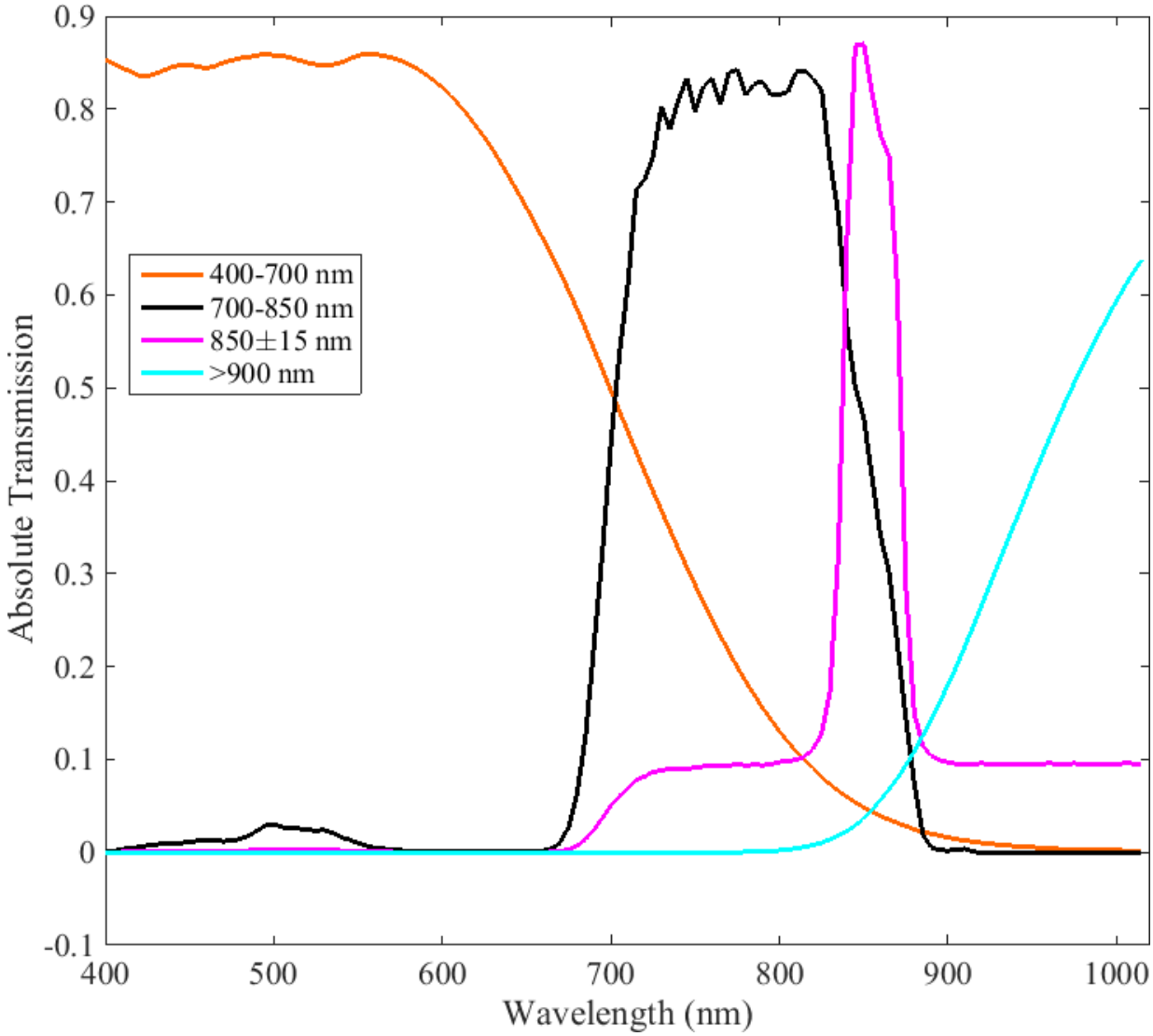

Figure 3.14: The transmission curves of the four field filters used in the system. The visible field filter 400 - 700 nm is shown in orange, and the three NIR field filters 700 - 850 nm, 850 ± 15, and 900+ nm are shown in black, magenta, and cyan, respectively.

3.5.1 Field Filters

The field filters are placed immediately in front of the entrance of the lens of the camera. According to Figure 3.14 there are a total of four filters used in the system as field filters. The filter whose transmission is shown in orange is more efficient in the visible portion of the spectrum and the filters shown in black, magenta, and cyan are more efficient in the NIR. Two out of the five POVs of the camera are both capable of making observations in the visible portion of the spectrum. The duplicated POV, in addition to a visible filter, may also be equipped with a linear polarization field filter. The uses and capabilities of this POV are not relevant to the topic of the work presented here and are deemed beyond the scope.

There are a total of five POVs in the system, four are capable of making measurements in four different wavelengths ranges. These ranges are 400 -700 nm, 700 - 850 nm, 835 - 865 nm, and 900 - 1000 nm. The fifth POV is designed to replicate the observations made in the visible range (400 - 700 nm). The spectral transmission capabilities of the field filters are not disjoint and there is ample overlap between spectrally adjacent channels. The combination of these four field filters with the RGB Bayer filters on the CCD will determine the final spectral channels and the transmission efficiency of each. This concept is discussed in detail in §3.5.2.

Location of the Field Filters

The field filters are arranged immediately in front of the lens of the camera and they are selected to allow a pre-determined wavelength range of the electromagnetic wavelength to enter the camera system. These filters are arranged in a filter holder which is designed to only operate on the light, from the POV, that is entering the camera from the appropriate field multiplying optical element.

3.5.2 Spectral Channels

The spectral channels that the system is capable of observing are convolutions of the transmission of the field filters with the transmission of the Bayer RGB filters on the

CCD pixels. Since the camera is designed to perform consumer-based imaging, the pixel-based filters are designed to have optimal performance in the visible wavelength range of the electromagnetic spectrum. The three blue, green, and red channels are distinctly separable from one another and with an introduction of an infrared blocking filter the three channels would have similar transmission efficiency.

Having removed the NIR blocking filter, there is access to this part of the spectrum, therefore understanding the behavior of the Bayer filters at these wavelengths is paramount and this has been measured and shown in Figure 3.12. Determining the possible spectral channels that can be distinctly measured using the system is done by convolving the transmission spectrum of the field filters and the transmission spectrum of the Bayer filters on the CCD.

Figure 3.15 shows the 12 (3×4) spectral channels as the result of the above-mentioned convolution from POVs I and II (a), III (b), IV (c), and V (d). The colored curves in the plots represent the respective Bayer filter response. Note the significant decrease in the arbitrary transmission value starting from Figure 3.15 a - d which is consistent with the QE of the CCD.

The pure transmission efficiency of the red filter in the POV I seems to be the highest, in actuality with the introduction of an NIR blocking filter with a cut-off wavelength at around 650 nm, the response of the red channel in the visible range would be comparable to the blue and the green channels in the same range.

An inspection of each of the channels in the spectral range determined by the field filters was carried out. A single-mode Gaussian curve was fitted to the efficiency curves and the central wavelength and full-width-half-maximum (FWHM), or spectral bandwidth, was determined. Table 3.1 shows the result of the fits for the RGB filter in each POV (I-V).

The purpose of this exercise is to find a combination of field filter and Bayer filter transmission spectrum which has a strong transmission efficiency at a "unique" wavelength. The definition of a 'unique' wavelength is a transmission curve that has one Gaussian-like peak and ideally no secondary or tertiary peaks larger than 50% of the maximum efficiency of the main peak. Also two adjacent peaks can be considered to be unique if they are separated by more than the half-width-half-maximum ($\frac{FWHM}{2}$) of one another, this imposed rule adheres and is analogous to the Rayleigh criterion on angular resolution [18].

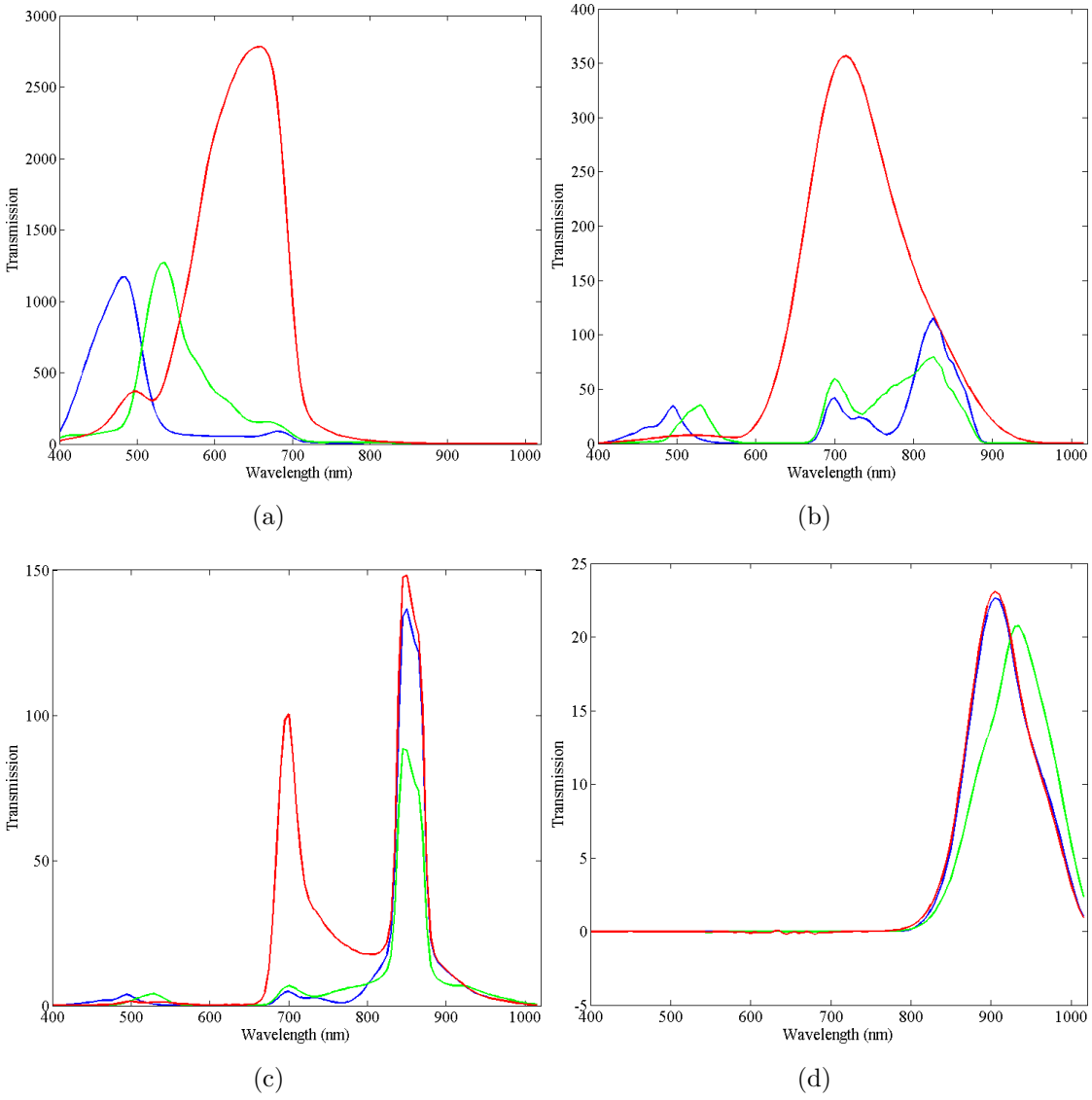

Figure 3.15: The spectral transmission of the Pentax CCD. In all plots the blue, green, and red curves correspond to the transmission behavior of the respective Bayer pixels in the spectral region determined by the field filter: a) 400 - 700 nm, b) 700 - 850 nm, c) 825 - 875 nm, and d) 900 - 1000 nm.

Table 3.1: The discrete spectral channels of the system deduced as a result of the combination of the field filters and the detector Bayer filters. A channel number has been assigned to the channels that will be used for future studies using the instrument. † According to Figure 3.15 these channels have multiple transmission peaks at relatively similar power, therefore their accurate transmission band could not be determined.

$POV_{Bayer\,filter}$	λ_c (nm)	$\pm\lambda$ (nm)	Channel#
I_B and II_B	473.3	44.69	CH1
I_G and II_G	540.1	48.32	CH2
I_R and II_R	635.3	69.60	CH3
$III_B^{\dagger}$	——	——	—
$III_G^{\dagger}$	——	——	—
III_R	705.1	62.13	CH4
IV_B	854.4	21.10	CH5
IV_G	853.6	21.26	—
$IV_R^{\dagger}$	——	——	—
V_B	912.1	58.36	—
V_G	932.9	62.27	CH6
V_R	910.8	57.88	—

The channels that have been deemed suitable for use in the multispectral instrument are given channel number 1 - 6. In POVs I and II, the three blue, green, and red channels are completely separable and can therefore be considered to be independent spectral channels, CH1, CH2, and CH3. In POV III, the blue and green channels have extremely low transmission as well as having two peaks at similar relative transmission and there therefore deemed to be unusable. In POV III, the red channel, however, has a very strong and defined peak and will therefore be used as CH4. In POV IV, the red channel has two relatively strong peaks and is not usable. The blue and green channels in the same POV have almost identical transmission wavelengths, however the blue channel has a slightly higher peak, hence, it has been chosen as CH5. In POV V, the blue and red channels have similar transmission central wavelength and peak and both do not satisfy the separability criterion previously mentioned thus, the green channel was selected as CH6. The spectral

characteristic of the six channels selected for operational purposes of the system and the proposed work are shown in Figure 3.16.

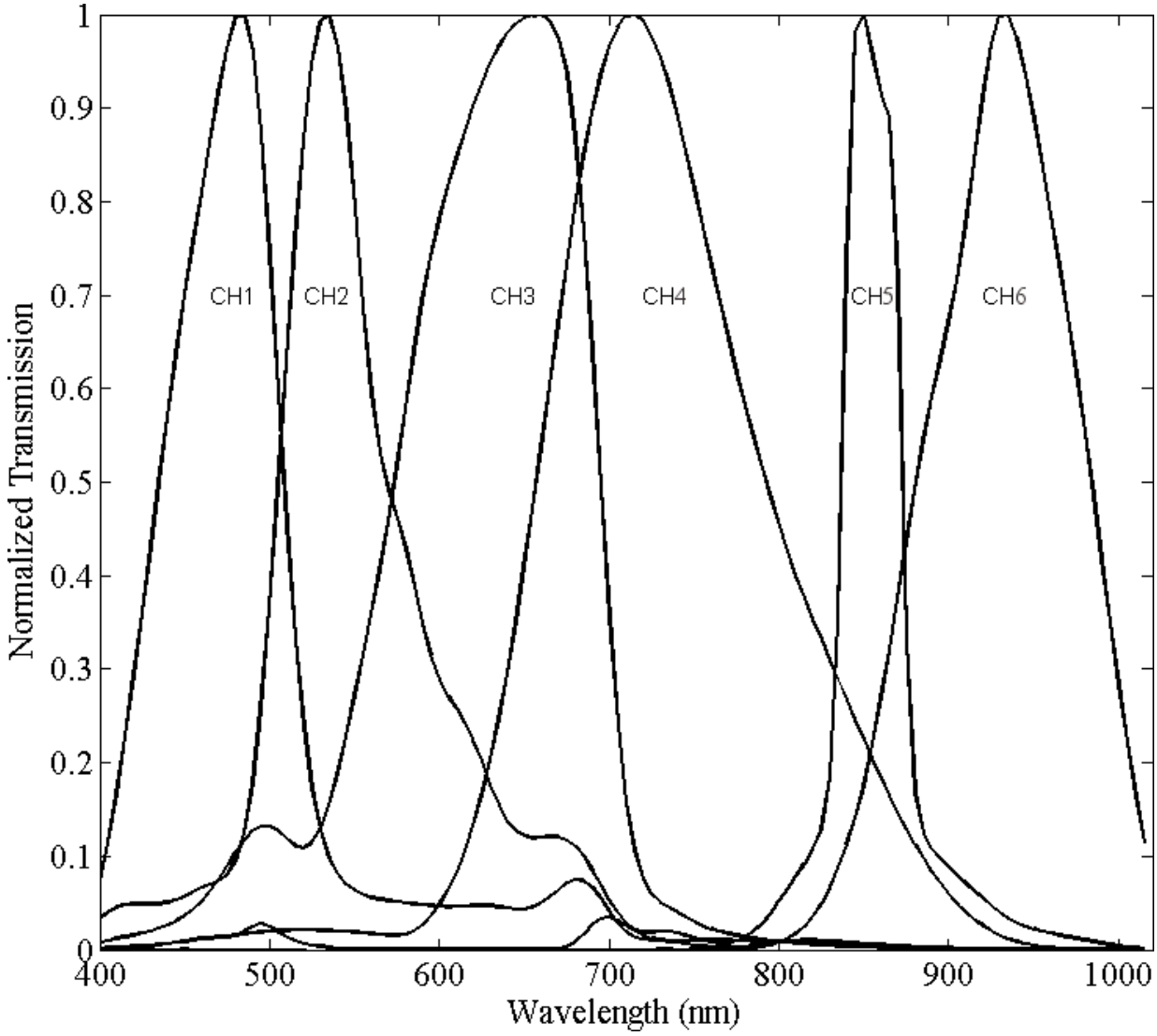

Figure 3.16: The size spectral channels selected, the transmission efficiency of all channels have been normalized. The channels number corresponds to the spectral properties quoted in Table 3.1.

3.6 Discrete Spectral Imaging Attachment Design

The multispectral imaging capabilities proposed in this work can be enable by coalescing any camera, lens and detector combination, with the discrete spectral imaging (dSI) attachment proposed in this section and designed as described in previous sections of this chapter. The optical schematic of the system is shown in Figure 3.17. The specific parts used in the system presented here are listed in Appendix C. The mirrors in the replicating device are used to steer the light from the object that would have otherwise missed the camera into the camera. The light presented by the mirrors then travel through bandpass filters which filter out different portions of the spectrum, determined in previous section, on the way to the imaging device. The five separate POVs are then imaged at different location of the detector, as shown in Figure 3.18, and recorded for post-processing.

The dSI attachment can be adapted to any camera system, consumer or scientific, using a locking adapter similar to the one shown in Figure 3.19. The adapter ring shown here is specifically designed to lock on to the Pentax DSLR's hood locking mechanism.

The filter holder module, Figure 3.20, would connect to the adapter ring which would then be placed immediately in front of the camera lens. The spectral filters have to be cut to size in order to fit within the appropriate compartment just so they are covering the appropriate size and location of the FOV of the camera corresponding to the correct POV presented by the replicating optics.

The replicating optics module is the last module in the dSI assembly which houses the mirrors required for this process. The mirrors are at a distance of $\sim$ 90 mm from the camera lens and $\sim$ 90 mm from the location of the sample. This module has also been designed with many connection points that would allow the inclusion of equipment such as specialized light sources, an SMA fiber adapter holder to couple a light source delivered via an optical fiber, etc.

One of the most important design aspects of the attachment is the fact that it has to be relatively light to be easily integrated into the camera yet strong enough to hold all of the necessary optics in place. Also, with the unique physical design of the attachment itself, such as the locking mechanism between different modules, the specific angle of the slots holding the replicating optics, and generally the specialized design fabricating such an object was a great challenge. To this end, 3D printing was deemed to be the most

appropriate tool for producing such an object as other machining techniques would have fallen short in producing something of such high tolerance and unique and unusual design specification.

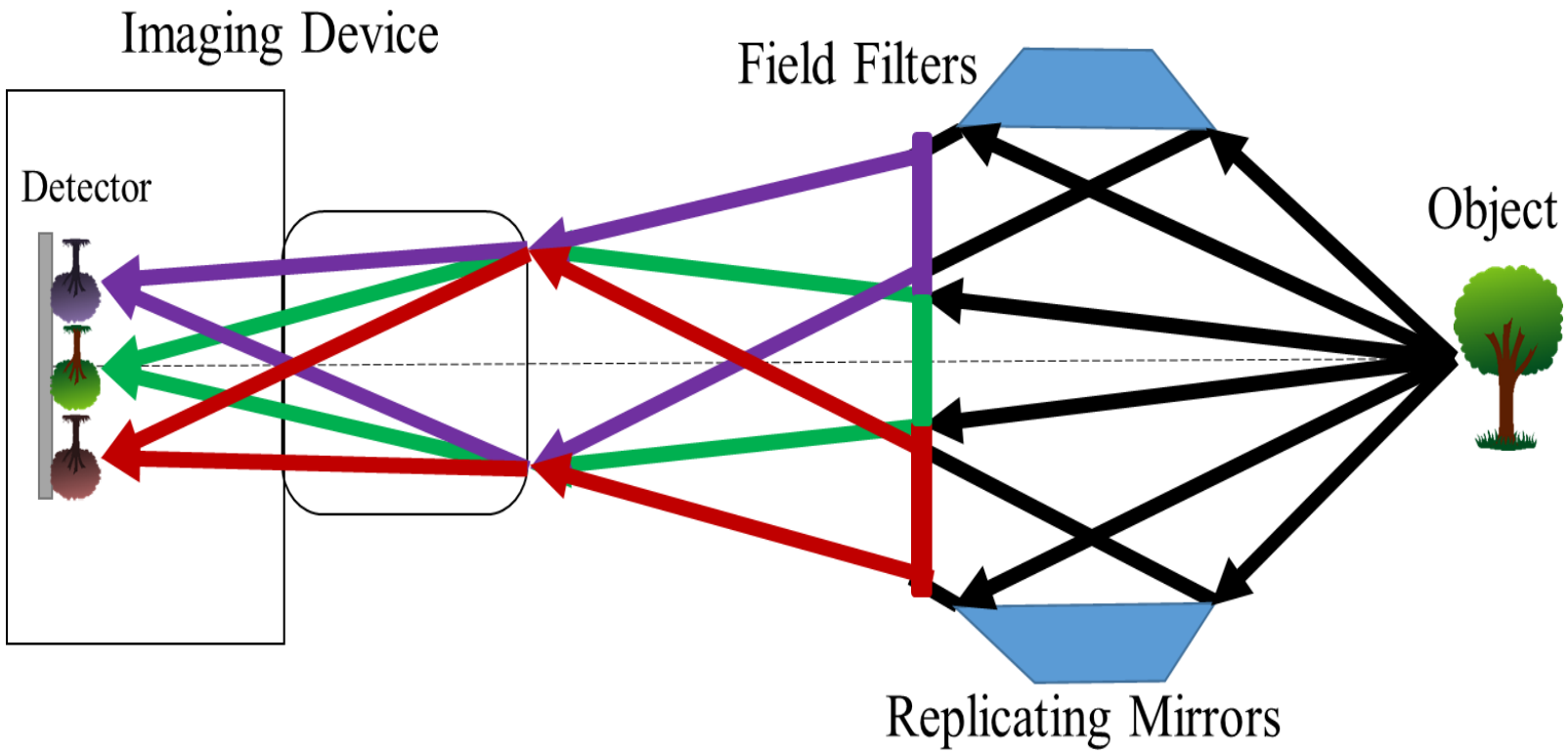

Figure 3.17: The optical schematic of the proposed system. This schematic is representative of the top and side views of the system as they are symmetric. The light from of the object, in the schematic is replicated by the mirrors and directed through spectral filters to the imaging device where they are recorded as images in a specific spectral range.

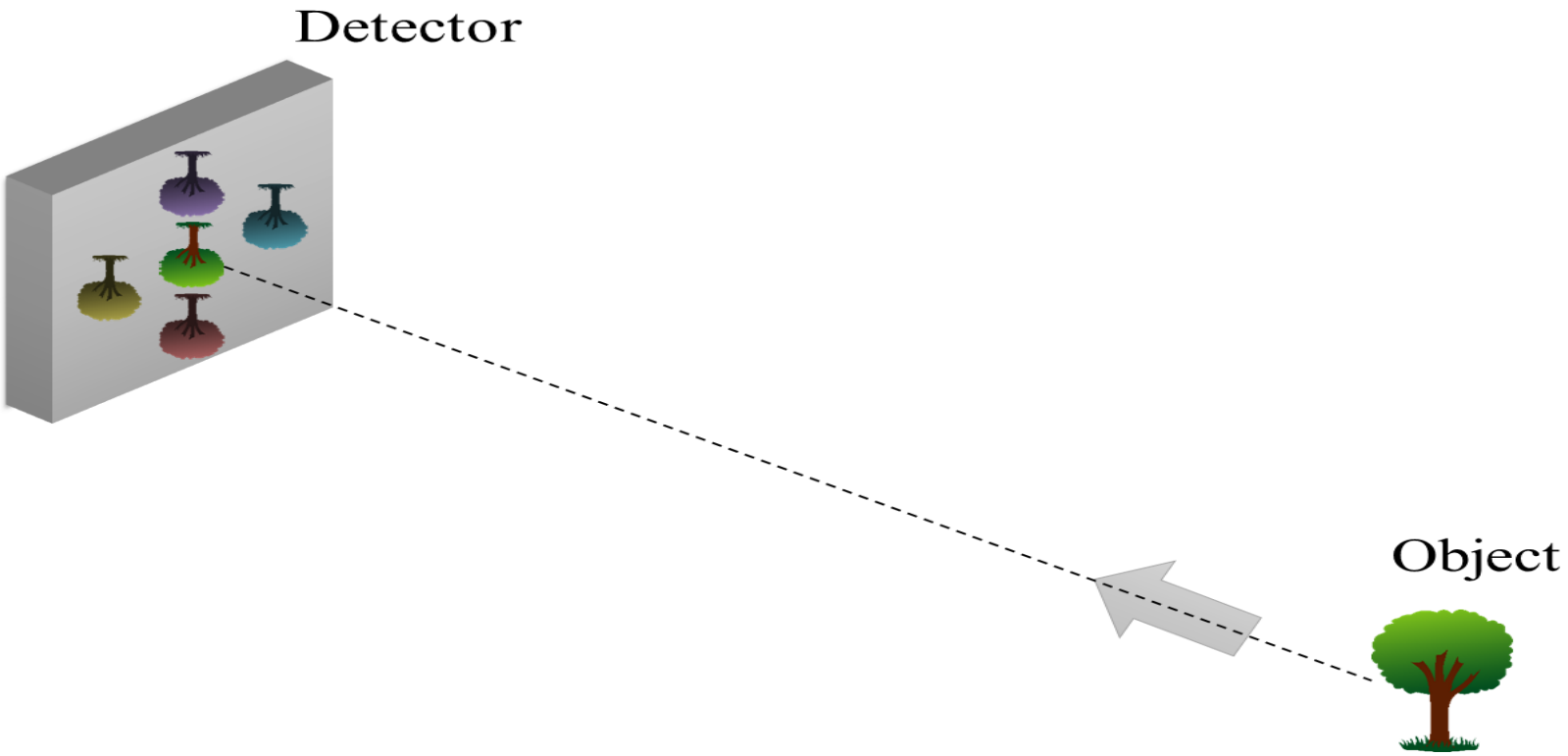

Figure 3.18: The schematic of how the distribution of the FOV being imaged on the sensor. The five POVs are separated spatially from one another with no interference. The colorization of the images observed in the FOVs are of no particular meaning and are for illustrative purposes only.

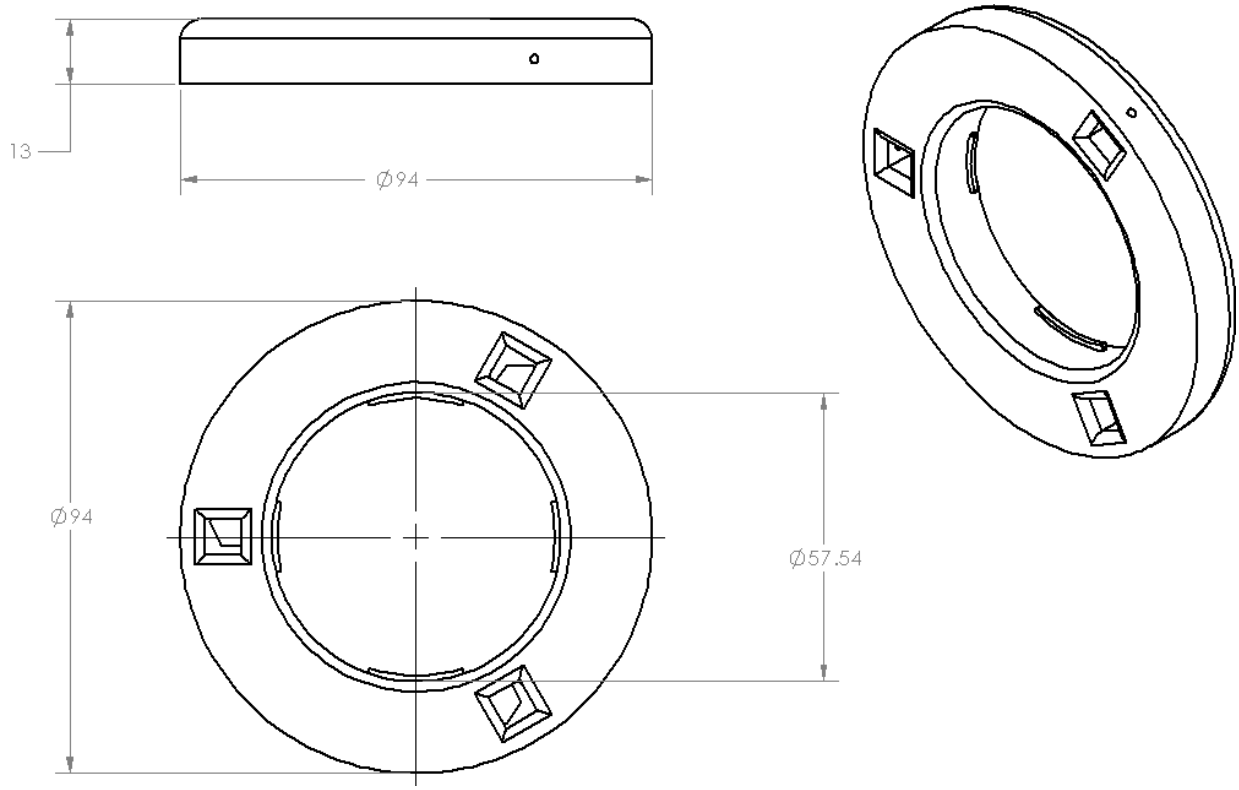

Figure 3.19: The dSI adapter ring which facilitates the connection of the dSI attachment to the DSLR camera. All dimensions are in millimeters.

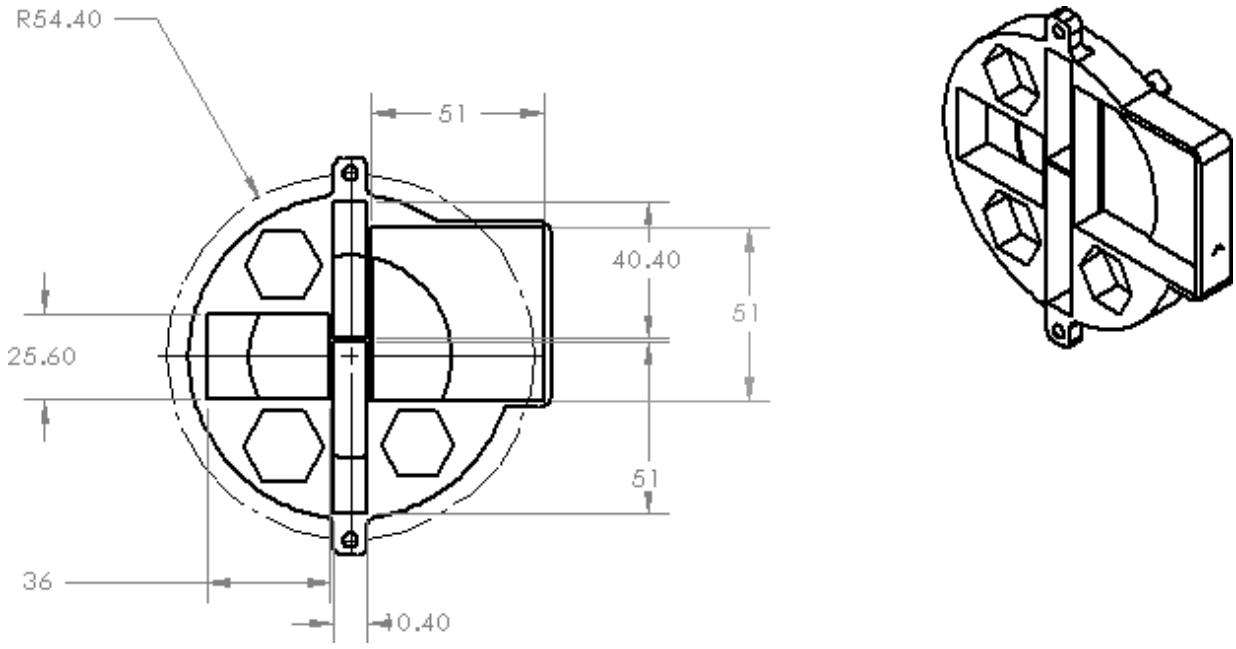

Figure 3.20: The filter holder module of the dSI system where the spectral filters are located and help in place in front of the camera lens. All dimensions are in millimeters.

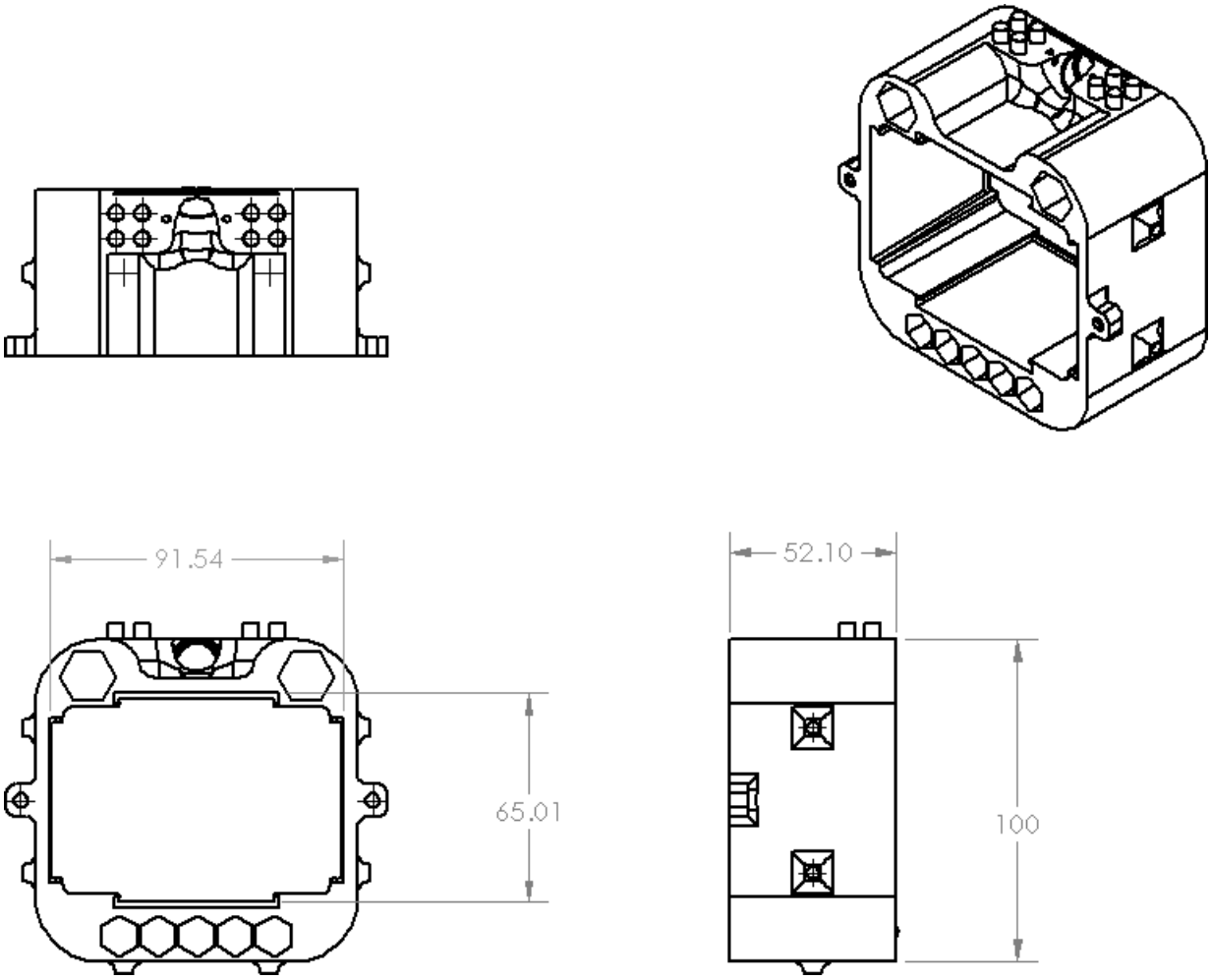

Figure 3.21: The replicating optics module of the dSI system. This component has been designed to allow for addition modular attachments such as various light sources. All dimensions are in millimeters.

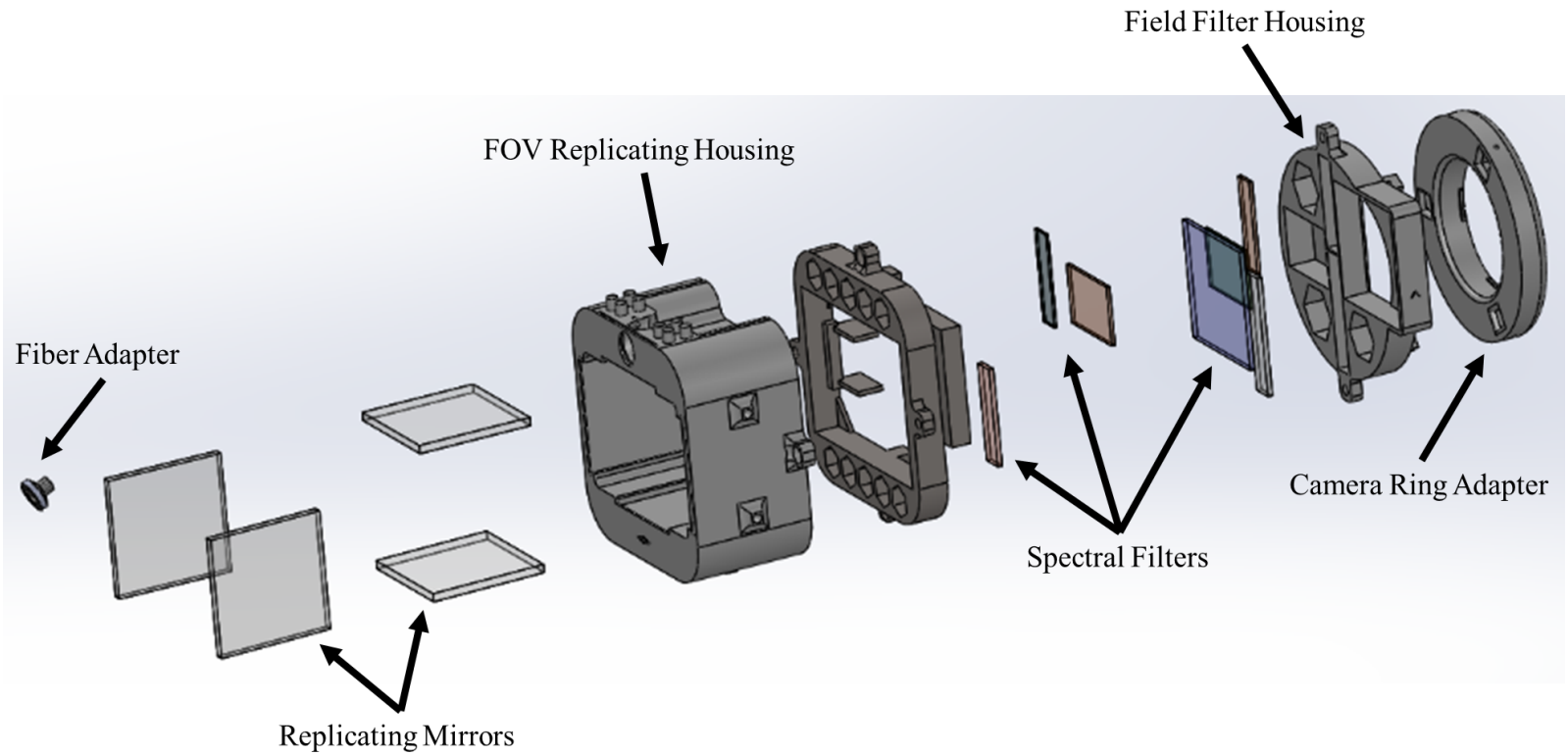

Figure 3.22: The exploded view of the camera attachment that enables multispectral imaging across the visible and the near-infrared. The components include, from left to right: an SMA fiber adapter, replicating mirrors, the housing for the replicating optics and light sources, filter housing lid, various spectral filters, filter housing, and the camera adapter ring.

The material that the printing was done with is Polycarbonate-Acrylonitrile Butadiene Atyrene. The print was done using a Stratysis Fortus 380MC 3D printer with lateral resolution of $\sim 90\ \mu m$ and axial resolution or layer thickness of $\sim 130\ \mu m$ [115]. The entire print, shown in Figure 3.22, took 24 hours to complete and an additional 24 hours to cure and dry. Figure 3.22 shows the dSI attachment in its totality including all of the mirrors and spectral filters. This attachment once assembled can simply be used in combination with any imaging device and it will therefore enable simultaneous multispectral imaging.

Chapter 4

Computational Compressive Sensing

The optical hardware design presented in the previous chapter requires the accompaniment of some software algorithms to enable the system to function as proposed. First, the spectral images captured in each of the POVs will have to be aligned for the purposes of performing multispectral analysis. In other words, if multispectral properties of a single pixel is to be considered, the radiometric response of corresponding pixel in each of the POVs will have to be determined. Second, since multispectral sensing is being done via a compressive sensing technique, not every pixel has a true measurement at all spectral channels available in the instrument, therefore, the missing radiometric value of each pixel in every spectral channels will have to be estimated. Third, the field replicating optical design introduces a slight optical path difference between the different POVs which can act to defocus the captured image in that POV. To this end a numerical focusing technique has been implemented to find the best focus for each of the POVs. Lastly, principal component analysis will be carried out using the multispectral information to extract information that may aid in classification of various samples. The computational image processing discussed in this chapter is implemented in MATLAB[1].

[1]MATLAB® is a high-level language and interactive environment for numerical computation, visualization, and programming. It is a registered trademark of Mathworks Inc.

4.1 Registration of Multispectral Images

In many imaging applications where the object is non-stationary and the imaging is multi-temporal or multispectral, it is crucial to align the images before any processing, analysis and interpretation can take place. This alignment process is often referred to as registration in the field of image processing [47, 53, 116].

In its most generic form image registration is simply a geometrical transformation of the image array governed by specific matrix operations simply carried out by

$$\mathbf{T}(x_i, y_j, z_{ij}) = \mathbf{A}\ \mathbf{f}(x_i, y_j, z_{ij}), \tag{4.1}$$

where $\mathbf{T}(x_i, y_j, z_{ij})$ is the transformed image resulting from multiplication of the transformation operator, $\mathbf{A}$, by the original image $\mathbf{f}(x_i, y_j, z_{ij})$, where x_i, y_j, and z_{ij} are the i^{th} and j^{th} pixels in the vertical and horizontal direction with their corresponding intensity value, respectively. In actuality, images are three-dimensional as the third dimension is the intensity level, or the grayscale value, at each pixel however image registration is a spatial process and should not affect pixel intensity unless some interpolation is imposed after registration in order to estimate the missing values in pixels that have been placed within the registered image.

The transformation operator matrices, used in this work, for various geometric operations are listed below:

- Mirror in the x-direction

$$\begin{bmatrix} -1 & 0 & 0 \\ 0 & 1 & 0 \\ 0 & 0 & 1 \end{bmatrix}; \tag{4.2}$$

- Mirror in the y-direction

$$\begin{bmatrix} 1 & 0 & 0 \\ 0 & -1 & 0 \\ 0 & 0 & 1 \end{bmatrix}; \tag{4.3}$$

- Scaling

$$\begin{bmatrix} s_x & 0 & 0 \\ 0 & s_y & 0 \\ 0 & 0 & 1 \end{bmatrix}; \tag{4.4}$$

- Translation

$$\begin{bmatrix} 1 & 0 & t_x \\ 0 & 0 & t_y \\ 0 & 0 & 1 \end{bmatrix}; \tag{4.5}$$

- Shear

$$\begin{bmatrix} 1 & u_x & 0 \\ u_y & 1 & 0 \\ 0 & 0 & 1 \end{bmatrix}; \tag{4.6}$$

- Rotation

$$\begin{bmatrix} cos\theta & -sin\theta & 0 \\ sin\theta & cos\theta & 0 \\ 0 & 0 & 1 \end{bmatrix}. \tag{4.7}$$

In the most general case, an 'affine' transformation which is dependent on six parameters is performed which combines all of the above-mentioned transformations

$$\begin{bmatrix} w_{11} & w_{12} & t_x \\ w_{21} & w_{22} & t_y \\ 0 & 0 & 1 \end{bmatrix}, \tag{4.8}$$

where w_{nm} is a value determined by the combination of any of the transformations necessary to register two images.

One of the main outcomes of the FOV replicating unit in the proposed instrument is the fact that the five spectral images captured by the camera are all slightly misaligned, or geometrically transformed. This misalignment manifests itself in the different spatial address for corresponding pixels in each spectral channel. Therefore, the spectral images from the five POVs have to be registered to a super-image of a common spatial grid for the purposes of performing multispectral analysis. This registration step would ensure that the pixel address of the images in each of the five POVs correspond even though there may exist no measurement at a given pixel in a given POV. The registration step is carried out with out any interpolation meaning the pixels that do not have any measurement will remain vacant and the pixels in the super-image that did not have a POV image pixel registered to them will also remain vacant. The absence of measurements in the super-image gives

rise to the compressive sensing nature of the proposed system and will be addressed by interpolation techniques discussed in the next section.

The main transformations that the POVs experience are reflection, rotation, and translation. These are easily corrected using various image processing software, in this case MATLAB. Although there may exist some scaling transformation as a result of defocusing of the POVs, it can be assumed that the effect is minor and therefore negligible. The registration process for the data captured using the system can be performed in two stages. The first stage will address the reflection transformation and the second will address the more computationally intensive rotation and translation.

The reflection transformation can be simply performed by producing the reflection image of each POV about the correct mirroring axis. Figure 4.1 shows the five POVs as observed by the instrument as well as their respective reflection axis, A for II, B for III, C for IV, and D for IV.

The rotation and translation transformations, most generally represented as

$$\begin{bmatrix} x' \\ y' \\ z' \end{bmatrix} = \begin{bmatrix} cos\theta & sin\theta & t_X \\ -sin\theta & cos\theta & t_Y \\ 0 & 0 & 1 \end{bmatrix} \begin{bmatrix} x \\ y \\ z \end{bmatrix}, \tag{4.9}$$

can be determined using two methods: automatic or semi-automated registration.

4.1.1 Automatic Registration

This form of registration uses the inherent properties in the images to be aligned and calculates the transformation matrix (Equation 4.9) based on these properties. An intensity-based image registration technique was used that uses the relative intensity patterns in the pixels of the images to find the correct transformation that would align certain pixels in each image to the same location based on relative intensity patterns. The goodness of the alignment, which may be an evaluation of entropy between the two images being aligned, is calculated and is set to be minimized for the most appropriate transformation parameters. The MATLAB implementation of this registration technique, *imregister*, was used to perform the automatic registration.

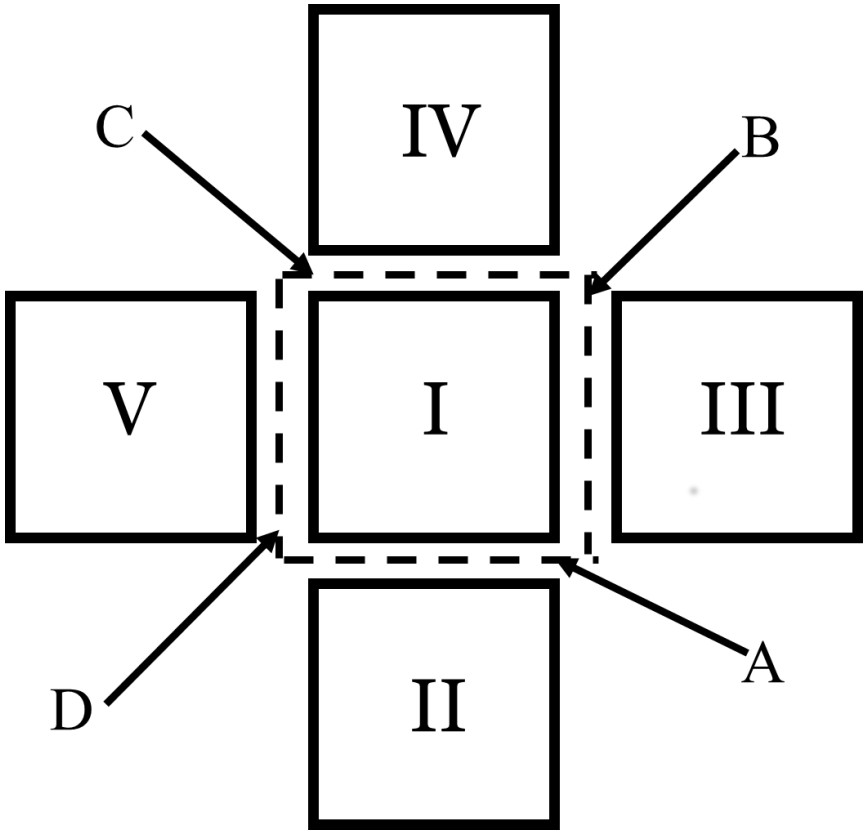

Figure 4.1: The five POVs with their respective reflection axes as seen by the system.

This method was tested to perform registration of the checker pattern shown in Figure 3.6, which are the original unregistered images captured by the instrument proposed in this work. The registration was carried out to align POVs II, III, IV, and V to POV I since the image observed in POV I is a real image and not the result of the FOV replication process. Figure 4.2 shows the outcome of the automatic registration process.

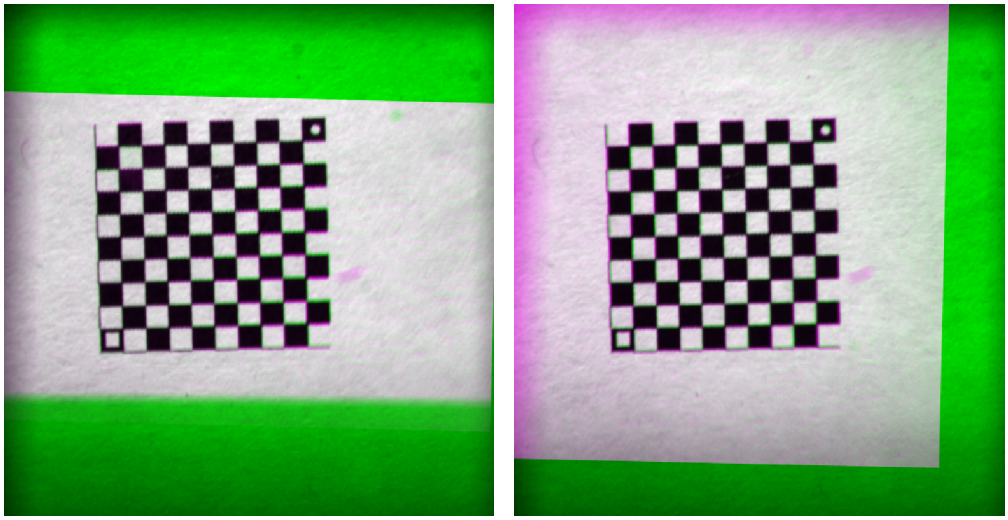

(a) II to I

(b) III to I

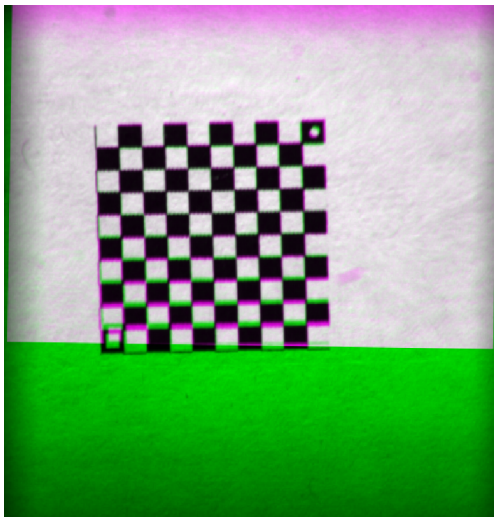

(c) IV to I

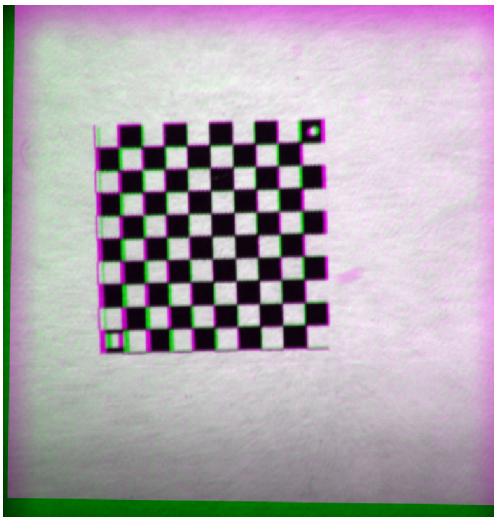

(d) V to I

Figure 4.2: The registration results from the automatic registration process. The individual figure caption denote the POVs that are registered to POV I.

The sub-images shown in Figure 4.2 are the result of overlaying the base image POV I, colorized in green, and the moving images POV II-V, colorized in magenta. The solid color section of the images are locations where data was not available in either one of the base or moving image, nonetheless, the region of interest, the checker pattern, is observed in its entirety in all POVs. There are some registration errors present with the automatic method as there appears to be some green or magenta edges within the checker pattern.

The error associated with the automatic registration are presented in Table 4.1. The errors evaluated are the Euclidean distance between the intersections points of the checkerboard pattern of POV I, shown in Figure 4.3, and the other POVs registered.

The automatic registration seems to perform adequately with registration misalignment of approximately three to five pixels in the worst case and approximately one pixel and possibly less than a pixel in the best case, for a target with well defined structure, such as the one used here.

Table 4.1: Registration error resulting from the manual and automatic registration process. The error is described as the distance, in pixels, between the intersection points of the checkerboard pattern as described in POV I and the registered intersection point from the other POVs. The errors resulting from the manual registration are less than one pixel in all cases whereas the errors resulting from the automatic registration can be as large as five pixels.

POVs	Manual Registration Error (pixels)	Automatic Registration Error (pixels)
II to I	**0.29 ± 0.14**	1.37 ± 0.82
III to I	**0.59 ± 0.28**	1.23 ± 0.49
IV to I	**0.33 ± 0.12**	2.79 ± 1.96
V to I	**0.43 ± 0.25**	2.50 ± 1.39

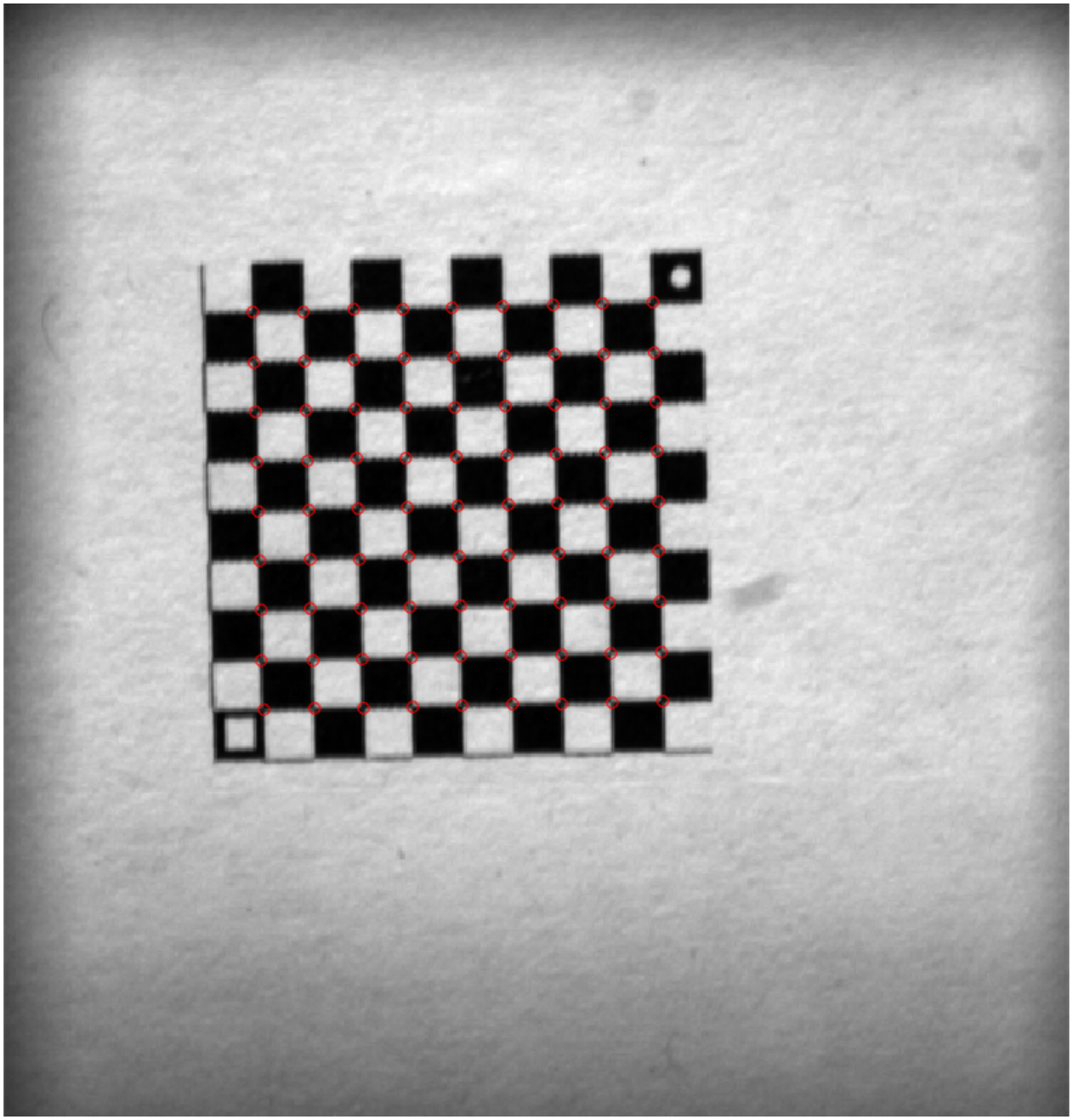

Figure 4.3: The checkboard pattern as seen in POV I with the intersection point denoted.

4.1.2 Manual Registration

The automatic registration perform relatively well aligning the five POVs if and when, all are in the same spectral region. However, when the spectral pre-filters are used and therefore the images in the five POVs are radiometrically different, the automatic registration may be sub-optimal for proper registration. Note that the automatic registration uses the intensity values of pixel neighborhoods to determine the appropriate transformation matrix and these pixel values and their radiometric characteristic may be vastly different in different spectral ranges across visible and NIR. Additionally, it is ideal to have registration errors of less than a pixel to increase the accuracy of the radiometric information.

To address the points raised above, a manual registration process can be employed where user intervention is required. The aforementioned intervention is in the form of selecting < 15 control points between the reference image POV I and the images to be registered POV II-V. Since the information in each POV will be unique, in the spectral dimension, user intervention is required to find corresponding pixel location which may otherwise be impossible for an automated algorithm to discover. The control points are then used to calculate a transformation matrix that would register the two POVs.

The control points are selected using 'The Control Point Selection Tool', *cpselect* command in MATLAB. Using these corresponding location pairs, a geometrical transformation matrix can be calculated using the local weighted mean of the projective transformation [49] implemented as *cp2tform* script in MATLAB. Finally, each pixel location in the captured image is transformed by the transformation matrix evaluated into the new grid space using the *imtransform* script in MATLAB, the geometrical transformation is performed to correctly registering the four POVs to POV I. Figure 4.4 shows the result of the manual registration process and Table 4.1 summarizes the registration error.

The accuracy of this method is astonishing compared to its automatic counterpart. Manual registration is successful at aligning two images with the accuracy of less than a pixel as seen in the Euclidean distance represented as the registration error.

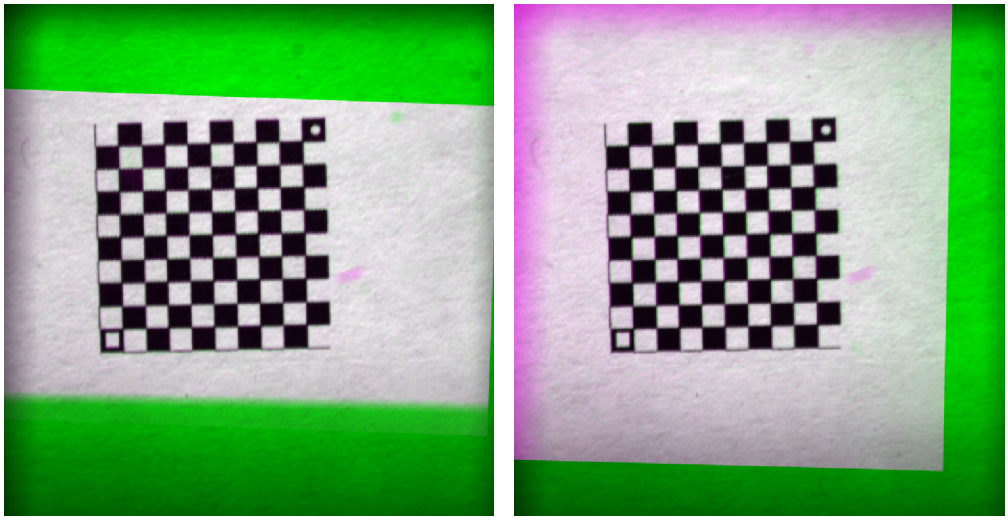

(a) II to I

(b) III to I

(c) IV to I

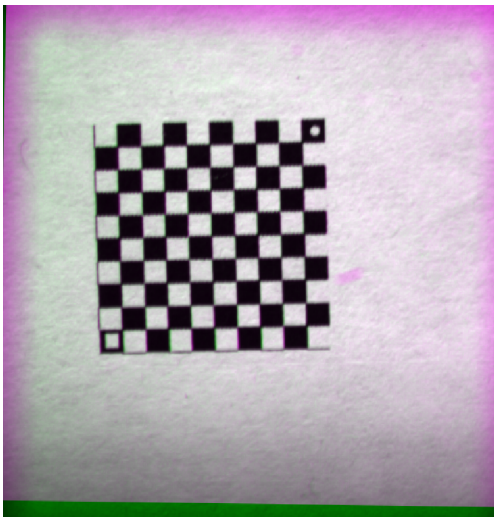

(d) V to I

Figure 4.4: The registration results from the manual registration process. The individual figure caption denote the POVs that are registered to POV I.

Registration is a unique procedure for every data set captured since the conditions under which the images are captured, such as the orientation of the camera and more importantly the distance between the camera and the sample, can differ. This data acquisition setup can be referred to as the 'non-assisted' setup and would require the control point selection in the registration process to be carried out. However, data acquisition can be performed using an 'assisted' setup which means a distance and orientation guide is attached to the camera that would ensure that the orientation of the camera and most importantly the distance between the camera and the target is constant in every acquisition. This way a preset set of control points can be recalled and used for registration and manual selection of control points will no longer be required.

4.2 Interpolation of Compressive Sensed Multispectral Images

Compressive sensing techniques require the accompaniment of advanced interpolation algorithms to estimate the missing information. The traditional interpolation algorithms used for the Bayer color filter array, referred to as demosaicing, will not be adequate for use with compressively sensed data for two reasons: 1. they use information from all spectral channels to interpolate the missing information in a given channel [2, 38]; 2. they are specifically designed to work with relatively dense datasets therefore the accuracy of interpolation of sparse data will be extremely low [125].

The mainstream demosaicing algorithms when applied to compressively sensed data fail to produce satisfactory results and tend to introduce many artifacts such as excessive blurring, zipper effect, discoloration, and false coloring [2]. Additionally, these algorithms do not maintain the spectral fidelity of the multispectral images and therefore render the data useless for any spectral analysis.

There is a very comprehensive presentation of all interpolation algorithms for various compressive sensing multispectral imaging techniques in a work by Lapray *et al.* [73]. These techniques range from simple non-iterative linear approaches to iterative Bayesian approaches. It is however suggested, by Lapray *et al.*, that no one algorithm seems to work

well with all compressive sensing multispectral data generating hardware as the algorithms have to be carefully tuned and guided for different applications.

To address the shortcomings of the above-mentioned algorithms, a series of algorithms have been proposed, by the author, which function based on an iterative Bayesian maximum a posteriori approach using conditional random fields to perform the multispectral interpolation [66, 75, 76], the multilayered conditional random field and the inter-spectral multilayered conditional random field. Both of these algorithms completely maintain the spectral fidelity of each of the image channels and are capable of producing high-contrast, sharp images that preserve edge information and do not require any tuning.

As previously mentioned in order to preserve the spectral fidelity of the images captured the automatic demosaicing of the imaging device will have to be circumvented. The raw detector pixel readout is shown in Figure 4.5. In Figure 4.5 shows a specific region in the checkerboard pattern imaged. It is clear that a color sensor, equipped with a Bayer filter is essentially a compressive sensing detector as only 25% of the pixels are equipped with red and blue filters and 50% of the pixels are equipped with a green filter.

In Chapter 3, it was demonstrated that the color filter array on the detector of the camera used allows for transmission in the NIR region of the electromagnetic spectrum. Exploiting this property three NIR channels were devised and the imaging system was designed to capture independent images in six spectral channels across the visible and the NIR wavelength region. To Evaluate the multispectral properties at a specific spatial location the POVs, each measuring a unique wavelength channel, are registered. The process of registration will introduce further sparseness into the data since the registration is carried out with sub-pixel precision.

Figure 4.6 shows the six spectral channels of the same region of the checkerboard pattern after sub-pixel registration. The white pixels in the spectral images are pixels where no information exists and the black pixels contained actual measurements. Table 4.2 summarizes the amount of pixels in the regions of interest with actual measurements.

Table 4.2: Spectral sparseness of the measurement in the region of interest in the checkerboard patter.

Channel	Available Measurements
1	3%
2	6%
3	3%
4	2%
5	2%
6	4%

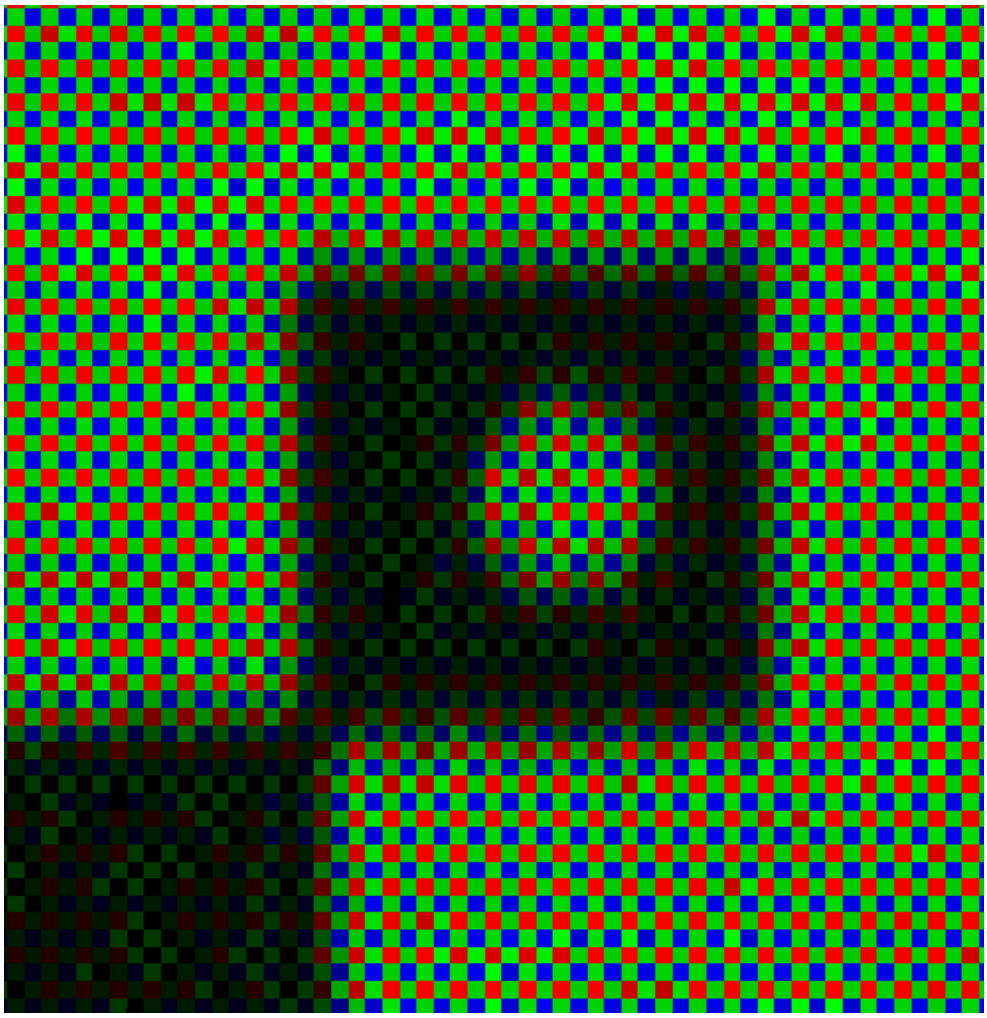

Figure 4.5: The raw image captured using the system, with the red, green, and blue pixels color-coded.

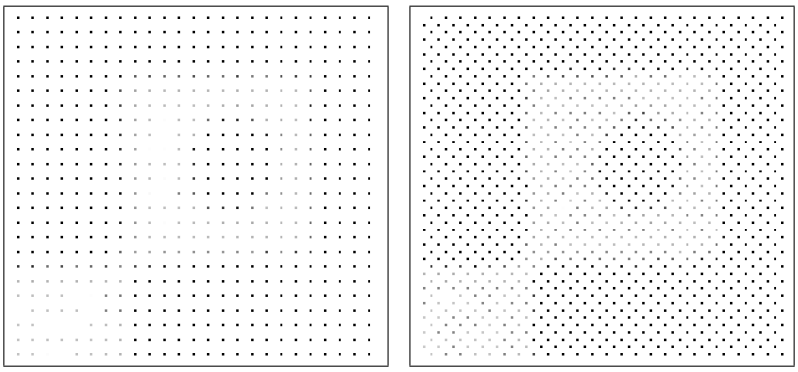

(a) CH1

(b) CH2

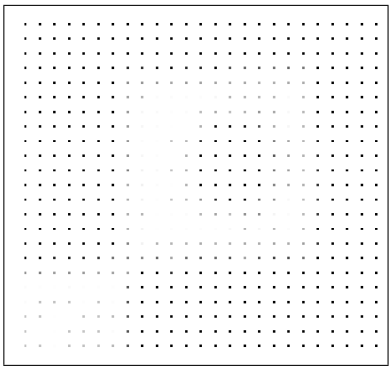

(c) CH3

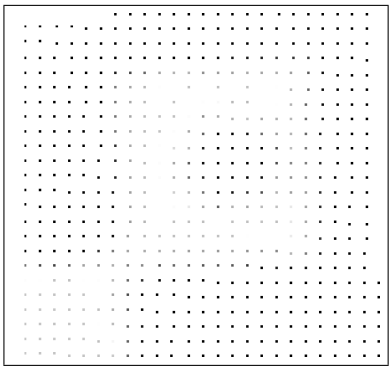

(d) CH4

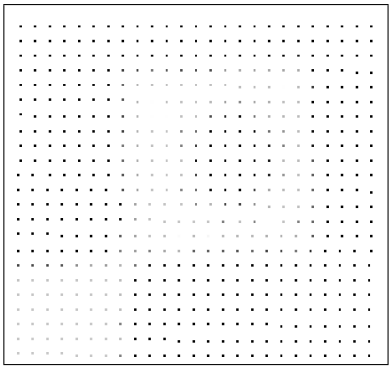

(e) CH5

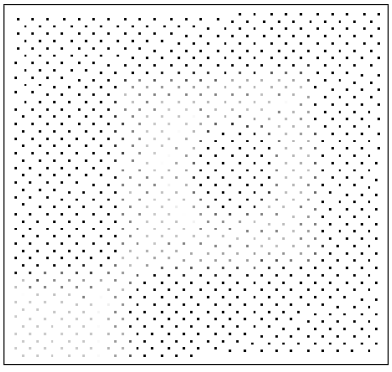

(f) CH6

Figure 4.6: A region of the checkerboard image is shown in the six spectral channels after registration of the raw images captured. The white pixels denote locations where no data exists and the black pixels are actual measurements made in the corresponding channel.

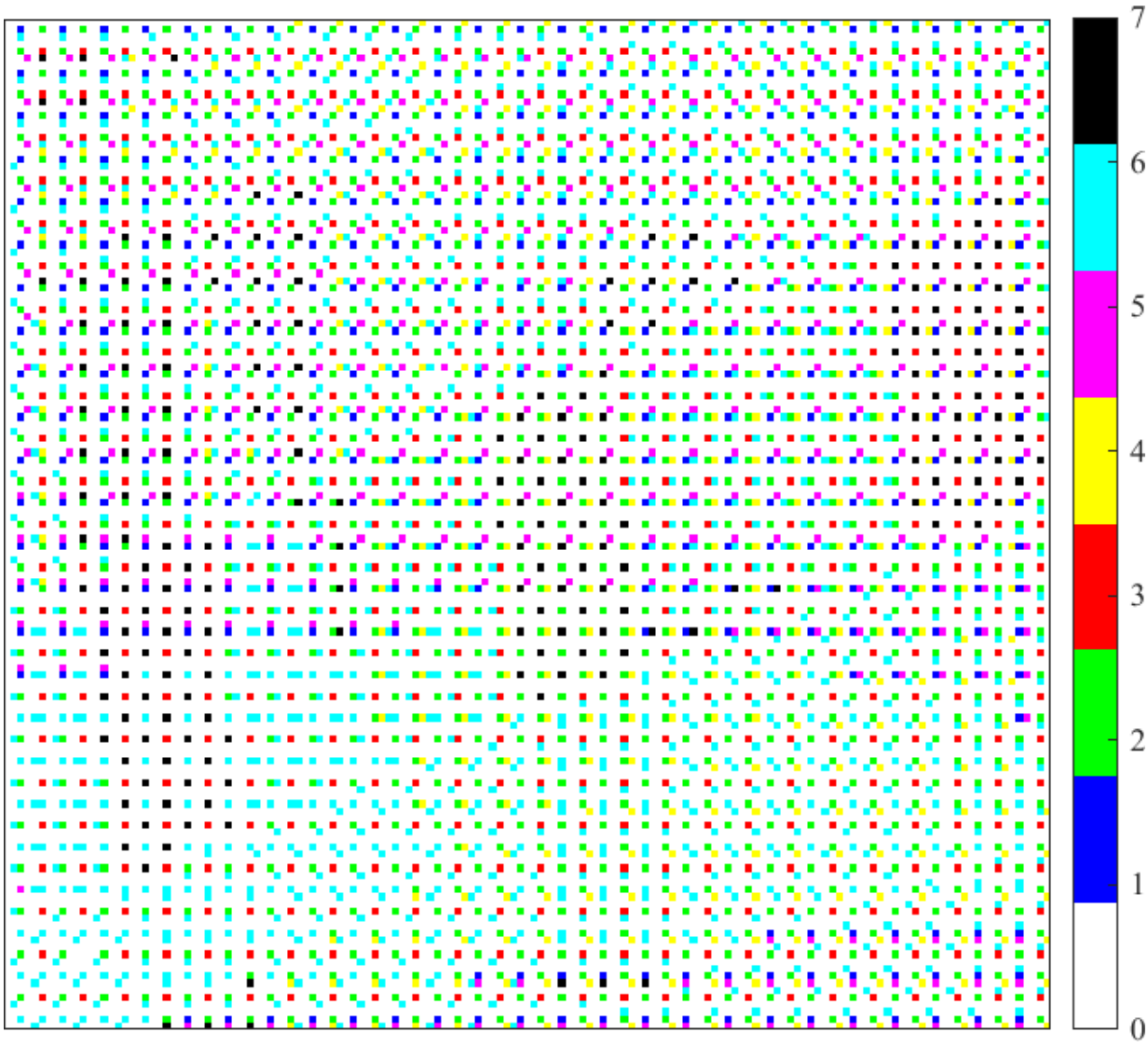

Figure 4.7: The raw six-channel sparse spectral image resulting from the registration of the raw detector readout leading to multispectral compressive sensing. The color of the pixels denotes the location at which spectral information in a given channel is present (channels 1-6). The black pixels denote locations where spectral information in more than one channel is present and the white pixels denote locations where no measurement is made. The region shown in this figure is the same as the region shown in Figure 4.6

.

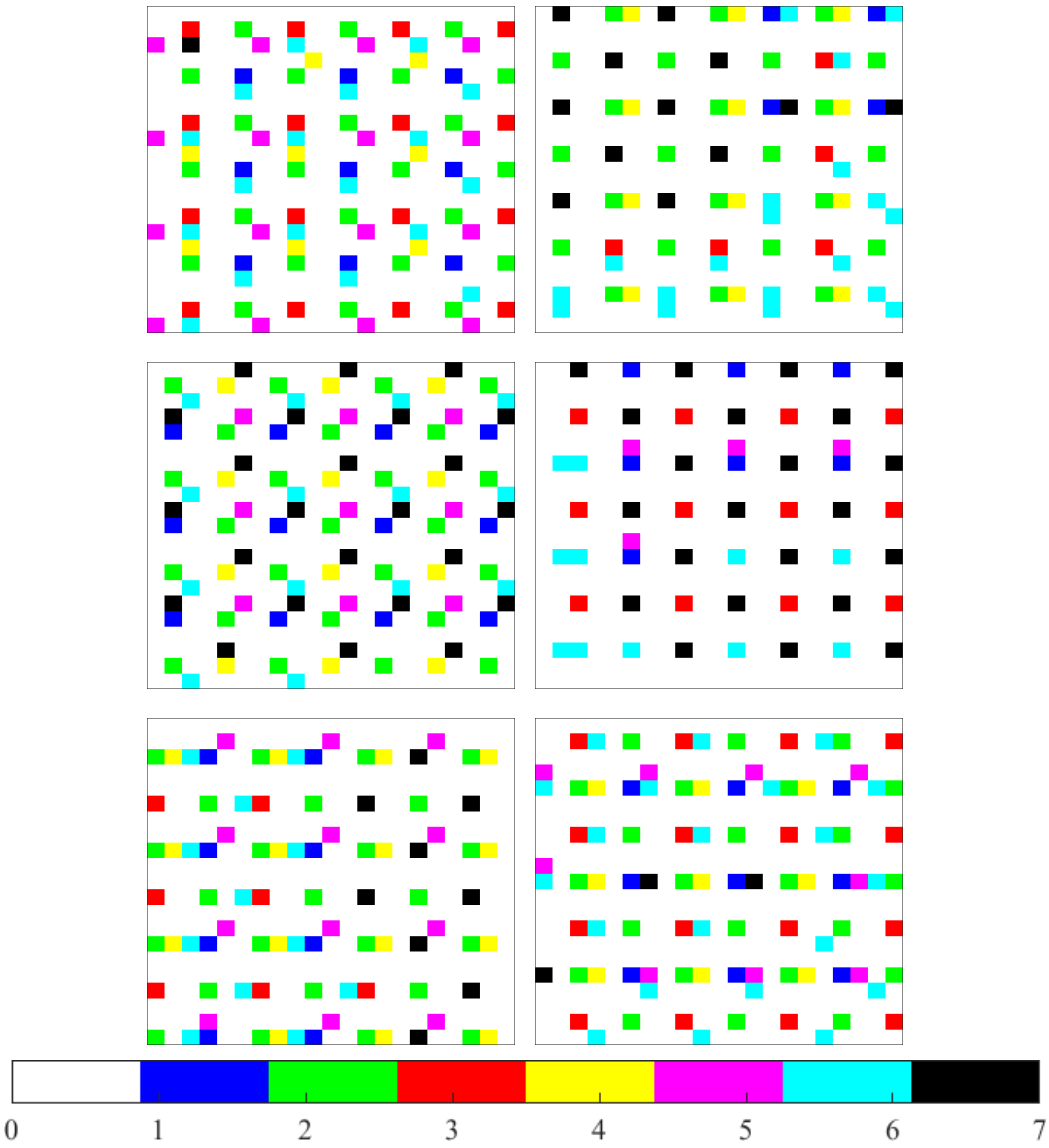

Figure 4.8: A closer look at the compressively sensed data at six different and random locations. The color bar shows the corresponding channels being measured at different spatial locations. The black pixels denote locations where spectral information in more than one channel is present and the white pixels denote locations where no measurement is made.

Figure 4.7 shows the same region of interest from the checkerboard pattern image, highlighting the pixel-based spectral measurements. The color bar in the figure denotes which spectral channel is being measured at which pixel location. The white pixels in this image are location where no measurement is performed which is $\sim 80\%$ of the image. The black pixels in this figure represent pixels where measurement in more than one spectral channel is performed, $\sim 1\%$.

The stochastic distribution of the pixels sampling in the six spectral channels is demonstrated in Figure 4.8. Six different 30×30 pixel regions of Figure 4.6 show the different distribution of the virtual compressive spectral sensing detector. The color code is similar to the one previously mentioned. Of note in this figure is the fact that there appears to be no prominent repeating pattern of the spectral sensing. Additionally, different physical locations of the virtual multispectral sensor are able to observe a selection of the spectral channels instead of all of the channels.

Compressive sensing has enabled a new paradigm in signal and image acquisition of simplified acquisition hardware however these devices will have to be accompanied by advanced, efficient, stable algorithms that would enable fast recovery of the missing information from the dataset to complete the image or signal being interrogated before any analysis can take place.

An advanced interpolation algorithm, proposed by the author, is a multi-layered conditional random field (MCRF) that will allow for interpolation for compressively sensed multispectral data [66]. This approach extends CRFs first proposed in [70], and models each spectral band as a MCRF to use spatial and intensity prior information to enhance and infer high spatial resolution states. The MCRF also incorporates an additional layer of abstraction to enforce the quality of the observations into the optimization.

Additional fiducial information from multiple neighboring spectral bands can be utilized to further enhance the quality of the interpolation A more advanced version of the MCRF, title inter-spectral MCRF (ISMCRF) was proposed by the author that further enhances the quality of the interpolation of the compressively sensed data [76, 75]. In the proposed framework it is presupposed that there exists an underlying connectedness between images in adjacent spectral bands. In other words, images taken in adjacent spectral bands contain spatial characteristics that can be taken into account in the interpolation process such as fundamental relationships between neighboring pixels in an image, intensity differences in

a neighborhood, and similar edge structure. Heeding to these similar spatial properties a more robust and true-to-reality interpolation of the compressively sensed data can be performed.

The two above-mentioned algorithms are of many proposed advanced interpolation algorithms employed in the field of compressive sensing, however, since the premise of this work isn't the exploration, development, and implementation of interpolation algorithm a very simple algorithm will be used to reconstruct the sparse images resulting from imaging using the proposed instrument in this work.

A bilinear interpolation is used to estimate the intensity value of the pixels with non-existent information. For the purposes of the design of the system the bilinear interpolation of the compressive images is deemed to be satisfactory and development and further investigation of any advanced interpolation algorithm is beyond the scope of this work. The bilinear interpolation is an interpolation method using the distance weighted-average of the value of the four nearest neighbors to approximate the value at the location of interest [47, 134, 116] and can be formulated as

$$f(x,y) = \frac{f(B_{11})}{(x_2-x_1)(y_2-y_1)}(x_2-x_1)(y_2-y_1) + \frac{f(B_{21})}{(x_2-x_1)(y_2-y_1)}(x-x_1)(y_2-y) + \frac{f(B_{12})}{(x_2-x_1)(y_2-y_1)}(x_2-x)(y-y_1) + \frac{f(B_{22})}{(x_2-x_1)(y_2-y_1)}(x-x_1)(y-y_1), \quad (4.10)$$

where $\mathbf{B}$ are the four neighbors and the corresponding $(x_\#, y_\#)$ locations.

The compressively sensed spectral images were fully reconstructed and a small region of the larger checkerboard pattern image is shown in Figure 4.9. The images in this figure tend to appear to be binary or with a limited greyscale levels, however this is not the case. The appearance is just the artifact of dynamic range stretching of these images and all posses the full 16 bit dynamic range. This is especially important for the purposes of multispectral data analysis and interpretation.

The quality of interpolation using any algorithm is of great importance and the most widely accepted method of measuring the quality is to evaluate the structural similarity (SSIM), [126], between the reconstructed images and their fully sampled original counterpart, if available.

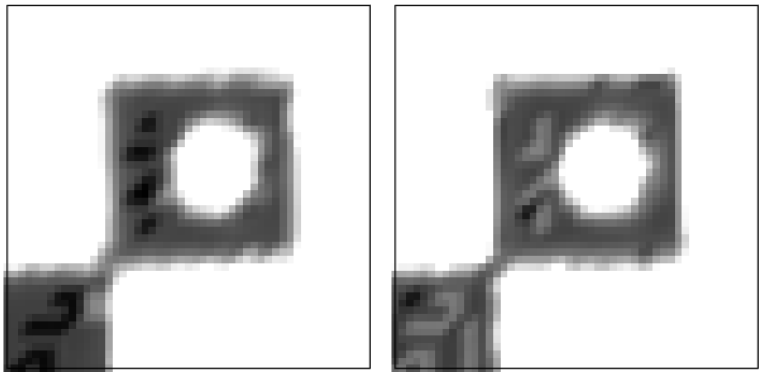

(a) CH1

(b) CH2

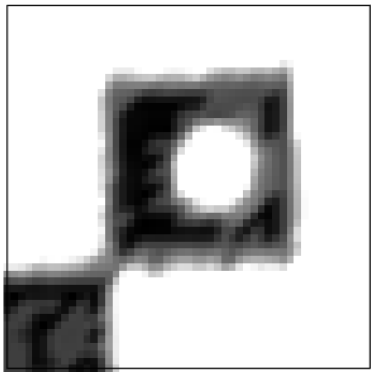

(c) CH3

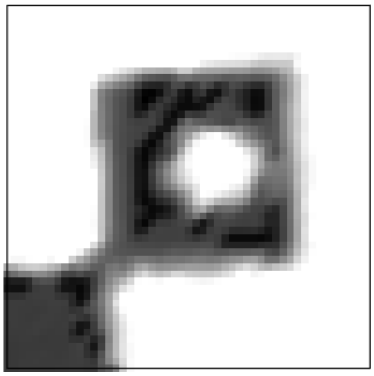

(d) CH4

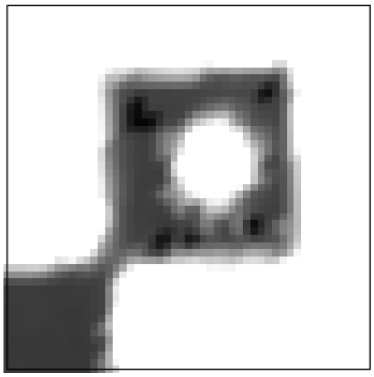

(e) CH5

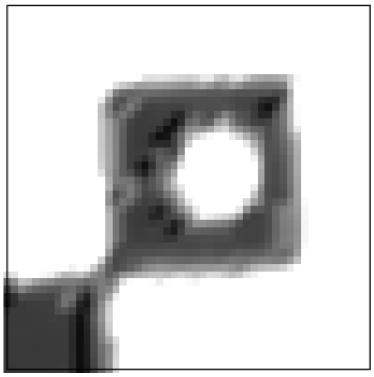

(f) CH6

Figure 4.9: The result of the bilinear interpolation of the compressive data to estimate the missing information in each channel and form a complete image that can be used in multispectral analysis.

The SSIM index is proposed to measure the similarity in a pixel by pixel approach between two images, in a fixed $M \times M$ window, with 0 and 1 being most dissimilar to most similar, respectively [126]. The SSIM index can be computed by

$$SSIM(x, y) = \frac{(2\mu_x\mu_y + c_1)(2\sigma_{xy} + c_2)}{(\mu_x^2 + \mu_y^2 + c_1)(\sigma_x^2 + \sigma_y^2 + c_2)}, \tag{4.11}$$

where μ_x and μ_y are the average of images x and y, respectively, σ_x^2 andσ_y^2 are the variance of images x and y, respectively, and σ_{xy} is the covariance of images x and y. The constants $c_1 = (k_1 L)^2$ and $c_2 = (k_2 L)^2$ where L is the dynamic range of the image and k_1 and k_2 are 0.01 and 0.03, respectively.

The SSIM distribution between the reconstructed images and the original checkerboard pattern that was created using vector graphics and printed for imaging are shown in Figure 4.10 for each channels. The red vertical line represents the mean of the distributions which corresponds to the SSIM_{mean} indexes presented in Table 4.3. The SSIM indexes for the first three channels are the highest compared to the other three channels which are similarly and considerably lower. Uncertainties introduced as a result of registration could be one of the factors in the decline of the SSIM indexes of the second three channels. Furthermore, the images reconstructed in channels four, five, and six are results of the images captured in POVs III, IV, and V respectively. These POVs suffer from notable defocusing which would introduce more divergence in the SSIM_{mean} index from complete similarity.

Table 4.3: The structural similarity value between the reconstructed compressive images and the fully-sampled camera output.

Channel	SSIM_{mean} Index	SSIM_{median} Index
1	0.6783	0.7421
2	0.6732	0.7431
3	0.6783	0.7616
4	0.6468	0.7221
5	0.6159	0.7143
6	0.6312	0.7042

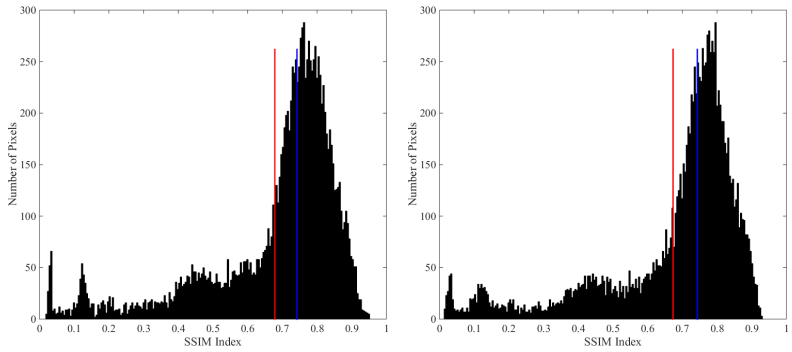

(a) CH1

(b) CH2

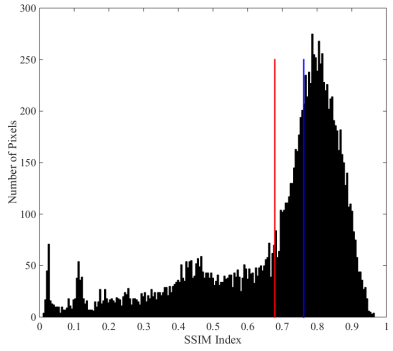

(c) CH3

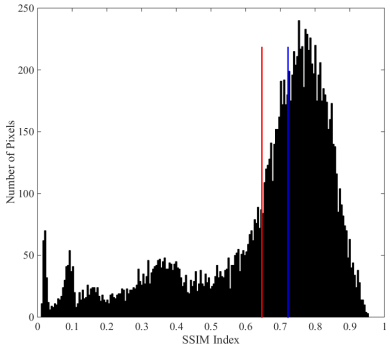

(d) CH4

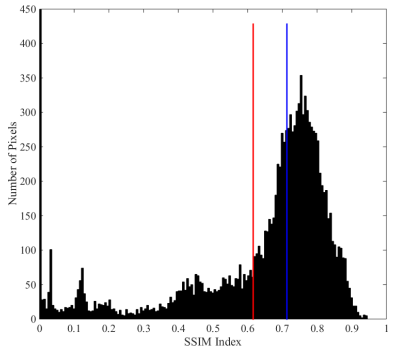

(e) CH5

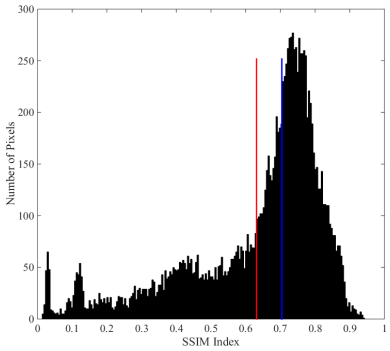

(f) CH6

Figure 4.10: The histogram of the structural similarity distribution of the six spectral channels comparing the reconstructed compressive spectral images and the camera interpolated fully-sampled images. The red vertical line in each subplot represents the mean of the values and the blue vertical lines represents the median of the values which correspond to the SSIM indexes presented in Table 4.3.

A notable fact with regards to Figure 4.10 is that the majority of the power of the distributions is much close to the index 1 which would represent a perfect similarity. In other words, since the SSIM distribution isn't a Gaussian (normal distribution) distribution and tends to be skewed toward the maximum value, finding the mean of this distribution and quoting it as a representative value of the data isn't necessarily a fair process. It is postulated that the median value of the SSIM distribution would be a better representation of the structural similarity. The mean and median SSIM indexes are shown using red and blue vertical lines, respectively, in each of the sub-figures in Figure 4.10. The median SSIM index (blue vertical line) is much closer to the largest peak in the distribution. The respective values for both of the mean and median SSIM indexes represented in Table 4.3. Note that the median SSIM value is systematically higher than the mean SSIM value.

Considering the fact that the interpolation of the sparse images was done using only $<10\%$ of the pixels in the image that contain actual measurements, the results of the interpolation have structural similarity of $\sim 70\%$ with the original sample is very reassuring.

4.3 Numerical Hyper-Focusing

The quality of the images captured using the device will depend on the quality of its' optical elements, more specifically the image forming optical component. Optical aberrations are present as a result of light traversing any optics and therefore are a persistent reality in any optical imaging device. There are many methods of dealing with aberrations that can be considered in an optical design, however, aberrations can not be removed all together. There are eight optical aberrations that could plague an imaging system and are discussed in turn below. Aberration theory describes the aberrations in terms of errors in the wavefront that manifest themselves as positional errors in the focal plane. Even though a wave description is used to describe and define the aberrations, a geometrical ray model is sufficient to trace an aberrated optical system [7, 44, 48, 89].

The piston and tilt aberrations are those that introduce an offset in the phase of the wavefront that has been transmitted by a lens onto a focal plane [83]. A piston aberration would suggest that the entire wave front at the focal plane has a constant phase offset and tilt suggests that there is a sloped phase change across the focal plane in either or both of

the lateral directions.

Chromatic aberration results from the refractive index of the lens being dependent on the wavelength of the light transmitted through it. Hence, the propagation speed is different for different wavelengths which leads to dispersion of light and this dispersion is manifested axially as different wavelengths of light come to focus at different axial distance from the lens and deviate from the actual focal length of the lens.

There are five Siedel aberrations first proposed by Philipp Ludwig von Seidel and are [127]: The **spherical aberration**, which is the result of the fact that rays further out towards the edge of the exit pupil come to a focus closer to the exit pupil, for a positive focal length lens, and opposite for a negative focal length lens. **Distortion** is seen as an image magnification that depends on the position in the focal plane. Distortion is caused by the location of the system stop relative to the position of the lens, meaning that the light is being focused on the focal plane at an incorrect distance from the optical axis. **Field curvature** is due to the focal plane being planar and not curved. Since lenses are curved surfaces then the focusing power of the curved lens will be sufficient to focus the light at a curvature, corresponding to the curvature of the lens itself, at the distance of the focal plane. However, detectors that are placed at the focal plane of lenses are planer and not curved. **Astigmatism** is similar to field curvature with the exception that it is not isotropic along the focal plane and has a directional preference. **Coma** is caused by an image magnification that is dependent upon the exit pupil location and affects light rays off of the optical axis. In other words, any off-axis image may be elongated and demonstrate a comet tail stretched toward the optical axis

Defocus can be caused either by choosing the wrong focal plane, or by axially moving the lens by a distance. The defocus aberration has a strong connection with respect to the lens in the radial direction. Meaning, there is more defocus in the radial direction away from the optical axis in the focal plane. Defocus can also be resulting from any optical path difference that may exist in the imaging device and should be addressed to achieve high quality images, as described in § 4.3.

A 13 element complex lens in the case of the DSLR used here. Such lenses are designed with utmost care to quality therefore the aberrations have been minimized as much as possible and are barely noticeable, if existent at all. Having said that, the nature of the optical design of the FOV replicating device and the spectral filtering device tend to

introduce an optical path difference unique to each one of the POVs, therefore, defocusing aberration is ubiquitous in the system. All imaging system suffer from defocusing to a certain extent which means the lateral resolution decreases radially, being rotationally invariant, from the principal optical axis. The decline in the lateral resolution as a function of radius is not unique to defocusing and it is rather an affect due to all aberrations combined, nevertheless all aberrations other than defocusing will not be considered as their effects have been minimized through the careful design of the complex lens system of the camera being used. The radial decline in lateral resolution is used to characterize a lens or a lens system as is coined modulation transfer function [44, 69, 71].

The simultaneous nature of capturing multispectral images dictates that a single focal length is used for the purposes of imaging. This focal length is chosen based on the information available in POV I based on the praxial rays entering the imaging system which benefit from the paraxial approximation [50]. Naturally, by the virtue of the design of the FOV replicating device, the light in the other four POVs have a longer optical path to travel before entering the imaging system hence their focal plane is not exactly the same as the focal plane of POV I which is supposedly on the detector plane. As such, the images captured in FOVs II-V suffer from defocusing. This shortcoming will have to be addressed if the spectral images are to be combined/fused in order to extract any useful information.

To address the shortcomings of the hardware implementation of the imaging system a numerical hyper-focusing algorithm was designed to address the defocusing issue in the captured images. The quality of focus or rather the amount of defocus is evaluated using a local variance of the gradient magnitude measure, Tenengrad metric, of the images captured [21, 97, 136]. A Bayesian-based maximum a posteriori probabilistic approach is then implemented and used to improve the resolution of the images in all POVs.

4.3.1 Mathematical Formulation

Tenengrad Focus Metric

The implementation of the Tenengrad focus measurement metric [136], is a local variance of the gradient magnitude measure using a modified horizontal and vertical pseudo-Sobel edge detection mask. The gradient magnitude Tenengrad focus measure of an image can

be computed by

$$FM_{Tenen} = \sum_{i=1}^{n-1} \sum_{j=1}^{m-1} \mathbf{E}[(\nabla I(i,j))^2] - (\mathbf{E}[\nabla I(i,j)])^2, \tag{4.12}$$

where N and M are the dimensions of the image referenced by i and j and $E[.]$ is the expected value of the gradient magnitude of the image. The expected value can be represented as

$$\mathbf{E}[(\nabla I(i,j))^2] = \left(\frac{1}{nm} \sum_{i=1}^{n-1} \sum_{j=1}^{m-1} (\nabla I(i,j))^2 \right), \tag{4.13}$$

and

$$(\mathbf{E}[\nabla I(i,j)])^2 = \left(\frac{1}{nm} \sum_{i=1}^{n-1} \sum_{j=1}^{m-1} (\nabla I(i,j)) \right)^2, \tag{4.14}$$

where $n = m = 3$ which represents a local moving average. Finally, the magnitude of the directional gradient of the image is calculated based on

$$\nabla I(i,j) = \sqrt{\nabla I_i(i,j)^2 + \nabla I_j(i,j)^2}, \tag{4.15}$$

where $\nabla I_{i,j} i(i,j)$ is the directional gradient measurement in the i^{th} or the j^{th} direction.

The directional gradient is implemented as a filtering kernel which is then convolved with the image that is being interrogated. The implementation of these kernels takes place in the horizontal and the vertical directions separately. The two are then combined using Equation 4.15 to create an edge strength map of the image. The kernel can be described as a convolution of an elementary edge detection matrix such as

$$\begin{bmatrix} \dots & -1 & 0 & 1 & \dots \\ \vdots & \vdots & \vdots & \vdots & \vdots \\ \dots & -1 & 0 & 1 & \dots \end{bmatrix}, \tag{4.16}$$

in the horizontal direction or its transpose in the vertical direction. The size of the edge detection kernel can be defined as desired, hence the '...' in Equation 4.16. The edge detection operator is then convolved with a zero-mean Gaussian distribution kernel to create the directional gradient kernel. The visual representation of the horizontal and the vertical gradient kernels are shown in Figure 4.11. The Tenengrad focus metric proposed here will be used to measure the quality of the focus as the result of the hyper-focusing algorithm to be discussed in the following section.

Numerical Focusing

The proposed method, for performing numerical focusing is an iterative Bayesian-based approach based on the work presented by the author [129] which is in turn based on the Bayesian-based model developed in [130]. This approach aims to create a model of the desired hyper-focused POV image ($\mathfrak{f}$) from the true captured image itself (g), both modeled as a probability distributions. In the proposed Bayesian-based method, the goal is to determine the most probable desired, focused image $\hat{f}$, given the measured defocused image g, based on prior knowledge related to $\mathfrak{f}$, knowledge of the transfer function associated with optical aberrations (H_a). This can be formulated as the following maximum a posteriori problem

$$\hat{f} = \text{argmax}_{\mathfrak{f}} \; P\left(\mathfrak{f}|g\right), \tag{4.17}$$

where $P\left(\mathfrak{f}|g\right)$ is the conditional probability of $\mathfrak{f}$ given g. This becomes an optimization of a probabilistic argument by solving which the hyper-focused image of each of the POVs should be the result. An alternate and equivalent formulation would be

$$\hat{f} = \text{argmax}_{\mathfrak{f}} \; P\left(g|\mathfrak{f}\right) P(\mathfrak{f}), \tag{4.18}$$

where $P(g|\mathfrak{f})$ is the likelihood and $P(\mathfrak{f})$ is the prior. The prior in this case is the point spread function (PSF) of the imaging device. Therefore, given the PSF and using this probabilistic approach the defocused images can be numerically focused and will allow for extraction of smaller lateral details in the image. Consider $\mathfrak{S}$ to be a set of pixel locations in the imaging system's detector array and $s \in \mathfrak{S}$ to be a specific pixel location on the same detector array. In the case of the proposed multispectral imaging system, the noise is primarily related to quantum photon emission. As such, accounting for the statistics of this noise in the proposed method along with any aberrations (characterized by H_a), the likelihood $P(g|\mathfrak{f})$ takes the form

$$P\left(g|\mathfrak{f}\right) = \prod_{s \in \mathfrak{S}} \frac{\left(\mathfrak{F}^{-1}\left\{H_a \mathfrak{F}\left\{f_s\right\}\right\}\right)^{g_s} e^{-\left(\mathfrak{F}^{-1}\left\{H_a \mathfrak{F}\left\{f_s\right\}\right\}\right)}}{g_s!}, \tag{4.19}$$

where $\mathfrak{F}$ and $\mathfrak{F}^{-1}$ denote the forward and inverse Fourier transform, respectively. In order to adequately perform the optimization process and produce a result that would in fact be representative of an image with least amount of defocus, the PSF of the imaging device is

either empirically measured or postulated and is enforced as a prior model

$$P\left(\mathfrak{f}\right) = \prod_{s \in \mathfrak{S}} e^{-\frac{(f_s - \mathbf{E}(f_s))^2}{2\xi^2}}, \tag{4.20}$$

where the parameter f_s as a nonstationary process with a nonstationary expectation $\mathbf{E}(f_s)$ and a variance ξ^2. This prior model is simply a Gaussian distribution which most closely resembles the 'half-rectified sinc' or Airy pattern which is the true PSF of an optical refractive or reflective imaging forming process. The process of enhancing the focus of the image is an iterative process, and each iteration uses the information from the previous iteration and given some prior knowledge about the image can improve the image quality.

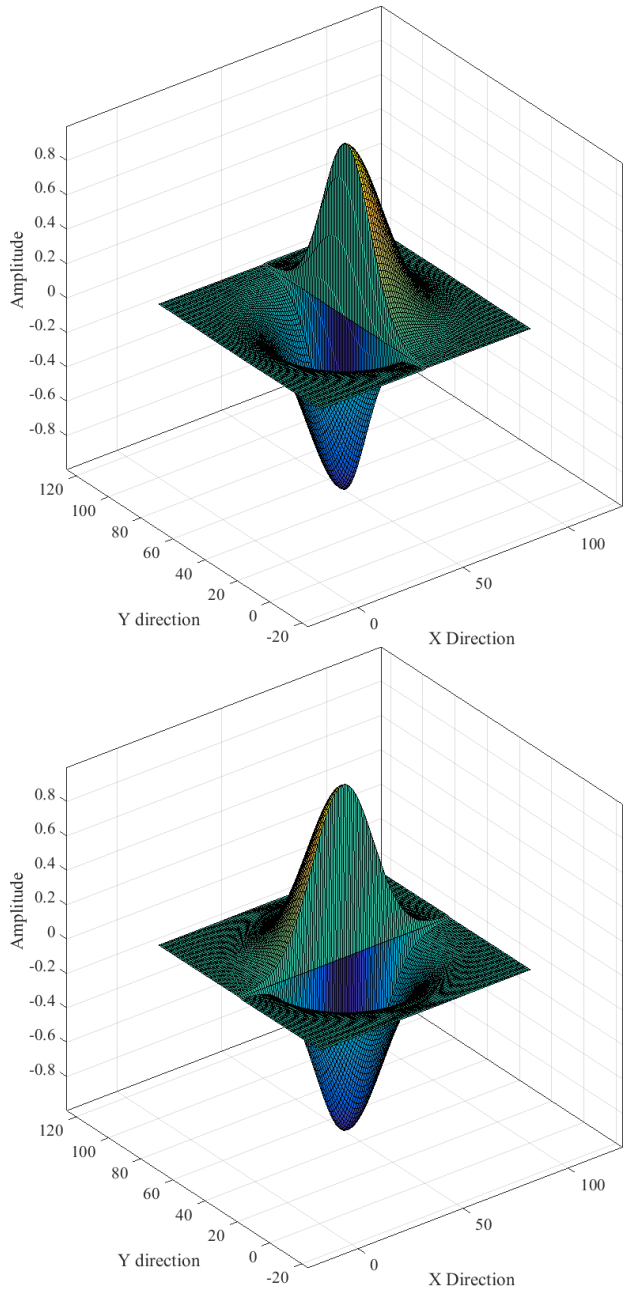

Figure 4.11: The two directional gradient kernels, horizontal and vertical, that are convolved with the image to detect horizontal and vertical edges.

4.3.2 Measured Defocus in the Hardware Implementation

An experiment was carried out to characterize the focusing properties of the hardware implementation for each of the POVs as well as the autofocus of the imaging device. More specifically, a target was repetitively imaged by the system as it was displaced towards and away from the system. The target used was the 1951 USAF resolution target, shown in Figure 4.12, and it was placed on a linear stage for displacement and it was displaced at intervals of 635 μm. The target consists of groups comprising six elements each having a three-bar horizontal and vertical structure. The groups and elements decrease in size systematically, and the smallest triplet that can be discerned by an imaging system is considered to be the resolving power of the system.

The USAF target was placed at a distance of $\sim$ 75 mm away from the dSI assembly such that a clear image of the target, in its entirety, was observed in all POV concurrently. This distance is defined as ideal distance for the placement of the target from the imaging system and denoted as linear location 'zero'. Any departure from this location toward or away from the imaging system will be denoted by a negative or a positive translation, respectively. Note that the spectral field filters in the spectral filtering device were removed therefore all POVs were observing the target in visible range.

The extent of displacement of the target was $\sim$ 25 mm in both positive and negative directions. This limitation was placed to ensure that the target could still be observed in each one of the POVs of the imaging system.

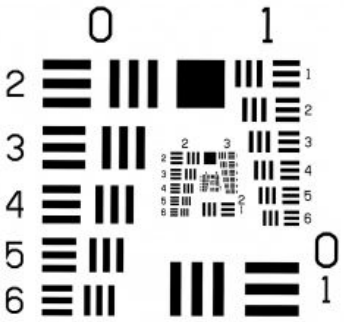

Figure 4.12: The 1951 USAF Resolution Target.

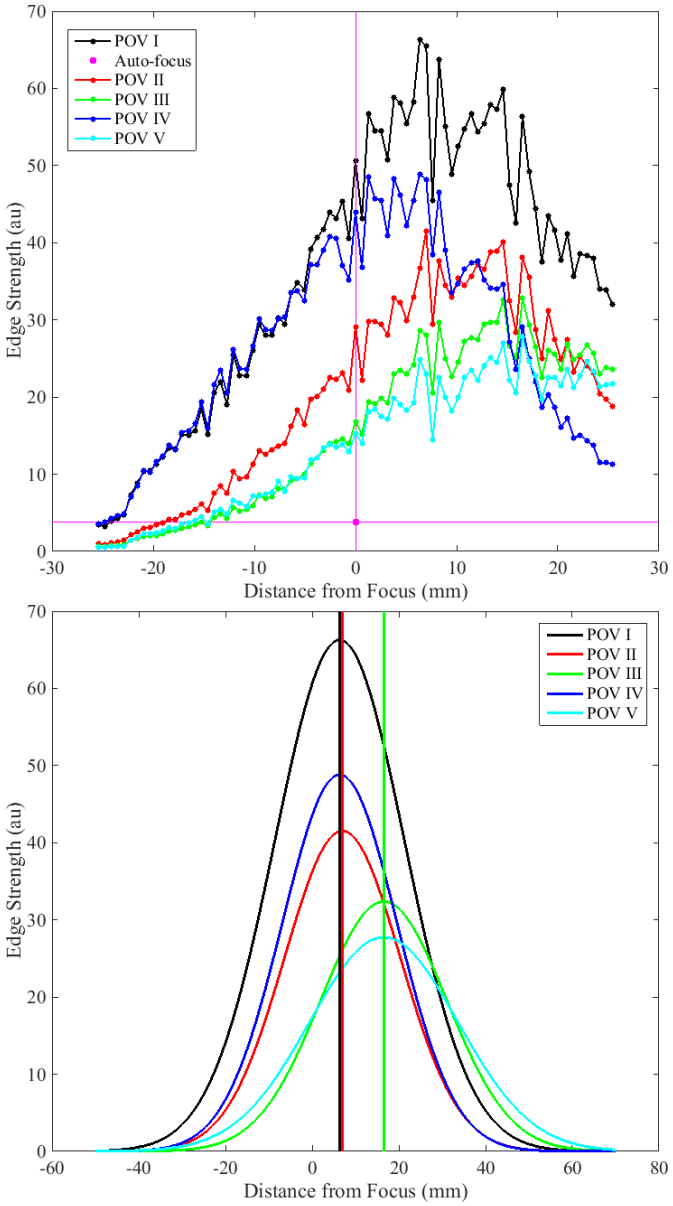

Figure 4.13: Local variance of the Tenengrad focusing metric evaluated for the five POVs. POV I (black), POV II (red), POV III (green), POV IV (blue), and POV V (cyan). The top plot shows the measured data points as well as the magenta point signifying the evaluated Tenengrad focus metric of the 'autofocused' image of POV I. The bottom plot is the Gaussian fits to the points of the top plot with the locations of the peak of the POVs noted by the vertical lines. Note that POVs I and IV and POV III and V have common peaks.

The Tenengrad focus metric was applied to the image of each of the POVs in all of the images captured after every translation. The change in the focusing capabilities of the imaging device is shown in Figure 4.13 by way of the Tenengrad focus measure.

The focus measure for POV I is shown in black, POV II is shown in red, POV III is shown in green, POV IV is shown in blue, and POV V is shown in cyan. The top plot in Figure 4.13 shows the raw evaluated edge strength in each of the images and the bottom plot shows the Gaussian fit to the data which is a good representative of the behavior of the edge strength or the focus measure. In Figure 4.13 top, the magenta point signifies the edge strength of the image of POV I captured using the imaging device's Auto-Focus capability. The low value of the edge strength in the Auto-Focus image is the result of the fact that this feature of the imaging device is 1) not calibrated; 2) is misguided as a result of removal of the internal NIR blocking filter affecting the optical path difference in the Auto-Focus optics compared to the actual imaging optics; 3) is misguided as a result of removal of the internal NIR blocking filter creating chromatic aberration affecting the Auto-Focus optics and decision making.

The edge strength measured by the Tenengrad metric in the image of POV I of the Auto-Focus image is similar to the edge strength measured in the image, of POV I, that is located at -30 mm from the image that has the highest edge strength. This means that with the current setup the Auto-Focus capabilities of the imaging device can not be trusted. Accordingly, the focus of the imaging device was adjusted, and confirmed by inspection, to capture an image at location 'zero' that appears to be in focus. As observed in Figure 4.13 top, the manually adjusted focus was not the optimal focal point of the imaging device which was in fact $\sim$ 6 mm farther away from the one selected manually. Note that this process was intended to be done using the image in POV I since it is the POV on the optical axis of the instrument and is not affected by the FOV replicating device, hence no additional optical path differences are introduced.

A Gaussian function was fitted to the edge strength data which appears to be a good approximation to it, Figure 4.13 bottom, in a sense that the edge strength would drop as a function of departure from the focal plane of the optics. The location of the peak in the edge strength of each POV is marked in the same figure using vertical lines. The peaks POVs I and IV and POVs III and V are common and are therefore shown with the same line, black for POVs I and IV and green for POV III and V. The discrepancy between the

focusing capabilities in POVs II and IV and POVs III and V is merely due to the fact that they are located at different distances from the optical axis of the imaging device and therefore there is a difference in the distance by which the light beam, off of the object, will have to travel to enter the imaging device. Furthermore, the radial location at which the light beams from these two POVs enter the imaging device will impose the effects of the modulation transfer function of the optics which would further deteriorate the quality of the focus.

Theoretically, the edge strength observed in POVs III and V and II and IV have to be the same assuming no errors in the manufacturing process of the dSI. In this case the locations of the peaks of POVs III and V correspond but the locations of peaks of POVs II and IV don't as they differ by $\sim 600\ \mu m$ however this off-set is less than the length of one translation step in the experimental setup therefore if can be attributed to sampling error. If the off-set in the peak locations of POVs II and IV is in fact real, it may be caused by the tolerance or rather uncertainty of the 3D printer and the printing process.

This discrepancy in the focusing capability of the hardware implementation in each of the POVs is not desirable and will therefore have to be addressed computationally to increase the resolution of the image in each POV. The practical implementation of the numerical focusing of the system is discussed in the following subsection.

4.3.3 Hyper-focusing of the Images

The iterative numerical hyper-focusing was implemented in MATLAB as per the formulation presented in this section. For demonstration purposes the images captured using the system at location zero, according to the previous subsection, was chosen for hyper-focusing. The goal of performing the hyper-focusing is to improve the image quality such that the information that is captured in an image will be much sharper than the original. The ultimate goal of hyper-focusing would be to transform any out-of-focus image into an image which is at the focusing limit of the imaging device. The purpose of hyper-focusing is not to increase the resolving power of the instrument as it is not a possibility since the resolving power is dependent on many other physical limitations other than defocusing aberration such as the resolution capability imposed by the imaging lens, signal-to-noise-ratio, severity of aberrations in the image, and the presence of any imaging artifacts.

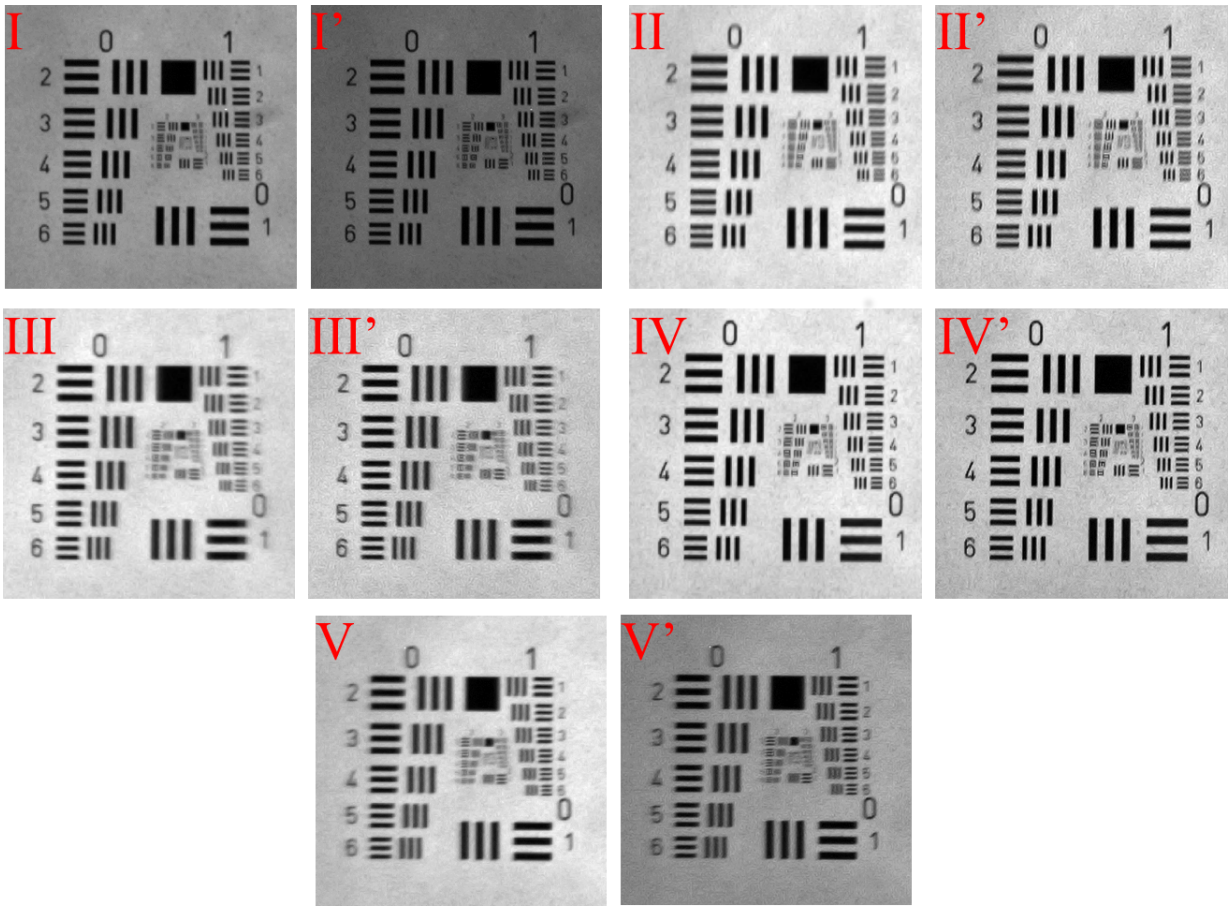

Figure 4.14: The hyper-focused images of all five POVs. The POV number is denoted on each image the ' marking denoted the refocused image of the corresponding POV.

The most suitable point-spread-function to use in the numerical focusing algorithm was selected using a grid search approach in which the standard deviation or the full-width-half-maximum of the Gaussian kernel was iteratively selected in order to maximize the Tenengrad focus metric

$$PSF(H, \Sigma) = \text{argmax } P(FM_{Tenen}|H, \sigma), \tag{4.21}$$

where H and Σ are the kernel size and the standard deviation of the ideal PSF, respectively, given σ which is the standard deviation of the test PSF.

The edge strength measured in each of the focused images resulting from the optimization process are summarized in Table 4.4. The properties of the PSF for each of the POVs is different, although within a reasonable neighborhood of one another. This verifies that each of the POV images has different optical properties than the others and a global numerical focusing or the internal focusing of the camera itself will not be able to improve the image quality of every POV equally.

The results of hyper-focusing of the five POVs are shown in Figure 4.14. In this figure the captured images of the POVs are marked with the POV number for original and the POV number followed by the prime (') for the hyper-refocused images. It is clear that the detail in the refocused images are much sharper than the original. Again, the purpose of refocusing wasn't to increase the resolving power of the imaging system but rather to improve the quality of the captured images. Here, improving the resolving power means to clearly observe a smaller triplet of horizontal or vertical lines in groups‘ 2 or 3 of the USAF resolution target.

Table 4.4: The properties of the PSF of different POV, in pixels, used for hyper-focusing and the corresponding Tenengrad metric measure.

POV	Edge Strength
I	101
II	139
III	74
IV	294
V	89

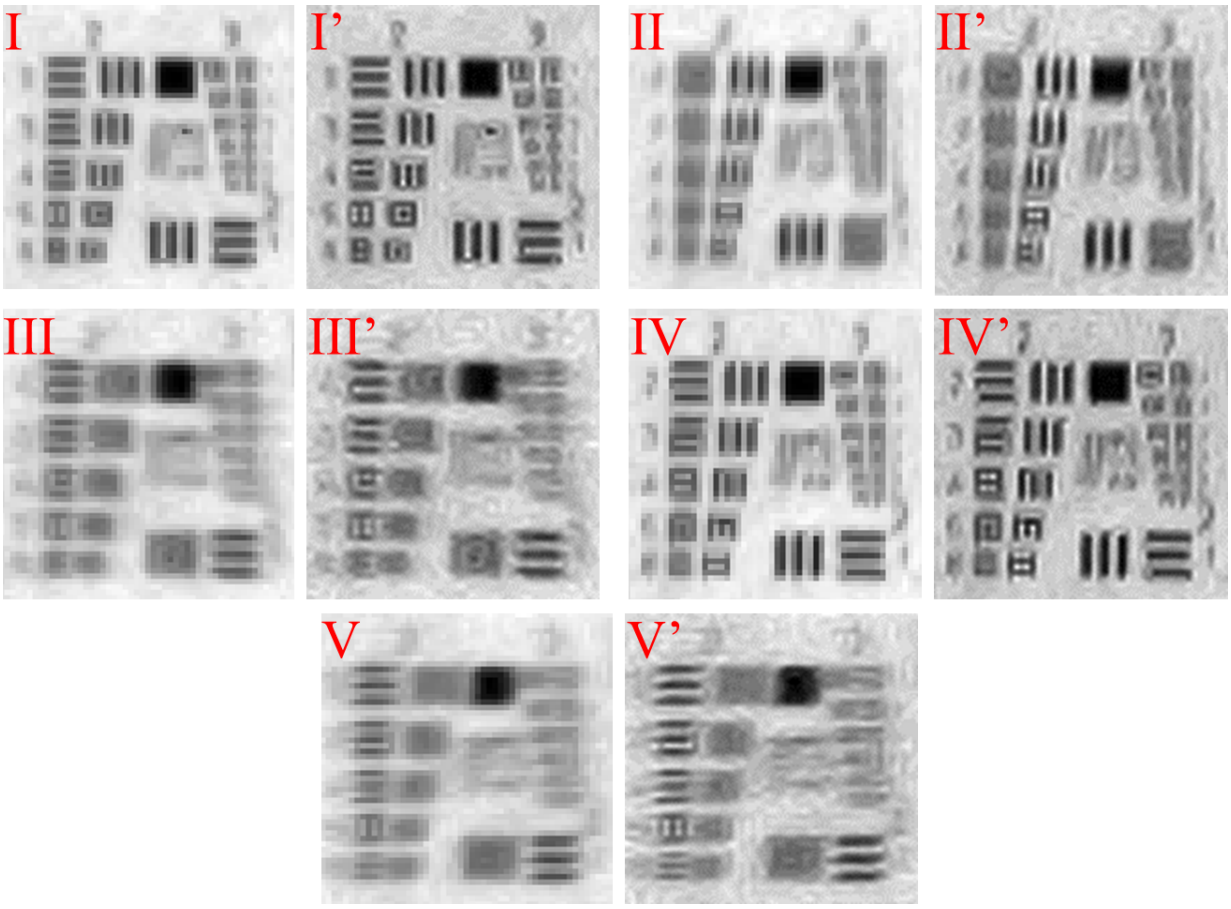

Figure 4.15: The zoomed-in section of the hyper-focused images of all five POVs. The POV number is denoted on each image the ' marking denoted the refocused image of the corresponding POV.

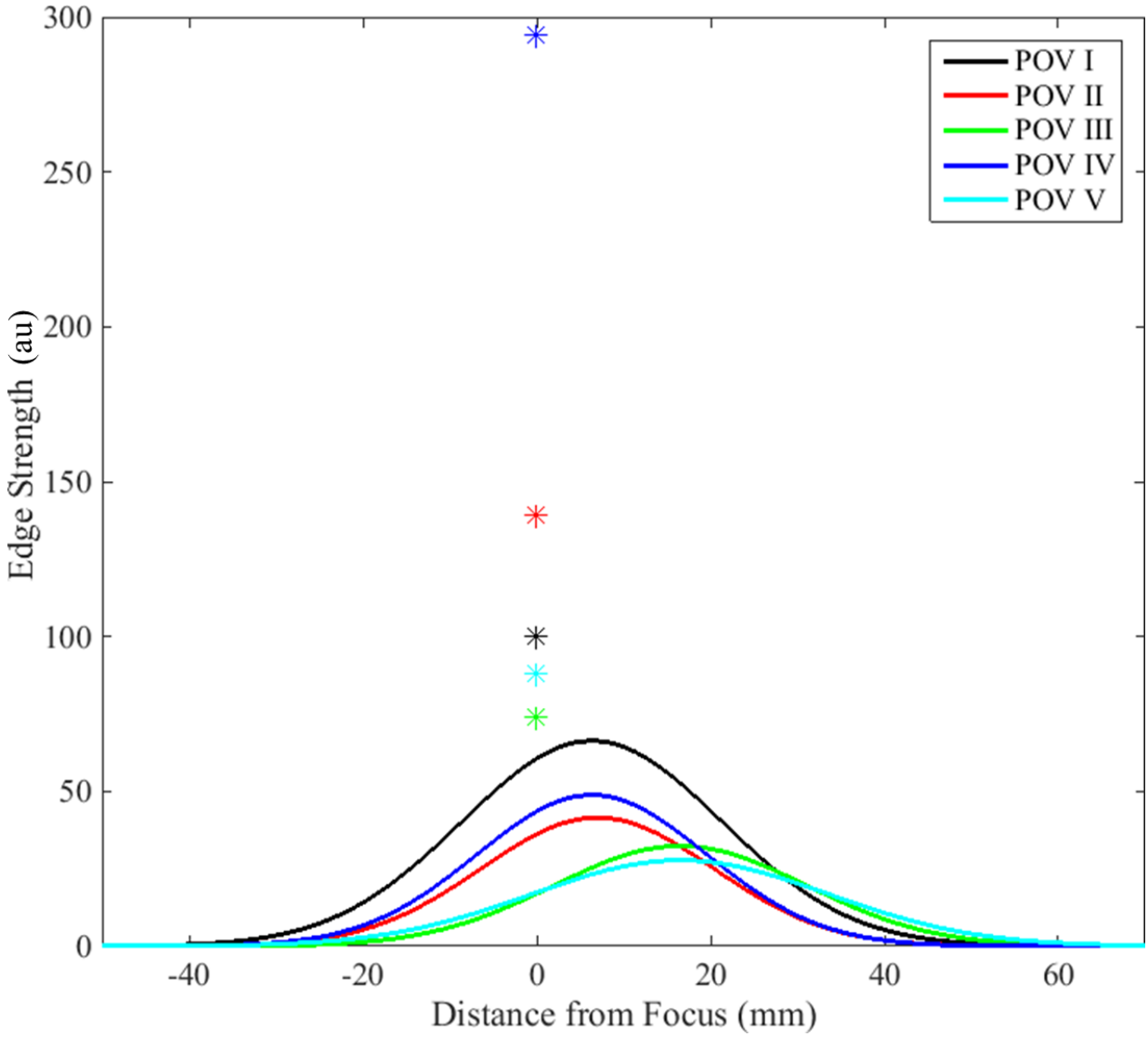

Figure 4.16: The edge strength of the hyper-focused images, using the Tenengrad focus measure, of the five POVs, solid lines, and the calculated Tenengrad focus measure of the image at 'zero' location after hyper-focusing, stars. POV I (black), POV II (red), POV III (green), POV IV (blue), and POV V (cyan).

Assessing the focus improvement of the refocused images was done using the Tenengrad focus metric. The images that were used for the hyper-focusing process were the one captured at the focal plane of the camera. After hyper-focusing was performed the edge strength of each POV image was evaluated and was over-plotted on the plot of the calculated focus metric at different locations with respect to the focal plane of the imaging system, see Figure 4.16. According to this plot the edge strength of the structures in the images have increased by more than four times in the best case (POV IV) and about two times in the worst case (POVs III and V). Furthermore, the sharpness of the hyper-focused images surpasses the maximum sharpness of the images that could be achieved by the hardware implementation.

Quantification of the Hyper-focusing Capabilities

Further analysis was carried out to determine the quantitative improvement of image quality after performing the hyper-focusing. The criteria based on which the image quality can be determined are chosen to be: 1) the improvement or maintaining in resolution determined by examining the visibility of the elements in the USAF resolution target; 2) the signal-to-noise ratio of the images; 3) the contrast-to-noise ratio (CNR) of the images; 4) the improvement in sharpness of details.

A comparative study between the original images and the hyper-focused images with regards to the SNR And CNR can not be carried out as these two metrics will be higher (better) for the original image. The reason being that in out-of-focus images the variance in noise is reduced because of blurring effects and it will increase as the image sharpness is

Table 4.5: Quantitative measure of the hyper-focused image attributes.

POV	Element/Resolution Before	Element/Resolution After	SNR (dB)	CNR
I	2-3/99 μm	2-6/70 μm	41.00	112.41
II	2-6/70 μm	2-6/70 μm	46.12	202.33
III	2-4/88 μm	3-1/63 μm	46.91	221.49
IV	2-5/79 μm	2-5/79 μm	42.01	125.99
V	2-4/88 μm	2-6/70 μm	47.22	229.71

increased. Therefore, the variance in the noise in the hyper-focused images is larger than its counterpart in the original defocused image, and regardless of the amount of improvement in 'signal' these two metrics will decrease for the hyper-focused image.

The above-mentioned metrics of quality have been measured for the hyper-focused image of each POV and the results are presented in Table 4.5. The smallest discernible feature on the USAF resolution target for the original and the hyper-focused image are quoted. Even though no resolution gain was expected from performing hyper-focusing, surprisingly some improvement in resolution was observed. In three out of five POVs (I, II, and V) significant gain in resolution was observed as smaller elements in the USAF target were observable after performing the hyper-focusing as seen in Figure 4.15. The remaining two POVs (II and IV) showed no improvement in resolution however according to Figure 4.17 the local contrast in the data was increased at the peaks and valleys of the target elements are evidently much more pronounced. Pertaining to the overall system resolution, considering the worst case scenario, a resolution of 79 μm surpasses the requirement of 200 μm resolution by more than twice. The SNR and CNR for the hyper-focused images are considerably high, therefore it can be concluded that the hyper-focusing process did not degrade the quality of the image.

Table 4.6: Improvement in image sharpness resulting from hyper-focusing.

POV	Resolution Increase (%)
I	29
II	0
III	28
IV	0
V	20

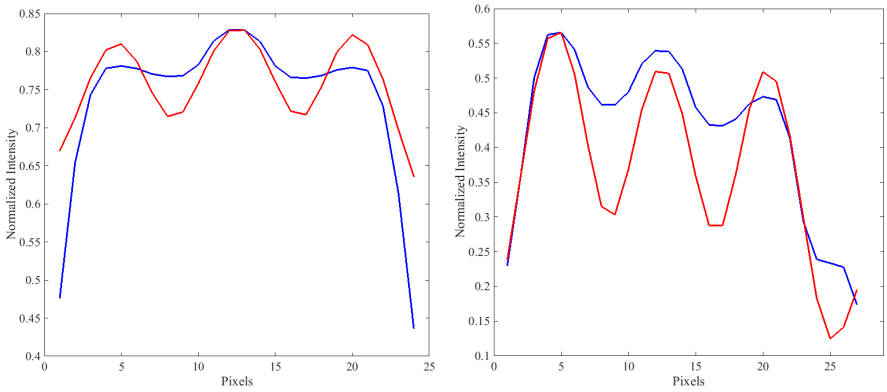

(a) POV I, 2-6

(b) POV II, 2-6

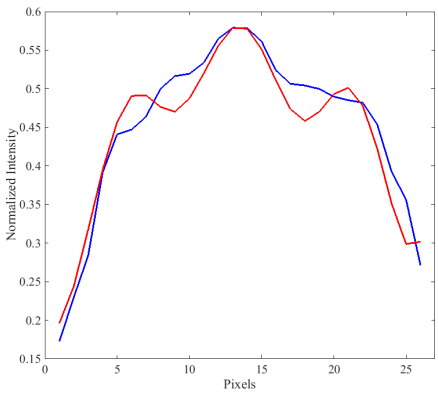

(c) POV III, 3-1

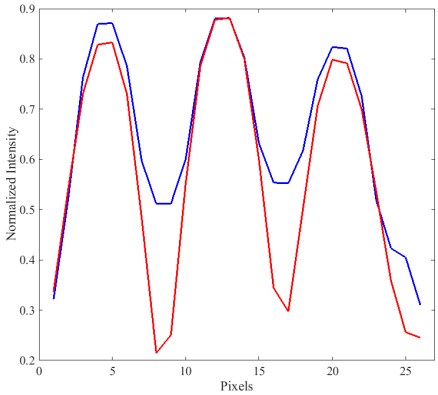

(d) POV IV, 2-5

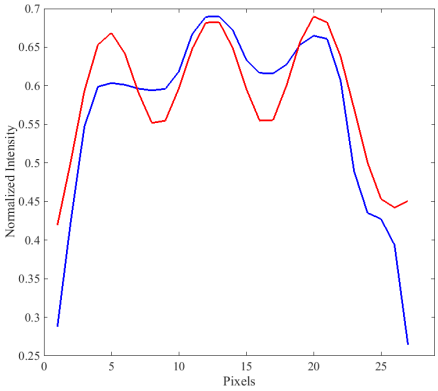

(e) POV V, 2-6

Figure 4.17: The plot of cross section of the intensity profile across the smallest discernible element in the USAF resolution target for each POV before (blue) and after (red) hyper-focusing.

Examining Figure 4.17, it is apparent that the USAF elements that are observed in POVs I, II, and V are not at all observable before performing the hyper-focusing. The resolution increase, in the three POVs that have experienced it, are clearly observed in Figure 4.15 and are quantified and summarized in Table 4.6. With the exception of POVs II and IV the imaging resolution of the system was increased by more that 20% which is representative of the hypothesis that defocus is the main aberration in the system and can be addressed computationally in post-processing therefore decreasing the complexity of the imaging hardware.

Considering the fact that this system will be performing imaging from $\sim$ 400 nm to 1100 nm in different POVs, it is a fair hypothesis that the expected resolution capability would decrease as the wavelength increase. Even though this may be the case, as mentioned previously the optical design of consumer DSLR cameras is of highest quality, therefore the focus at longer wavelengths will not drift much from the nominal in the visible wavelengths. Albeit, the laws of physics will still hold and there will be deviation from the nominal resolution of $\sim$ 80 μm in the NIR channels.

4.4 Data Fusion - Component Analysis

Visualization and interpretation of correlated multivariable, multidimensional datasets are always a challenge. Principal component analysis (PCA) has been proposed to transform the correlated multidimensional data into a set of linearly uncorrelated data using a set of principal components, usually on the order of two or three [41]. The principal components are evaluated and ordered in decreasing magnitude of variance, accounting for the maximum variability in the dataset [59, 61].

Given a multidimensional dataset

$$\mathbf{X} = \begin{bmatrix} \mathbf{x}_1 \\ \vdots \\ \mathbf{x}_j \end{bmatrix}, \tag{4.22}$$

where $\mathbf{x}_n$ are the data vectors, the covariance matrix

$$\mathbf{S} = \begin{bmatrix} s_{11}^2 & s_{12} & \dots & s_{1j}^2 \\ s_{12}^2 & s_{22}^2 & \dots & s_{2j}^2 \\ \vdots & \vdots & \vdots & \vdots \\ s_{1j}^2 & s_{2j}^2 & \dots & s_{jj}^2 \end{bmatrix} \tag{4.23}$$

can be calculated by

$$s_{ij} = \frac{n \ \sum_{k=1}^{n-1} \ x_{ik}x_{jk} - \sum_{k=1}^{n-1} \ x_{ik}x_{jk}}{n(n-1)}, \tag{4.24}$$

with n representing the total number of samples or the length of the $\mathbf{x}$ vectors and x_{ij} is the j^{th} element of the i^{th} data vector $\mathbf{x}$.

Next, the eigenvalues of the covariance matrix are to be calculated by

$$|\mathbf{S} - \Lambda \ \mathbf{I}| = 0, \tag{4.25}$$

where $\mathbf{I}$ is the identity matrix and Λ is the eigenvalue. This equation would then produce j^{th} degree polynomial, j being the length of the multidimensional dataset $\mathbf{X}$, solving which will give then eigenvalues which can then be used to produce the eigenvectors for the data. Using the matrix of the eigenvector, $\mathbf{X}$ can be transformed to a projection principal component space. In most cases only the first two or three principal components are used for visualizing the data. The order of the principal components are determined comparing the eigenvalues with the largest value being the first principal component.

The principal component analysis was performed on the six channel image of a collection of black ink markings from five different pen manufacturers. The resulting first two coefficients are plotted in Figure 5.10. Using the six-channel multispectral image that is captured simultaneously and following the computational imaging described in this chapter, the data available can be fused and analyzed and useful information can be extracted.

The PCA information presented here is to simply demonstrate the power of multispectral imaging, however limited in number of spectral bands. Using intelligent techniques to extract information from multidimensional data, objects that appear to be seemingly the same, five black inks observed in the visible bands can be distinctly differentiated by simply observing them in the NIR. When multispectral image acquisition is performed the information conveyed by the PCA operation will be much more informative.

Chapter 5

Performance and Applications

The performance capabilities of the instrument are put to test via three different experiments. First, the simultaneous multispectral imaging capability of the instrument is evaluated using a sample of fluorescent microspheres. Second, a sample of a collection of inks has been imaged and computationally classified spectrally. Lastly, multispectral information is used to differentiate between a selection of edible oils and to computationally detect adulteration of the oils using simultaneous multispectral fluorescent data.

5.1 Fluorescent Microspheres

The most important outcome of simultaneous multispectral imaging is to compile the images and produce a multispectral image cube. The image cube would consist of images at specific spectral wavelength which have corresponding spatial characteristics therefore enabling spectral investigation at a specific location. This capability is demonstrated for the proposed system in this section.

A selection of 0.5 μm fluorescent microspheres were acquired having a wide range in excitation and emission wavelengths from the UV to the NIR [101]. Resolving and observing a 500 nm object is beyond the imaging resolving power capabilities of the proposed instrument by three orders of magnitude, therefore, the fluorescent microspheres were used to coat larger Polystyrene (plastic) beads. Two different size of plastic beads were chosen,

500 μm and 800 μm, and were immersed in a diluted solution of the 500 nm fluorescent microspheres. The fluorescent microspheres behave as colloidal particles and entirely coat the plastic beads via a process referred to as particle deposition. The coating process follows closely the process presented by Jin *et al.* [60].

The fluorescent microspheres used are designed with specific dyes to have emission maxima at 486 ± 35 nm, 546 ± 40 nm, 662 ± 25 nm, and 820 ± 30 nm [101]. The spheres with the emission spectrum 662 ± 25 nm and 820 ± 30 nm will be observed in two of the channels of the proposed instrument that have overlapping spectral sensitivity with the aforementioned emission spectra. It is therefore expected to observe the plastic beads coated with these dyes in channels 3 and 4 and channels 4 and 5, respectively.

A composite sample was created that comprise of a mixture of the two sizes of the beads that have been coated with the four dyes. The mixture of the plastic beads was fixed using epoxy, ensuring that the epoxy did not fluoresce in the spectral regions of interest. The diameter of the sample was limited to $\sim$ 20 mm which is within the design specifications of the FOV of the instrument. The sample was then irradiated with an 8 W UV lamp at 365 nm. The UV source used is capable of exciting all of the fluorescent dyes and inducing emission at the expected wavelengths.

The proposed instrument was used to capture simultaneous multispectral images of the sample of the fluorescent beads. The individual channels are shown in Figure 5.1 and the hyper-focused color composite of the images are shown in two parts, visible and NIR, in Figure 5.2. The spectral channels shown in Figure 5.1 are representative of the beads observed at that wavelength range and can be used to clearly discern between different beads. Additionally, the beads of different sizes can be distinguished since both sizes of beads (500 μm and 800 μm) are well within the resolving power of the instrument. As predicted, the large bandwidth of the spectral sensitivity of the imaging device in different channels results in the observation of more than one of the dyes in multiple channels. Also the wide spectral bandwidth of the fluorescent emission of the dyes enables this observation. Note that no spectral signal was observed in CH6 since none of the fluorescent dyes emit in this wavelength range.

The experiment demonstrates the simultaneous spatial-spectral data acquisition capabilities of the instrument albeit at a prescribed field-of-view size.

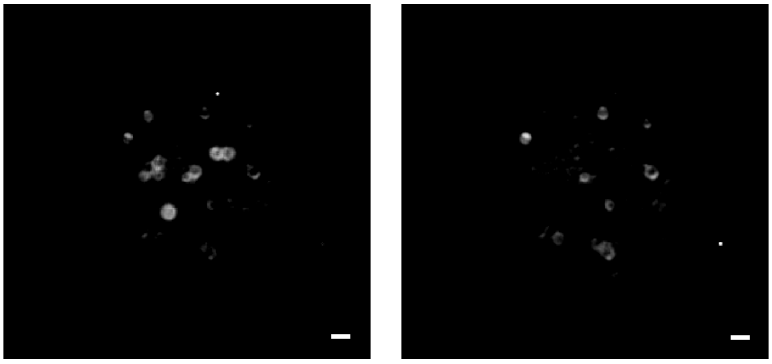

(a) CH1 - 472 ± 45 nm

(b) CH2 - 540 ± 48 nm

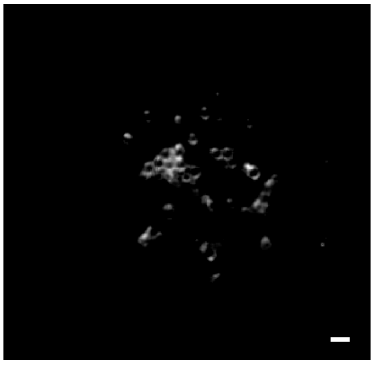

(c) CH3 - 635 ± 70 nm

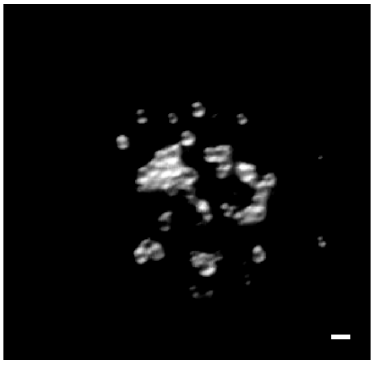

(d) CH4 - 705 ± 62 nm

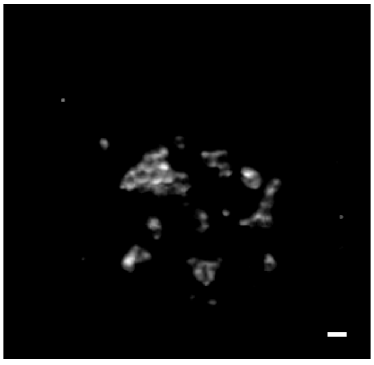

(e) CH5 - 854 ± 21 nm

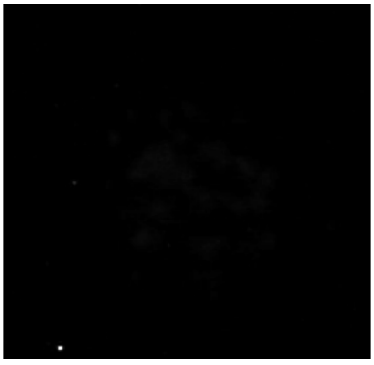

(f) CH6 - 932 ± 62 nm

Figure 5.1: The six channel multispectral image of the fluorescent plastic beads of 500 μm and 800 μm in size. There is no observation made in CH6 as there exists no fluorescent dye with emission in this spectral range. The scale bar denotes 1 mm.

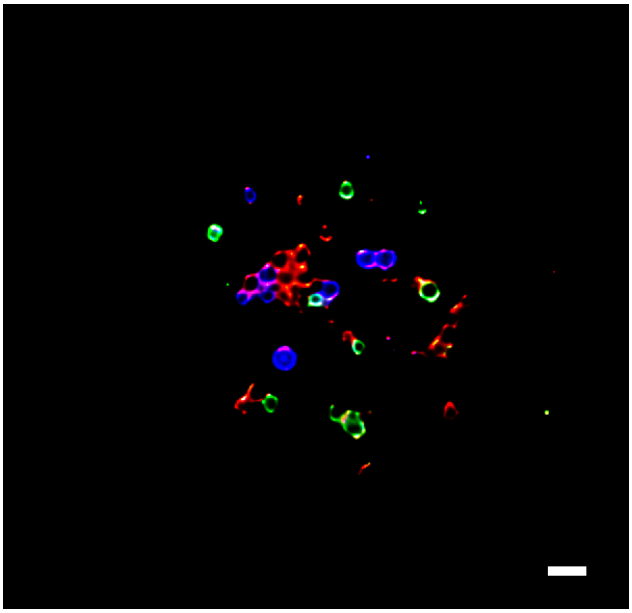

(a) VIS

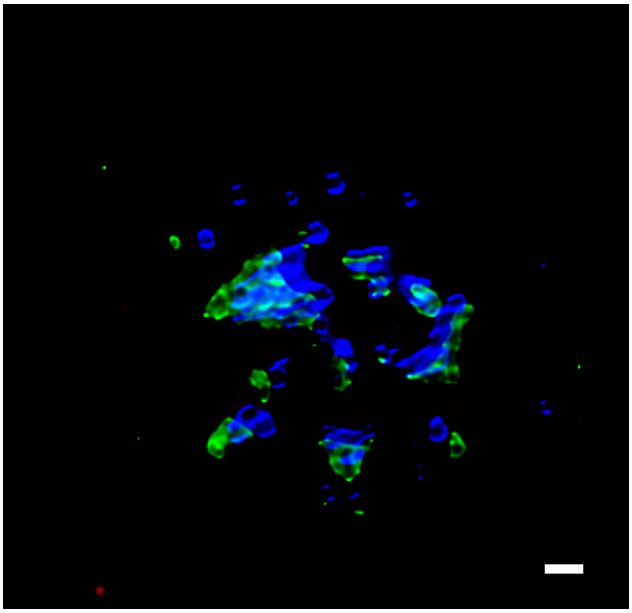

(b) NIR

Figure 5.2: The color composite images of the fluorescent beads in the visible and the NIR. In the NIR image (b) CH4 is represented in blue, CH5 is represented in green, and CH6 is represented as red. The scale bar denotes 1 mm.

5.2 Adulteration in Edible Oils

Adulteration is the process of adding an adulterant, a substance usually banned or harmful, to another substance. This process will result in an impure mixture of various products mainly, food, beverages, and fuel. The main purpose of adulteration is to artificially create a substance or feign the existence of a substance that does not actually exists. There are many examples of adulteration especially in the food industry such as addition of urea or melamine to inflate the crude protein content of a meat product, adding high fructose corn syrup to increase volume of honey production, and water or brine injected into poultry to increase their weight [26].

Most common methods of detection adulteration use techniques of chemometric analysis for the classification of food adulteration. The techniques include spectroscopy (UV, NIR, mid-wave IR, visible, Raman), isotopic analysis, chromatography, electronic nose, polymerase chain reaction, enzyme-linked immunosorbent assay, and thermal analysis [105]. These methods are used to explicitly qualify and quantify the type and the amount of adulteration in a food sample.

Adulteration of edible oils has become a recent issue as more oil producers are adding low-quality edible oils such as Palm Olein oil, which is more cost effective, to adulterate high-quality oils such as mustard oil in order to inflate the volume to maximize income. The measurement techniques proposed above can detect the presence of the adulterant in a contaminated batch of mustard oil however very few of them allow for the measurement and examination to be done *in-situ*.

The multispectral interrogation of the fluorescent emission of edible oils can be imaged using the proposed system and using the computational tools developed, adulteration can be detected on-site in a matter of seconds. Granted the amount of the adulterant and the exact composition of it may not be clear but as a quick pass-fail (contaminated-not contaminated) test, the proposed system will be sufficient and desirable. The work presented here is a continuation of and improvement on the previously published work by the author [64].

A selection of high-end cooking oils such as rice bran, mustard, sunflower were used in this test as well as a low-quality palm and soy cooking oils. The samples were placed in Methyl Methacrylate cuvettes which have very high transmission efficiency from UV to the

NIR [1]. The mustard oil was contaminated with the palm oil at different percentages (5%, 10%, and 20%) by volume. The mustard oil was placed in a beaker and placed in a warm water bath. The palm oil was then added to the mustard oil performing the adulteration by volume 95 parts to 5 parts mustard to palm oil, then repeated to achieve 90 parts to 10 parts mustard to palm oil and 80 parts to 20 parts mustard to palm oil. The purpose of the warm bath is to ensure thorough mixture of the two oils. The mixtures were then placed using a cuvette using a pipette.

The oil samples were maintained at room temperature ($\sim 24^\circ$ C) and were illuminated using a 5 mW green laser, wavelength 532 nm, in order to induce fluorescence. The fluorescence emission was observed in a direction orthogonal to that of the excitation light.

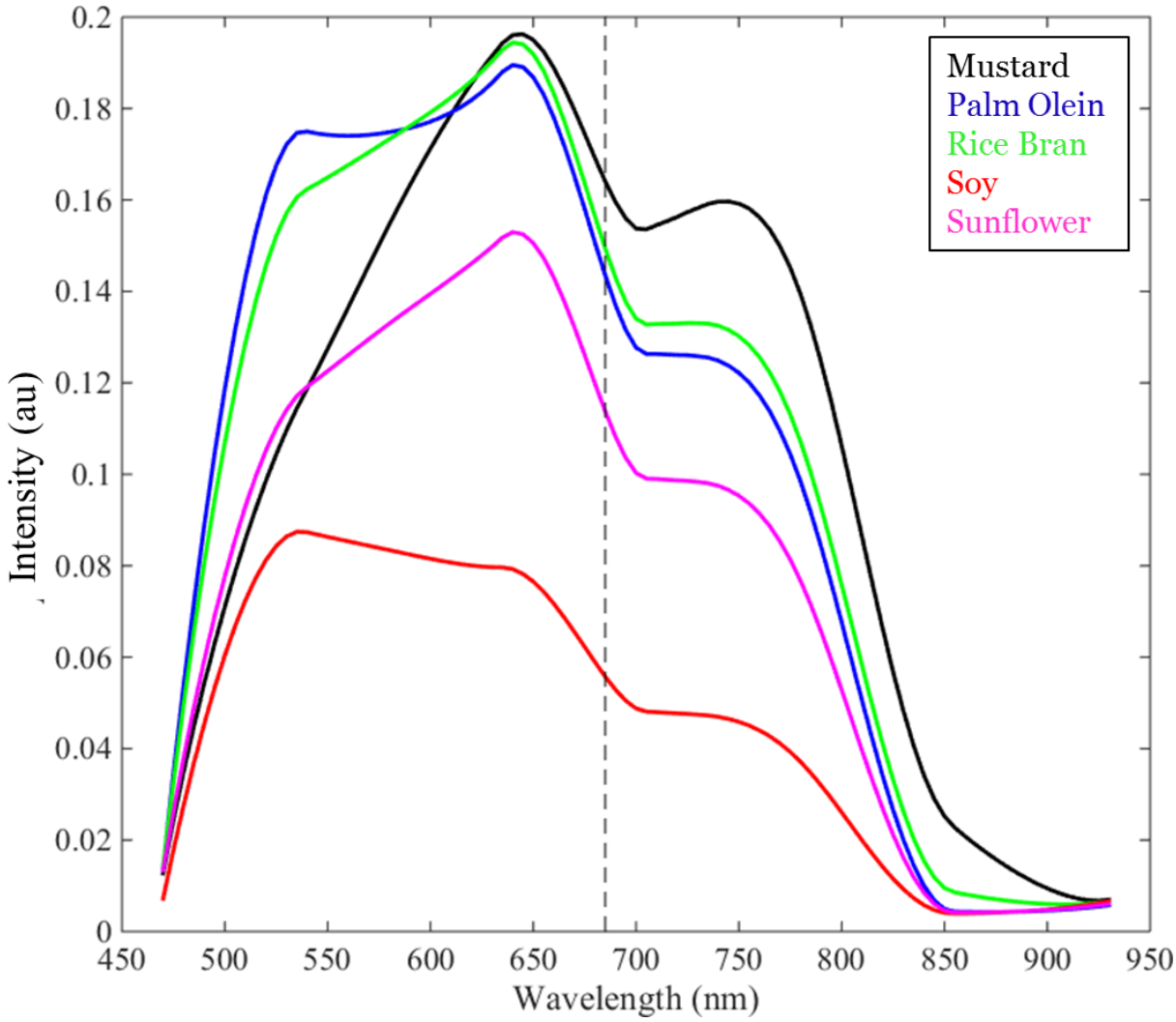

Figure 5.3: A six-channel spectrum of the five edible oils, mustard oil (black), palm oil (blue), rice bran oil (green), soy oil (red), sunflower oil (magenta). The vertical dashed line is to separate the visible region (to the left of) and the near infrared region (to the right of) of the spectrum.

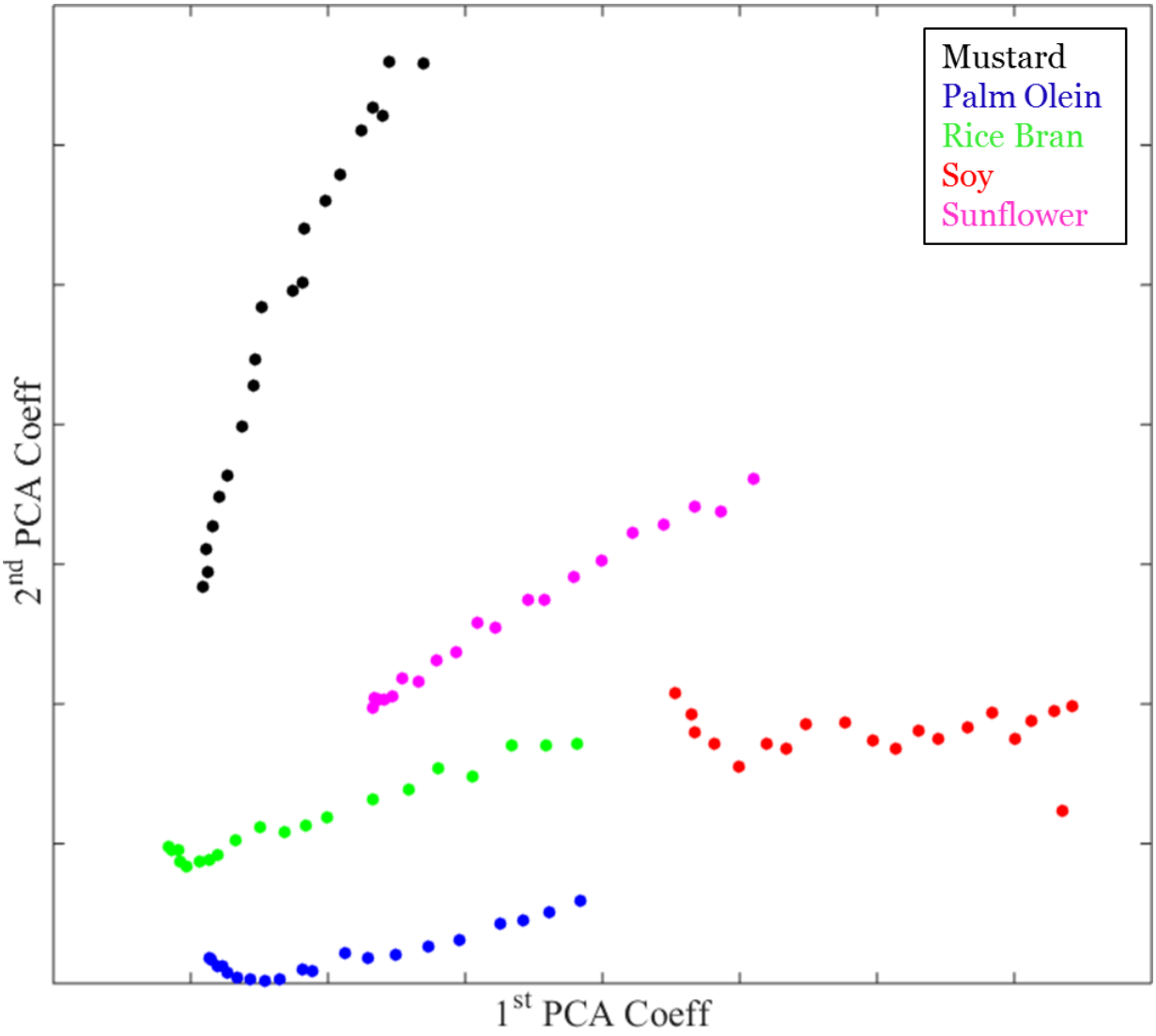

Figure 5.4: The PCA space containing the five edible oils clusters, mustard oil (black), palm oil (blue), rice bran oil (green), soy oil (red), sunflower oil (magenta).

The fluorescence spectra of the edible oils are shown in Figure 5.3. It is noted that each of the oils, in their pure non-adulterated form, has a very different spectrum than any other oil. In principle, it should be relatively trivial to distinguish between the pure forms of these oils by simply examining their six-channel multispectral spectra and comparing it to the spectra shown in Figure 5.3. Principal component analysis of the multispectral data can more readily distinguish between the oils as evident in Figure 5.4. Each of the oils is occupying a specific region in the PCA space. The rigid structure of the PCA clusters could be due to the quantization of the dynamic range of the detector since the 16-bit images captured by the imaging device are translated to 8-bit images. The quantization resulting from bit-rate reduction of the dynamic range can manifest itself in quantization of the PCA coefficient values.

The effects of adulteration of the pure oils can similarly be observed via the fluorescence spectra of the oil. Palm oil is used to adulterate mustard oil at 5%, 10%, and 20% contamination rate by volume. The fluorescence spectra of the pure mustard and palm as well as the adulterated mustard oil at different rates are shown in Figure 5.5. It is immediately apparent that the spectra of the adulterated oils differ significantly from either one of their progenitors. The adulterated oils have their own unique spectral shape and an increase in the concentration of the contamination results in the decrease of the total fluorescence emission, which is the integral of the spectral curve.

To examine the uniqueness of the adulterated oils in a lower dimensional space the PCA was employed and its results are shown in Figure 5.6. The figure shows a set of plots generated using the first and second PCA coefficients. Figure 5.6 shows the location of the mustard and palm clusters as well as the three adulterated concentrations of the two. It was expected to observe the three contamination clusters in the linear space adjoining the two oils however this isn't the case. Nevertheless, in the PCA space the location of the two pure samples of the oils are clearly defined and the adulterated sampled clearly fall outside of these regions and can therefore be classified as non-pure samples.

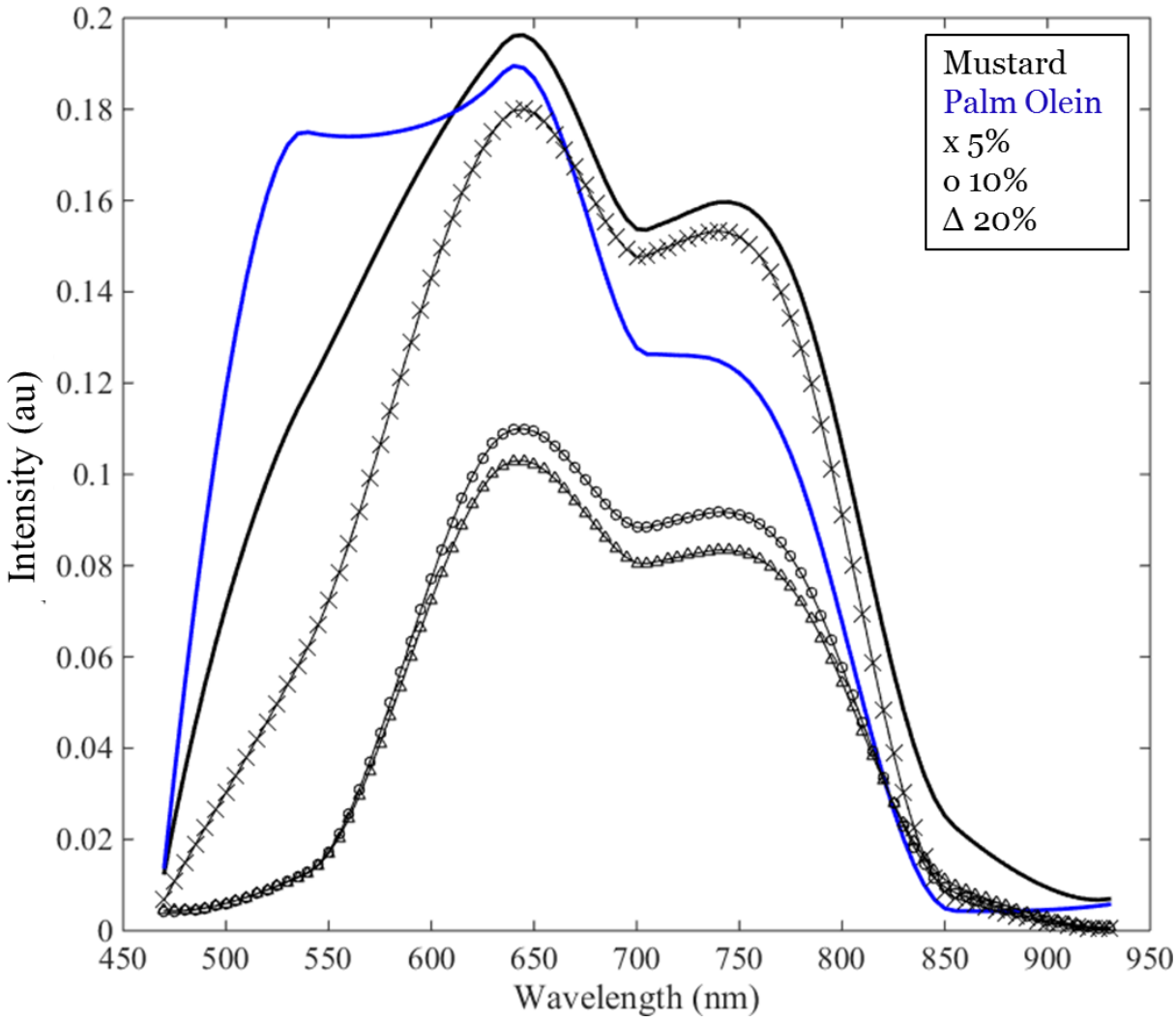

Figure 5.5: A six-channel spectrum of the palm oil (blue) and mustard oil (black). The adulterated mustard oil samples at different concentrations of palm oil are over plotted; 5% palm oil contamination (connected crosses), 10% palm oil contamination (connected circles), 20% palm oil contamination (connected triangles).

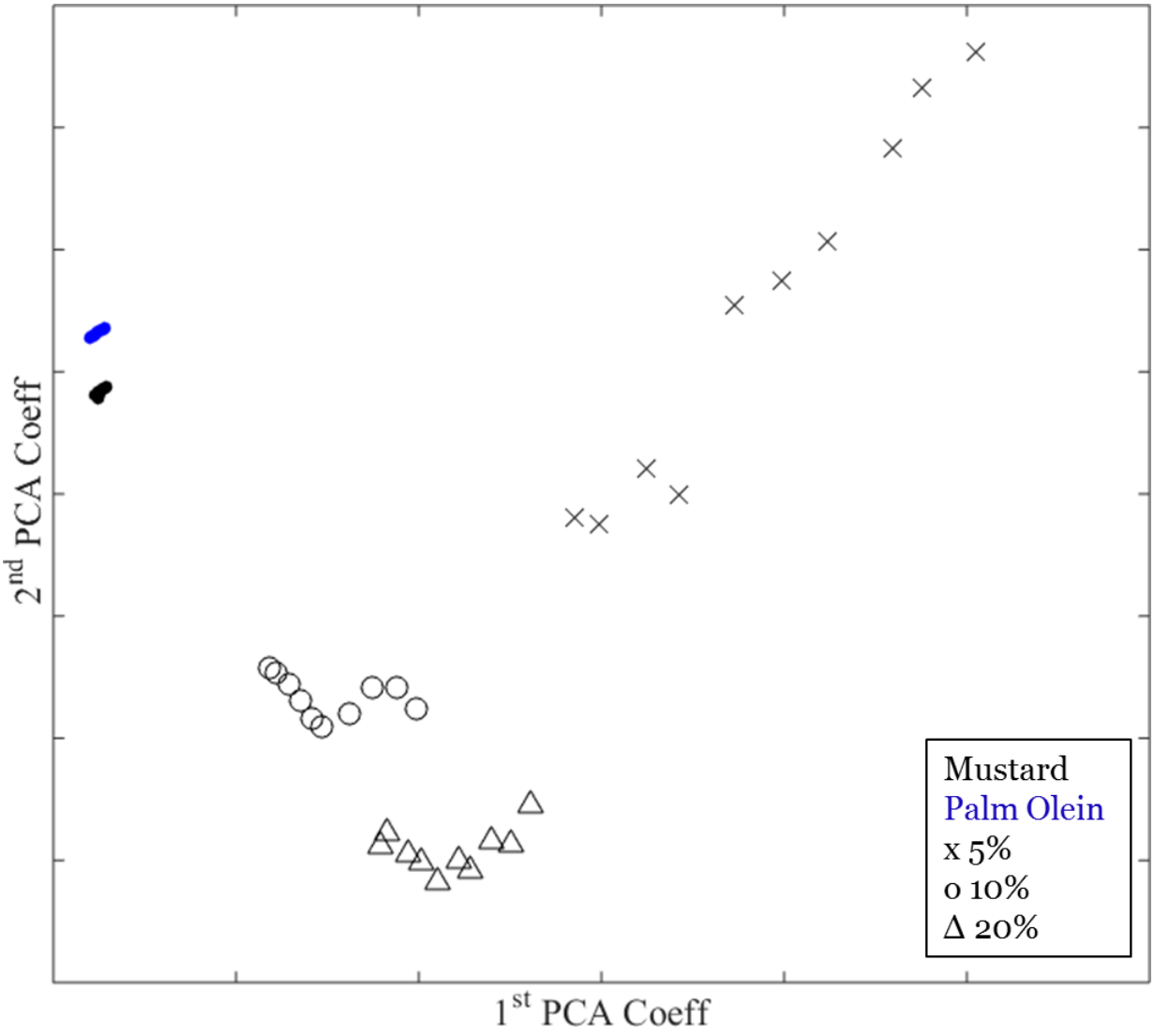

Figure 5.6: The results of PCA of mustard oil (black) contaminated with palm oil (blue) and 5% palm oil contamination (crosses), 10% palm oil contamination (circles), 20% palm oil contamination (triangles).

5.3 Ink Analysis for Counterfeit Detection

The purpose of this study is to examine the capability of the instrument in differentiating between five different type of black ink. Here, 'types of ink' is imply referring to the manufacturers of the pens that are used. The purpose of this study is not to determine the chemical composition of the inks but to simply discern the difference between the ink from different pens. This study is a continuation of and improvement on the previously published work by the author [65].

It is obvious that the observed color of the ink from all of the pens in the visible range is the same and differentiating between the inks in order to determine which pen was used to make a certain mark is close to impossible. However, by observing the reflective and scattering properties of the inks in the NIR as well as the visible wavelength range, some differences in the inks are observed. These differences could lead to differentiating the inks and thereby determining which pen and by extension from which manufacturer the marking came from. The reflection of the light measured in this experiment is governed by the Mie scattering theory.

The most rudimentary approach for carrying out this classification would be to represent the intensity measured at each wavelength in the form of a six-channel spectrum, shown in Figure 5.8. The individual spectrum of the five inks tends to be very similar with very little departure from one another except maybe in the first and last channels in the visible and the NIR, respectively.

The spectra, as presented, have been corrected for the illumination source which was a Tungsten-Halogen broadband source at 3500 K. The spectra have also been corrected for the detector quantum efficiency in order to capture the true reflectance spectra of the inks across the wavelength range presented. As mentioned previously, only six true spectral measurement have been made and the missing intensity value between the measured channels have been interpolated.

Following the computational imaging procedures introduced in this work, more specifically the implementation of the data fusion § 4.4, principal component analysis can be performed on the six-channel data of the black inks. To verify the fidelity of the data fusion process a sample of spots was created using the five inks, shown in Figure 5.7. To demonstrate the power of the multispectral data across the visible and the NIR spectral

regions, the PCA was also performed using only the three channels in the visible, Figure 5.9 top, and the three NIR channels, Figure 5.9 bottom. These figures show the first and second PCA coefficients which are selected for having the largest variance (eigenvalue). From these figures it is clear that no real distinction can be made between the five black inks in the visible or the NIR separately. Combining all six channels in the PCA process, Figure 5.10, will result in five extremely well separated clusters that define the extent of each ink in the two-dimensional PCA space, therefore, each ink can be identified. It may be worth mentioning that the data points in Figures 5.9 and 5.10 are pixels that contain the image of each of the five inks.

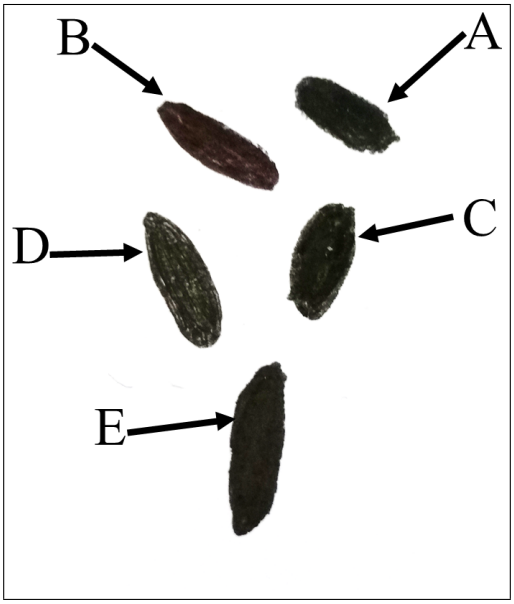

Figure 5.7: The image of the ink spots drawn at random with the five pens.

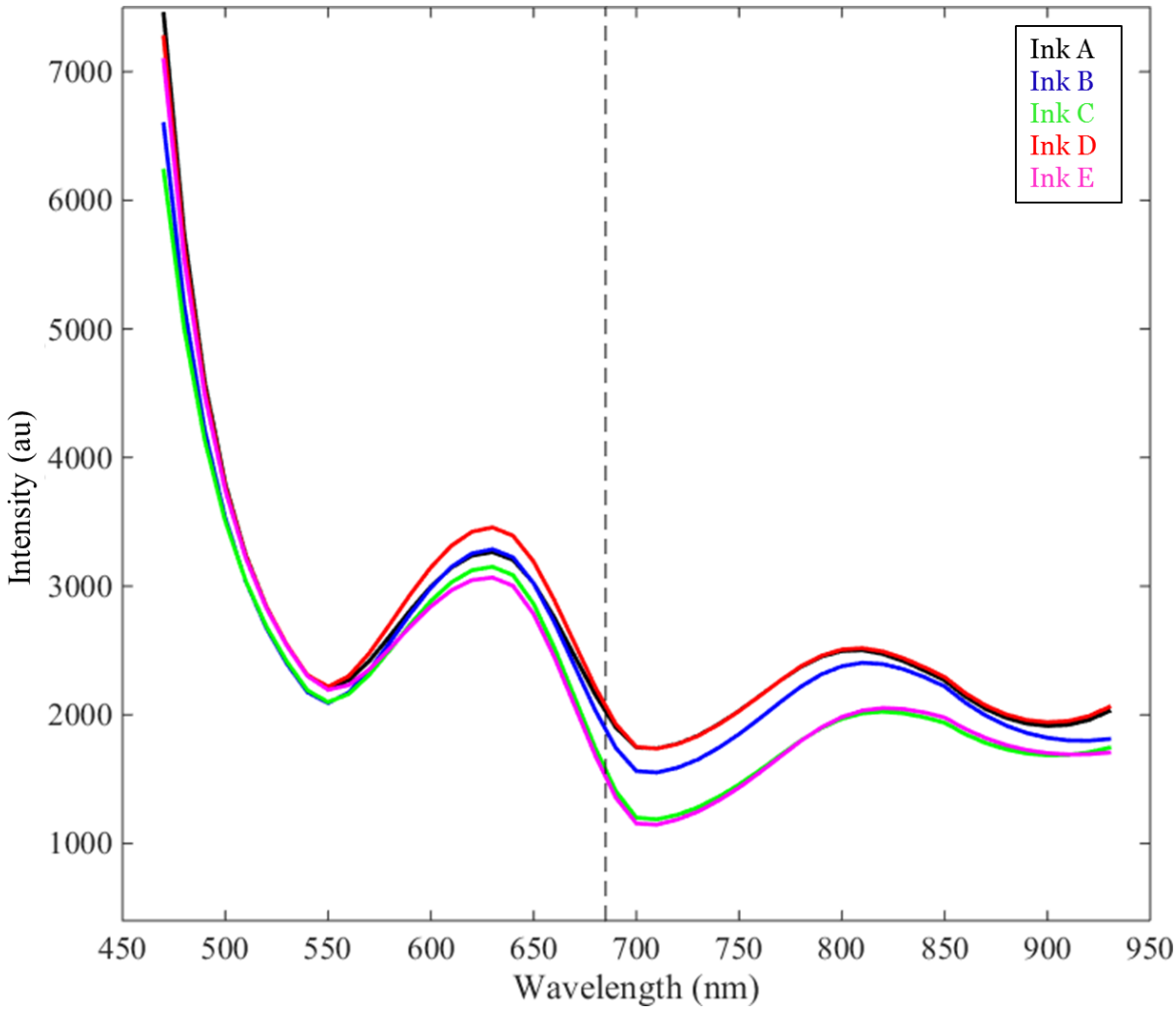

Figure 5.8: A six-channel spectrum of the five black inks from five black pens from different manufacturers, ink A (black), ink B (blue), ink C (green), ink D (red), ink E (magenta). The vertical dashed line is to separate the visible region (to the left of) and the near infrared region (to the right of) of the spectrum.

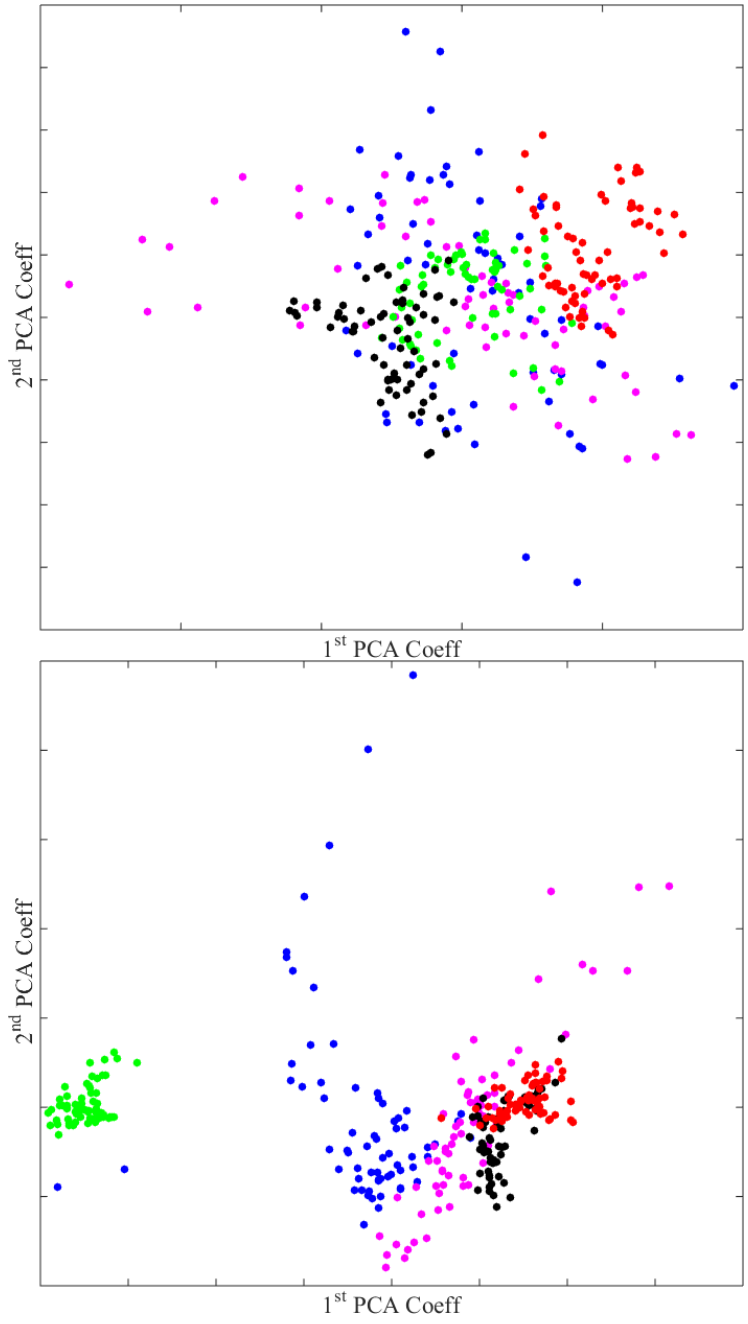

Figure 5.9: The result of separate PCA analysis in the visible and the near infrared spectral channels of the five black inks from five black pens from different manufacturers, visible (top) and near infrared (bottom). Ink 1 (black), ink 2 (blue), ink 3 (green), ink 4 (red), ink 5 (magenta).

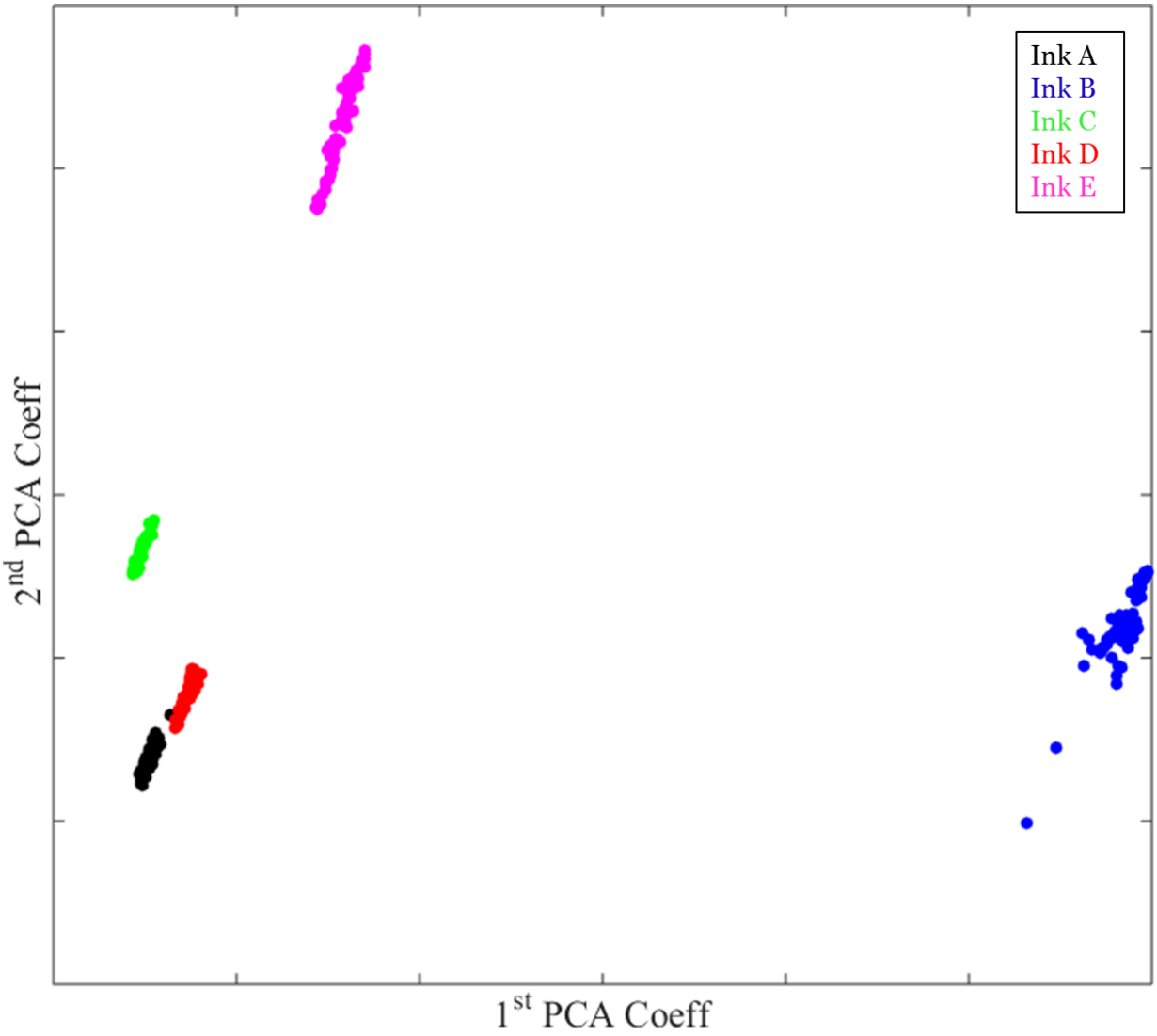

Figure 5.10: The result of the PCA using all six spectral channels of the ink images show clear separability between the five inks. ink A (black), ink B (blue), ink C (green), ink D (red), ink E (magenta).

It has been shown that using multispectral information to perform PCA, in this case, the five inks are clearly separated from one another and having prior knowledge of which pen was used to create each of the spots it can be concluded that dot A was created using ink 1, dot B was created using ink 2, dot C was created using ink 3, dot D was created using ink 4, and dot E was created using ink 5. The fact that spots A, B, C, D, and E were drawn using inks 1, 2, 3, 4, and 5 is completely coincidental and was not by design. It can be observed that in the PCA space inks 1 and 4, even though very similar, are in fact separated however the spectra of these two inks, Figure 5.8, are identical and separability solely using the spectrum is not possible.

The impact of such capability as presented here is in paper currency counterfeit detection and forensics as well as any facet of forgery that may require the use of pigment such as ink. These facets may include document forgery, photography, and paintings. Alternatively, such a system can be used to study alteration to works of art such as paintings, done by the artist [33, 122, 123].

Chapter 6

Conclusions

The need for having *in-situ* sensing technologies, for various applications, is continually increasing. Over the past decade, multispectral imaging has become one of the main imaging modalities in diverse fields such as science, technology, and industry. Optical imaging instruments have also experienced a 'renaissance' in the sense that there has been considerable effort put toward miniaturizing, reducing cost and complexity, and increase in the usability of imaging instrument which have historically been 'bench-top' devices. To this end, this work set out to devise a portable, point-and-shoot simultaneous multispectral imaging device using the advanced concepts of single-detector multiview imaging, compressive sensing, and computational imaging. This goal has been accomplished by designing a series of optical and computational augmentation that can be adapted for any image forming device.

In Chapter 3 the hardware implementation of the design was presented. The requirements and considerations of the light source needed for such an instrument are laid out depending on the imaging mode (reflectance or fluorescence) that the instrument is to be used in. In fluorescence mode, the light source has to be chosen adhering to the samples that are to be examined, as some sample are activated by UV radiation and some others require single frequency (laser) radiation.

Next, the field-of-view replicating device is discussed and its design is detailed. This device contains four mirrors placed at a specific distance from the optical axis of the instrument and angled in such a manner that are able to reflect and redirect the beams of

light coming off of the sample, that would have otherwise missed the imaging device, into it for acquisition. The design allows for the replication and simultaneous multiview image capture of five POVs of an FOV that is $\sim$ 30 mm in size and imposes a distance of $\sim$ 75 mm at which the sample needs to be placed with respect to the instrument.

Following the optical path, the spectral filtering device is designed and placed in the optical path of the multiple POVs to select the spectral range that enters the imaging device in each POV. The combination of the spectral transmission of this device and the spectral response of the Bayer color filter array on the detector of the imaging device define the spectral channels that are observable by the instrument. The combination of the two spectral filtering mechanisms results in six unique spectral channels spanning the visible and the NIR region of the electromagnetic wavelength (400 - 1100 nm).

Lastly, the design and some specifications of the unit that houses the FOV replicating device and the spectral filtering device are presented. This unit is designed specifically for the imaging device used in this work and will have to be adapted to other imaging devices before deployment.

Chapter 4 presents the software implementation of the instrument presented in this work. The simultaneity of the image capture or rather the multiview nature of the image acquisition naturally results in misalignment of the five images which have to be aligned for any multispectral, multidimensional analysis to be conducted. The process of image registration is never ideal and there always exists minor misalignment despite all efforts. It was determined that manual registration results in much less registration error (less than one pixel), or misalignment, than any automatic, intensity-based, registration process.

Selecting spectral channels from the available Bayer color filter array and registration results in extremely sparse spectral images. This means that in an image of a given channel there exists very few pixels with actual measurement and the majority of the pixels have no information whatsoever. The process of registering the six channels results in a super image where only 20% of its pixels have a measurement and the rest (80%) are empty. The distribution of the spectral sensing is random across this super image and to fully construct the image, the use of sparse interpolation algorithms is necessary.

Defocusing is determined to be the main aberration present in the instrument, specifically driven by the imposition of the FOV replicating device. This aberration is therefore

addressed by a hyper-focusing process which includes a modified Tenengrad focus metric to measure the level of focus and uses a Bayesian-based maximum a posteriori iterative method to perform the refocusing of the images of each of the POVs. It has been shown that this method improves the quality of the images in all five POVs as well as increasing the lateral resolution of the three of the five POVs by more that 20%. Interestingly, the effects of the modulation transfer function of the complex lens design of the imaging device was observed using the Tenengrad focus metric.

Lastly, a dimensionality reduction algorithm, principal component analysis, is implemented and used to extract information from the multidimensional multispectral data.

The efficacy of the instrument is then tested using three different samples in Chapter 5. First, two different micron-sized plastic beads were coated using fluorescent dyes with emission wavelengths spanning five of the six spectral channels. The spatial-spectral imaging capabilities of the instrument were demonstrated using this sample. Second, adulteration in edible oil was discovered using fluorescent spectral analysis. Lastly, the reflectance spectra of five different black inks were measured using the instrument which was able to differentiate between the inks and determine which of the five different pen manufacturers' ink has made a certain marking.

The work presented here is patent pending under the United States and the Canadian patent offices [67].

6.1 List of Contributions

A list summarizing the unique and major contributions of this work are as follows:

- A method and optical design of a FOV replicating device, enabling the multiview imaging capability (§ 3.2);
- A method and optical design of a simultaneous spectral filtering device from visible to the near infrared (§ 3.5);
- A method of performing spectral characterization of an image capturing device as well as additional characterization of the image capturing device such as noise floor, dead pixels, quantum efficiency, white balancing, etc. (§ 3.4);

- A design and implementation of housing and attachment mechanism of the FOV replicating and the spectral filtering devices for adaptation to any image capturing device (§ 3.6);
- A method of performing spectral compressive sensing via simultaneous multispectral imaging on a single imaging device (§ 4.2);
- A method and implementation of a hyper-focusing technique for addressing any defocusing aberration in any image capturing device (§ 4.3);
- Interpretation of extracted information from multispectral data using dimensional reduction analysis (§ 4.4).

6.2 Limitations

As designed and presented the system has certain limitations that may prevent its usability, as designed, for a wide variety of applications. The design and implementation of the instrument is such that there may be the need to customize the instrument depending on the application.

1. The spectral channels that currently exist in the instrument are the result of the convolution of the spectral response of the field filters in the spectral filtering device and the Bayer color filter array of the imaging device. If a finer control over the resulting spectral channels is desired the spectral field filters can be chosen to have a much narrower spectral bandwidth to decrease the spectral extent of a given channel. Currently, the spectral channels have been designed with considerable overlap in order to enable the spectral demultiplexing capability discussed in the next section;
2. The size of the field-of-view of the instrument is limited by the area of the reflecting surfaces used in the FOV replicating device and the available detector area. Currently, the maximum size of the FOV that can reliably be observed in all POVs is $\sim$ 30 mm;

3. The working distance of the instrument which is tied in closely with the size of the FOV is fixed. In other words, if the maximum FOV is to be observed then the distance between the sample and the instrument is fixed. Currently, this distance is ~ 75 mm;

4. The manual registration process is a lengthy and arduous process, this can be remedied by using some advanced feature extraction techniques to automatically find and match various features/pixel locations in different images [9, 62];

5. The data fusion, dimensional reduction algorithm presented here, principal component analysis, is a very basic form of data analysis and there exists more complex version of such algorithms which would aid in better analysis of the data and thereby lead to more accurate interpretations [120, 121].

6.3 Extensions and Future Work

The system presented in this work lends itself to many short-term and long-term modifications and applications, a selection of which is presented in this section.

6.3.1 Light Source Design

Depending on the application and the observation mode, reflectance or induced emission (fluorescence), the light source for the instrument will have to be catered accordingly.

As described in Chapter 3, in reflectance mode the relative optical power across the visible and the NIR spectrum have to be equalized with respect to the QE and the transmission efficiency of the hardware implementation. This is an important point since in order to adequately make observations in each of the spectral bands, sufficient number of photons will have to be collected by the detector. The system uses a global exposure time in the process of acquiring the multispectral images, therefore, each of the six spectral channels need to have the opportunity to collect sufficient amount of light to have at least an SNR of three based on the photon statistics presented in § 3.4.2. This leads to a custom light source design in which the emission power at the NIR range is much higher than

the emission in the visible part of the spectrum. Additionally, in reflectance mode, it is crucial that the sample is illuminated uniformly. To accomplish uniform illumination the light source could be designed to form a ring about the hardware, thereby illuminating the sample from many directions the additive effect of which is a uniform intensity pattern illuminating the sample.

For induced emission, whether using a UV lamp or a laser for excitation, the emission power is proportional to the excitation power however there exist limits on the power of the excitation light sources. Nevertheless, the optical power of the fluorescence emission is not very strong and emission at wavelengths farther away from the excitation wavelength is weaker. To this end some hardware modification is required which would be implemented in the spectral filtering device. This modification will be the inclusion of a neutral density filter in the POV that observes the visible region of the spectrum. A neutral density filter works to reduce the transmitted intensity of a beam, at the same level, in the wavelength range of interest [12, 107]. The visible wavelengths are observed in POV I and II and by equalizing the intensity of light entering the imaging device across the visible and the NIR wavelength range, once again a global exposure time can be imposed to enable measurement across the entire spectrum.

6.3.2 Three-Dimensional Topographical Reconstruction

The optical design of the FOV replicating device and the multiview nature of the imaging naturally lends itself to evaluation of depth information of the FOV. Multiview stereo imaging, as it is known, is an active research area which has made improvements upon the traditional two-view stereo imaging [95, 118]. The increase in the number of POVs increases the robustness in the feature extraction and mapping used in three-dimensional reconstruction and reduces the negative effects of inherent image noise and surface texture.

The proposed device has been used to successfully produce a three-dimensional reconstruction of an artificial sample [65]. The process of producing a topographical model of the FOV consists of observing and finding corresponding features in each of the POVs and simply by triangulation, the distance from the imaging device to each of the features can be determined.

Another technique that can be used to produce a topographical reconstruction of the

FOV is the extent of defocus of the image. By extending the hyper-focusing technique combined with the Tenengrad focus metric proposed in this work, deviations from the focal plane of the camera can be calculated and depth information can be inferred from the power of the hyper-focusing technique [14].

6.3.3 Spectral Demultiplexing

Multispectral observations are inherently limited in the number of spectral bands available for making observations. There are numerical or computational methods that enable extraction of hyperspectral information from multispectral observations such as the well-known Wiener spectral estimation method [113]. As an example, the multispectral spectra that are shown in Chapter 5 are the result of mathematical interpolation to estimate the missing values between the actual measured spectral response which may not accurately represent the actual, real, spectra. Spectral demultiplexing methods tend to more intelligently perform the estimation of the missing spectral value based on the measurements made and some intrinsic properties of the imaging device itself. Some of these methods, proposed by the author, include non-linear regression modeling or random forest modeling which tend to maintain the spectral fidelity of the observation in the process of producing a hyperspectral image from multispectral data acquired [32, 31, 30, 29].

6.4 Impact and Relevance to Other Fields

The applications and use of multispectral imaging systems are becoming more and more ubiquitous, specifically when such a system is portable and low-cost. There are diverse fields that can take advantage of and benefit from such a system, from biomedical imaging, to food and agriculture, to environmental monitoring, and gemology.

An application that is giving multispectral imaging a lot of traction is dermatology and the detection of different forms of skin cancer, melanoma and basal cell carcinoma. In this field multispectral imaging is used to examine the concentration of various constituents of skin at the location of a lesion and examine the vascular composition and pigment network of the skin lesion [13, 85, 88].

The assessment of the quality and safety of food is of utmost importance and has gained much publicity in recent years. Multispectral imaging is readily adopted for the monitoring of various processing lines. This imaging modality is quickly becoming one of the more used since it can enable real-time process control and monitoring while being non-destructive and non-contact [57, 102]. This type of imaging can be used to assess the freshness of produce in order to determine its shelf-life as well as the over-ripening and internal bruises or spoilage of food that are not otherwise observable.

Water processing facilities can benefit from a multispectral imaging system to continually search for sources of contamination in the water. Pathogenic contamination can be detected on large scales using fluorescence multispectral imaging for those pathogens that auto-fluorescence such as *E. Coli* or Cyanobacteria [17, 23].

Lastly, multispectral imaging cameras have been proposed for observing various jewels including diamonds and gem stones to be used for grading the stones and determining different qualitative factors quantitatively.

References

[1] R. M. Ahmed. Optical study on poly(methyl methacrylate)/poly(vinyl acetate) blends. *International Journal of Photoenergy*, 2009(150389), August 2009. 108

[2] D. Alleysson, S. Susstrunk, and J. Herault. Linear demosaicing inspired by the human visual system. *Image Processing, IEEE Transactions on*, 14(4):439–449, April 2005. 71

[3] R. Amelard, C. Scharfenberger, F. Kazemzadeh, K.J. Pfisterer, B. Lin, A. Wong, and D.A. Clausi. Non-contact transmittance photoplethysmographic imaging for long-distance cardiovascular monitoring. *Nature Scientific Reports*, 5(14673), 2015. 7

[4] D.A. Atchison and G. Smith. *Optics of the Human Eye*. Butterworth-Heinemann, 2000. 35

[5] Avantes. Avalight-hal tungsten halogen light source. http://www.avantes.com/Chemistry/AvaLight-HAL-Tungsten-Halogen-Light-Source/Detailed-product-flyer.html, 2013. Accessed: June 27, 2013. 32

[6] R.G. Baraniuk. Compressive sensing. *IEEE Signal Processing Magazine*, 29:118–124, July 2007. 9

[7] H.H. Barrett and K.J. Myers. *Foundations of Image Science*. Wiley series in pure and applied optics. Wiley-Interscience, 2004. 38, 83

[8] M. Bass, C. DeCusatis, J. Enoch, V. Lakshminarayanan, G. Li, C. Macdonald, V. Mahajan, and E. Van Stryland. *Handbook of Optics, Third Edition Volume I: Geometrical and Physical Optics, Polarized Light, Components and Instruments(Set)*. McGraw-Hill, Inc., New York, NY, USA, 3 edition, 2010. 24

[9] H. Bay, A. Ess, T. Tuytelaars, and L. Van Gool. Surf: Speeded up robust features. In *Computer Vision and Image Understanding (CVIU)*, volume 110, pages 346–359, 2008. 125

[10] B.E. Bayer. Color imaging array, July 20 1976. US Patent 3,971,065. 18

[11] J. Beeckman, K. Neyts, and P.J.M. Vanbrabant. Liquid-crystal photonic applications. *Optical Engineering*, 50(8):081202–081202–17, 2011. 7

[12] K.E. Bennett and J.R. Staley. Neutral density filters, May 28 1991. US Patent 5,018,833. 126

[13] K.S. Bersha. Spectral imaging and analysis of human skin. Master's thesis, University of Eastern Finland, June 2010. 127

[14] B. Billiot, F. Cointault, L. Journaux, J.C. Simon, and P. Gouton. 3d image acquisition system based on shape from focus technique. *Sensors*, 13(14):5040–5053, April 2013. 127

[15] D.A. Boas, D.H. Brooks, E.L. Miller, C.A. DiMarzio, M. Kilmer, R.J. Gaudette, and Z. Quan. Imaging the body with diffuse optical tomography. *Signal Processing Magazine, IEEE*, 18(6):57–75, Nov 2001. 18

[16] J. Bobin, J.L. Starck, and R. Ottensamer. Compressed sensing in astronomy. *Selected Topics in Signal Processing, IEEE Journal of*, 2(5):718–726, Oct 2008. 9

[17] J.R. Bordowitz and B.L. Montgomery. Exploiting the autofluorescent properties of photosynthetic pigments for analysis of pigmentation and morphology in live fremyella diplosiphon cells. *Sensors*, 10(7):6969, 2010. 128

[18] M. Born and E. Wolf. *Principles of Optics*. Cambridge University Press, seventh edition, 1999. 24, 48

[19] D.J. Brady, K. Choi, D.L. Marks, R. Horisaki, and S. Lim. Compressive holography. *Opt. Express*, 17(15):13040–13049, Jul 2009. 9

[20] J.B. Breckinridge, , W.S.T. Lam, and R.A. Chipman. Polarization aberrations in astronomical telescopes: The point spread function. *Publications of the Astronomical Society of the Pacific*, 127(951):445–468, May 2015. 30

[21] M.A. Bueno-Ibarra, J. Alvarez-Borrego, L. Acho, and M.C. Chavez-Sanchez. Fast autofocus algorithm for automated microscopes. *Optical Engineering*, 44(6):063601–1–8, 2005. 85

[22] E.J. Candes. Compressive sampling. In *Proceedings of the International Congress of Mathematicians*, volume 3, pages 1433–1452, 2006. 9

[23] V. Chalova, C.L. Woodward, and S.C Ricke. Application of an Escherichia Coli green fluorescent protein-based lysine biosensor under nonsterile conditions and autofluorescence background. *Letters in Applied Microbiology*, 42(3):265–270, 2006. 128

[24] S. Chandrasekhar. *Radiative Transfer*. Dover Publications, 1960.

[25] P. Coffey. *The Science of Logic*. Longmans, Green and Company, 1912. 4

[26] N.G. Coley. The fight against food adulteration. Online, March 2005. 107

[27] K.B. Crozier, H.Park, K. Seo, P. Steinvurzel, E. Schonbrun, Y. Dan, T. Ellenbogen, P. Duane, and M. Wober. Harnessing the nano-optics of silicon nanowires for multispectral imaging. *IEEE Photonics Society News*, 27:11–18, 2013. 8

[28] M. Czerny and A.F. Turner. Über den Astigmatismus bei Spiegelspektrometern. *Zeitschrift fur Physik*, 61:792–797, November 1930. 45

[29] J. Deglint, F. Kazemzadeh, D. Cho, D.A. Clausi, and A. Wong. Numerical spectral demultiplexing microscopy from an anatomical specimen. *Vision Letters*, 1(1):VL102, 2015. 127

[30] J. Deglint, F. Kazemzadeh, D. Cho, D.A. Clausi, and A. Wong. Numerical demultiplexing of color image sensor measurements via non-linear random forest modeling. *Optics Letters*, Submitted. 127

[31] J. Deglint, F. Kazemzadeh, A. Wong, and D.A. Clausi. Inference of dense spectral reflectance images from sparse reflectance measurement using non-linear regression modeling. In *SPIE Proceedings*, volume 9599, pages 95992G–95992G–9, 2015. 127

[32] J Deglint, F. Kazemzadeha, M.J. Shafiee, E. Li, I. Khodadad, S.S. Saini, A. Wong, and D.A.Clausi. Virtual spectral multiplexing for applications in *In-situ* imaging microscopy of transient phenomena. In *SPIE Proceedings*, volume 9599, pages 95992D–95992D–9, 2015. 127

[33] J.K. Delaney, J.G. Zeibel, M. Thoury, R. Littleton, M. Palmer, K.M. Morales, E.R. de la Rie, and A. Hoenigswald. Visible and infrared imaging spectroscopy of picasso's harlequin musician: Mapping and identification of artist materials in situ. *Appl. Spectrosc.*, 64(6):584–594, Jun 2010. 119

[34] D.L. Donoho. Compressed sensing. *Information Theory, IEEE Transactions on*, 52(4):1289–1306, April 2006. 9

[35] M.F. Duarte, M.A. Davenport, D. Takhar, J.N. Laska, T. Sun, K.F. Kelly, and R.G. Baraniuk. Single-pixel imaging via compressive sampling. *IEEE Signal Processing Magazine*, 25(2):83–91, March 2008. 9

[36] H. Eklund, A. Roos, and S.T. Eng. Rotation of laser beam polarization in acousto-optic devices. *Optical and Quantum Electronics*, 7(2):73–79, 1975. 7

[37] J.H. Everitt, D.E. Escobar, I. Cavazos, J.R. Noriega, and M.R. Davis. A three-camera multispectral digital video imaging system. *Remote Sensing of Environment*, 54(3):333 – 337, 1995. 7

[38] S. Farsiu, M. Elad, and P. Milanfar. Multiframe demosaicing and super-resolution of color images. *IEEE Transactions on Image Processing*, 15(1):141–159, January 2006. 71

[39] C. Fischer and I. Kakoulli. Multispectral and hyperspectral imaging technologies in conservation: current research and potential applications. *Reviews in Conservation*, 7:3–16, 2006. 5, 6

[40] Z. Frentress, L. C. Young, and H. D. Edwards. Field photometer with nine-element filter wheel. *Appl. Opt.*, 3(2):303–308, Feb 1964. 7

[41] Karl Pearson F.R.S. Liii. on lines and planes of closest fit to systems of points in space. *Philosophical Magazine Series 6*, 2(11):559–572, 1901. 101

[42] Y. Furukawa. Multi-view stereo: A tutorial. *Foundations and Trends in Computer Graphics and Vision*, 9(1-2), 2013.

[43] A. Garcia-Uribe, E.B. Smith, J. Zou, M. Duvic, V. Prieto, and L.V. Wang. *In-vivo* characterization of optical properties of pigmented skin lesions including melanoma using oblique incidence diffuse reflectance spectrometry. *Journal of Biomedical Optics*, 16(2):020501:1–3, 2011. 6

[44] J.M. Geary. *Introduction to Lens Design: With Practical ZEMAX Examples*. Willmann-Bell, 2002. 83, 85

[45] G.C. Giakos. Multifusion, multispectral, optical polarimetric imaging sensing principles. *IEEE Transactions on Instrumentation and Measurement*, 55(5):1628–1633, November 2006. 7

[46] H. Gong and M. Desvignes. Hemoglobin and melanin quantification of skin images. Technical Report 7325, Grenoble Institute of Tachnology, 2012. 6

[47] R.C. Gonzalez and R.E. Woods. *Digital Image Processing*. Prentice-Hall, Inc., Upper Saddle River, NJ, USA, 3rd edition, 2006. 29, 62, 79

[48] J.W. Goodman. *Introduction to Fourier Optics*. McGraw-Hill physical and quantum electronics series. Roberts & Company, 2005. 83

[49] A. Goshtasby. Image registration by local approximation methods. *Image and Vision Computing*, 6(4):255 – 261, 1988. 69

[50] J.E. Greivenkamp. *Field Guide to Geometrical Optics*. Field Guide Series. Society of Photo Optical, 2004. 85

[51] N. Gupta. Acousto-optic-tunable-filter-based spectropolarimetric imagers for medical diagnostic applications: instrument design point of view. *Journal of Biomedical Optics*, 10(5):051802, 2005. 7

[52] F.A. Haight. *Handbook of the Poisson distribution*. Publications in operations research. Wiley, 1967. 38

[53] J.V. Hajnal and D.L.G. Hill. *Medical Image Registration*. Biomedical Engineering. CRC Press, 2001. 62

[54] S. Harris and R. Wallace. Acousto-optic tunable filter. *Journal of Optical Society of America*, 59(6):744–747, June 1969. 7

[55] J. Hershey and Z. Zhang. Multispectral digital camera employing both visible light and non-visible light sensing on a single image sensor, 2008. US Patent 7/460,160. 8

[56] G.C. Holst. *CCD Arrays Cameras and Displays*. JCD Publishing, 1998. 34, 37, 43

[57] H. Huang, L. Liu, and M.O. Ngadi MO. Recent developments in hyperspectral imaging for assessment of food quality and safety. *Sensors*, 14(4):7248–7276, 2014. 128

[58] NASA IPAC. Herschel discovers ir light. http://coolcosmos.ipa.caltech.edu/cosmic-classroom/classroom-activities/herschel-bio.html, 2000. Accessed: May 23, 2013. 5

[59] J.E. Jackson. *A User's Guide to Principal Components*. Wiley Series in Probability and Statistics. Wiley, 2003. 101

[60] C. Jin, S.D. Normani, and M.B. Emelko. Surface roughness impacts on granular media filtration at favorable deposition conditions: Experiments and modeling. *Environmental Science & Technology*, 49(13):7879–7888, 2015. PMID: 26053116. 104

[61] I.T. Jolliffe. *Principal Component Analysis*. Springer Series in Statistics. Springer, 2002. 101

[62] L. Juan and O. Gwon. A comparison of SIFT, PCA-SIFT and SURF. *International Journal of Image Processing (IJIP)*, 3(4):143–152, 2009. 125

[63] M. Katz. *Introduction to Geometrical Optics*. World Scientific, 2002. 24

[64] F. Kazemzadeh, S. Haider, C. Jin, D.A. Clausi, and A. Wong. Concurrent fluorescence macro-imaging across multiple spectral regions in the visible and the near infrared. In *Proc. SPIE*, volume 9579, pages 957907–957907–7, 2015. 107

[65] F. Kazemzadeh, S.A. Haider, C. Scharfenberger, A. Wong, and D.A. Clausi. Multispectral stereoscopic imaging device: Simultaneous multiview imaging from the visible to the near-infrared. *Instrumentation and Measurement, IEEE Transactions on*, 63(7):1871–1873, July 2014. 10, 26, 114, 126

[66] F. Kazemzadeh, M.J. Shafiee, A. Wong, and D.A. Clausi. Reconstruction of compressive multispectral sensing data using a multilayered conditional random field approach. In Andrew G. Tescher, editor, *Proc. SPIE*, Applications of Digital Image Processing XXXVII, page 921712. SPIE, August 2014. 72, 78

[67] F. Kazemzadeh, A. Wong, and S.A. Haider. Imaging system and method for concurrent multiview multispectral polarimetric light-field high dynamic range imaging, August 2014. US patent 14/840,013, CA patent 2,902,675. 10, 123

[68] O. Khait, S. Smirnov, and C.D. Tran. Time-resolved multispectral imaging spectrometer. *Appl. Spectrosc.*, 54(12):1734–1742, Dec 2000. 7

[69] R. Kingslake. *Lens Design Fundamentals*. Academic Press, 1978. 85

[70] J.D. Lafferty, A. McCallum, and F.C.N. Pereira. Conditional random fields : Probabilistic models for segmenting and labeling sequence data. In *Proceedings of the Eighteenth International Conference on Machine Learning*, volume 2001 of *ICML '01*, pages 282–289. Morgan Kaufmann Publishers Inc., 2001. 78

[71] M. Laikin. *Lens Design, Fourth Edition*. Optical Science and Engineering. CRC Press, 2006. 85

[72] J.R. Lakowicz. *Principles of Fluorescence Spectroscopy*. Springer US, 2007. 32

[73] P.J. Lapray, X. Wang, J.B. Thomas, and P. Gouton. Multispectral filter arrays: Recent advances and practical implementation. *Sensors*, 14:21626–21659, 2014. 71

[74] H.C. Lee. *Introduction to Color Imaging Science*. Cambridge University Press, 2005. 18, 19

[75] E. Li, F. Kazemzadeh, M.J. Shafiee, and A. Wong. Sparse reconstruction of compressed sensing multispectral data using cross-spectral multi-layered conditional random field model. *IEEE Transactions on Image Processing*, Submitted. 72, 78

[76] E. Li, M.J. Shafiee, F. Kazemzadeh, and A. Wong. Sparse reconstruction of compressed sensing multispectral data using a cross-spectral multilayered conditional random field model. In *Proc. SPIE*, volume 9599 of *Applications of Digital Image Processing XXXVIII*, pages 959902–959902–8. SPIE, August 2015. 72, 78

[77] X. Li and S. Luo. A compressed sensing-based iterative algorithm for ct reconstruction and its possible application to phase contrast imaging. *Biomedical Engineering Online*, 2011. 9

[78] Y. Li, S. Zhou, G. Dong, M. Peng, L. Wondraczek, and J. Qiu. Anti-stokes fluorescent probe with incoherent excitation. *Nature Scientific Reports*, 4(4059), February 2014. 20

[79] Y.M. Lu, C. Fredembach, M. Vetterli, and S. Ssstrunk. Designing color filter arrays for the joint capture of visible and near-infrared images. In *Proceedings of the 16th IEEE International Conference on Image Processing (ICIP)*, page 37973800, Cairo, Africa, 2009. 9

[80] M. Lustig, D. Donoho, and J.M.Pauly. Sparse mri: The application of compressed sensing for rapid mr imaging. *Magnetic Resonance in Medicine*, 58(6):1182–1195, 2007. 9

[81] M. Lustig, D.L. Donoho, J.M. Santos, and J.M. Pauly. Compressed sensing mri. *Signal Processing Magazine, IEEE*, 25(2):72–82, March 2008. 9

[82] A. Madooei, M.S. Drew, M. Sadeghi, and S. Atkins. Intrinsic melanin and hemoglobin colour components for skin lesion malignancy detection. *Medical Image Computing and Computer Assisted Intervention*, 7510:315–322, 2012. 6

[83] D. Malacara. *Optical Shop Testing*. Wiley Series in Pure and Applied Optics. Wiley, 2007. 83

[84] A. Manakov, J.F. Restrepo, O. Klehm, R. Hegedüs, E. Eisemann, H.P. Seidel, and I. Ihrke. A reconfigurable camera add-on for high dynamic range, multispectral, polarization, and light-field imaging. *ACM Trans. Graph.*, 32(4):47:1–47:14, July 2013. 7

[85] A.A. Marghoob, L.D. Swindle, C. Z.M. Moricz, F.A.S. Negron, B. Slue, A.C. Halpern, and A.W. Kopf. Instruments and new technologies for the textitin-vivo diagnosis of melanom. *Journal of American Academy of Dermatology*, 49:777–797, 2003. 127

[86] M. McGuire, W. Matusik, H. Pfister, B. Chen, J.F. Hughes, and S.K. Nayar. Optical splitting trees for high-precision monocular imaging. *Computer Graphics and Applications, IEEE*, 27(2):32–42, March 2007. 7

[87] G. Mie. Beiträge zur Optik trüber Medien, speziell kolloidaler Metallösungen. *Annalen der Physik*, 330:377–445, 1908. 19

[88] M. Moncrieff, S. Cotton, E.Claridges, and P. Hall. Spectrophotometric intracutaneous analysis: A new technique for imaging pigmented skin lesions. *British Journal of Dermatology*, 146:448–457, 2002. 127

[89] P.P. Mondal and a. Diaspro. *Fundamentals of Fluorescence Microscopy: Exploring Life with Light*. SpringerLink : Bücher. Springer Netherlands, 2013. 18, 20, 83

[90] Y. Monno, S. Kikuchi, M. Tanaka, and M. Okutomi. A practical one-shot multispectral imaging system using a single image sensor. *Image Processing, IEEE Transactions on*, 24(10):3048–3059, Oct 2015. 8, 9

[91] Y. Murakami, M. Yamaguchi, and N. Ohyama. Hybrid-resolution multispectral imaging using color filter array. *Opt. Express*, 20(7):7173–7183, Mar 2012. 8

[92] D. Nakao, N. Tsumura, and Y. Miyake. Realtime multispectral image processing for mapping pigmentation in human skin. In *In Proceedings Ninth IS&T/SID Color Imaging Conference, IS&T*, pages 80–84, 1995. 6

[93] S.K. Nayar. Computational cameras. In *IAPR Conference on Machine Vision Applications*, Tokyo, Japan, 2007. 10

[94] H. Nyquist. Certain topics in telegraph transmission theory. *Transactions of the American Institute of Electrical Engineers*, 47(2):617–644, 1928. 9

[95] M. Okutomi and T. Kanade. A multiple-baseline stereo. *IEEE Trans. Pattern Anal. Mach. Intell.*, 15(4):353–363, April 1993. 126

[96] Edmund Optics. 10" white balance target, #58-611. Electronic, 2014. 34

[97] O.A. Osibote, R. Dendere, S. Krishnan, and T.S. Douglas. Automated focusing in bright-field microscopy for tuberculosis detection. journal of microscopy. *Journal of Microscopy*, 240(2):155–163., 2010. 85

[98] C. Palmer. *Diffraction Grating Handbook*. Newport Corporation, Rochester, NY, USA, 6th edition, 2005.

[99] H. Park and K.B. Crozier. Multispectral imaging with vertical silicon nanowires. *Nature Scientific Reports*, 3(2460), 2013. 8, 9

[100] H. Park, Y. Dan, K. Seo, Y.J. Yu, P.K. Duane, M. Wober, and K.B. Crozier. Filter-free image sensor pixels comprising silicon nanowires with selective color absorption. *Nano Letters*, 14(4):1804–1809, 2014. PMID: 24588103. 8, 9

[101] Polyscience. Fluoresbrite carboxylate color range kit ii. Electronic, 2015. 103, 104

[102] J. Qin, K. Chao, M.S. Kim, R. Lu, and T.F. Burks. Hyperspectral and multispectral imaging for evaluating food safety and quality. *Journal of Food Engineering*, 118(2):157 – 171, 2013. 128

[103] J.Y. Qu, H. Chang, and S. Xiong. Fluorescence spectral imaging for characterization of tissue based on multivariate statistical analysis. *Journal of the Optical Society of America - Optics Image Science and Vision*, 19:1823–1831, 2002.

[104] R. Ramanath, W.E. Snyder, G.L. Bilbro, and W.A. Sander. Robust multispectral imaging sensors for autonomous robots. Technical report, North Carolina State University, Raleigh, NC, USA, 2001. 8

[105] L.M. Reid, C.P. O'Donnell, and G. Downey. Recent technological advances for the determination of food authenticity. *Trends in Food Science & Technology*, 17(7):344 – 353, 2006. 107

[106] Y. Rivenson, A. Stern, and B. Javidi. Compressive fresnel holography. *Journal of Display Technology*, 6(10):506–509, Oct 2010. 9

[107] J. Ruettiger. Neutral density filters, May 19 1959. US Patent 2,887,010. 126

[108] D. Schneider. New camera chip captures only what it needs. *IEEE Spectrum*, 50:13–14, 2013. 9

[109] J.R. Schott. *Remote Sensing the Image Chain Approach*. Oxford University Press, second edition, 2007. 6

[110] G.A. Shaw and H.K. Burke. Spectral imaging for remote sensing. *Lincoln Labratory Journal*, 14(1):3–28, 2003. 5

[111] R. Shogenji, Y. Kitamura, K. Yamada, S. Miyatake, and J. Tanida. Multispectral imaging using compact compound optics. *Opt. Express*, 12(8):1643–1655, Apr 2004. 8

[112] B.A. Spiering. Multi spectral imaging system, 1999. US Patent 5/900,942. 7

[113] P. Stigell, K. Miyata, and M. Hauta-Kasari. Wiener estimation method in estimating of spectral reflectance from rgb images. *Pattern Recognition and Image Analysis*, 17(2):233–242, 2007. 127

[114] G.G. Stokes. On the change of refrangibility of light. *Philosophical Transactions of the Royal Society of London Series I*, 142:463–562, 1852. 20

[115] Stratasys. Fortus 380mc and fortus 450mc. Electronic, 2015. 60

[116] P. Suetens. *Fundamentals of Medical Imaging*. Cambridge University Press, second edition, 2009. Cambridge Books Online. 62, 79

[117] Thorlabs. Economy front surface mirrors. Electronic, 2015. 29

[118] R.Y. Tsai. Multiframe image point matching and 3-d surface reconstruction. *Pattern Analysis and Machine Intelligence, IEEE Transactions on*, PAMI-5(2):159–174, March 1983. 126

[119] L. Tsang, J.A. Kong, and K.H. Ding. *Scattering of Electromagnetic Waves, Theories and Applications*. A Wiley interscience publication. Wiley, 2000. 19

[120] L.J.P. van der Maaten and G.E. Hinton. Visualizing high-dimensional data using t-sne. *Journal of Machine Learning Research*, 9:2579–2605, 2008. 125

[121] L.J.P. van der Maaten, E.O. Postma, and H.J. van den Herik. Dimensionality reduction: A comparative review. Technical Report TiCC-TR 2009-005, Tilburg University Technical Report, 2009. 125

[122] E. Walmsley, C. Fletcher, and J. Delaney. Evaluation of system performance of near-infrared imaging devices. *Studies in Conservation*, 37(2):120–131, 1992. 119

[123] E. Walmsley, C. Metzger, J.K. Delaney, and C. Fletcher. Improved visualization of underdrawings with solid-state detectors operating in the infrared. *Studies in Conservation*, 39(4):217–231, 1994. 119

[124] L.V. Wang and H. Wu. *Biomedical Optics: Principles and Imaging*. Wiley, 2007. 18

[125] X. Wang, J.B. Thomas, J.Y. Hardeberg, and P. Gouton. Discrete wavelet transform based multispectral filter array demosaicing. In *Proceedings of the Colour and Visual Computing Symposium (CVCS)*, pages 1–6, Gjvik, Norway, 2013. 71

[126] Z. Wang, A.C. Bovik, H.R. Sheikh, and E.P. Simoncelli. Image quality assessment: from error visibility to structural similarity. *Image Processing, IEEE Transactions on*, 13(4):600–612, April 2004. 79, 81

[127] W.T. Welford. *Aberrations of Optical Systems*. Series in Optics and Optoelectronics. Taylor & Francis, 1986. 84

[128] B. Wilburn, N. Joshi, V. Vaish, E.V Talvala, E. Antunez, A. Barth, A. Adams, M. Horowitz, and M. Levoy. High performance imaging using large camera arrays. *ACM Trans. Graph.*, 24(3):765–776, July 2005. 7

[129] A. Wong, F. Kazemzadeh, C. Jin, and X.Y. Wang. Bayesian-based aberration correction and numerical diffraction for improved lensfree on-chip microscopy of biological specimens. *Opt. Lett.*, 40(10):2233–2236, May 2015. 87

[130] A. Wong, X.Y. Wang, and M. Gorbet. Bayesian-based deconvolution fluorescence microscopy using dynamically updated nonstationary expectation estimates. *Nature Scientific Reports*, 5:10849, 2015. 87

[131] J. Xing, C. Bravo, P.T. Jancsok, H. Ramon, and J.D. Bacrdemaeker. Detecting bruises on "Golden Delicious" apples using hyperspectral imaging with multiple wavebands. *Journal of Biosystems Engineering*, 90(1):27–36, 2005. 6

[132] M. Yamaguchi, M. Mitsui, Y. Murakami, H. Fukuda, N. Ohyama, and Y. Kubota. Multispectral color imaging for dermatology: Application in inflammatory and immunologic diseases. In *Imaging Science and Technology / Society of Imaging Display*, 13th Color Imaging Conference, 2005. 7

[133] C. Yang, J.K. Westbrook, C.P.C. Suh, D.E. Martin, W. C. Hoffmann, Y. Lan, B.K. Fritz, and J.A. Goolsby. An airborne multispectral imaging system based on two consumer-grade cameras for agricultural remote sensing. *Remote Sensing*, 6:5257–5278, 2014. 7

[134] L. Yaroslavsky. *Digital Holography and Digital Image Processing: Principles, Methods, Algorithms*. Springer US, 1 edition, 2004. 79

[135] F. Yasuma, T. Mitsunaga, D. Iso, and S.K. Nayar. Generalized assorted pixel camera: Postcapture control of resolution, dynamic range, and spectrum. *Image Processing, IEEE Transactions on*, 19(9):2241–2253, Sept 2010. 9

[136] T.T.E. Yeo, S.H. Ong, J. Sooriah, and R. Sinniah. Autofocusing for tissue microscopy. *Image and Vision Computing*, 11(10):629 – 639, 1993. 85

[137] D. Yi, L. Kong, F. Wang, F. Liu, S. Sprigle, and A. Adibi. Instrument an off-shelf ccd imaging sensor into a handheld multispectral video camera. *Photonics Technology Letters, IEEE*, 23(10):606–608, May 2011. 8, 9

[138] D. Yi, C. Wang, H. Qi, L. Kong, F. Wang, and A. Adibi. Real-time multispectral imager for home-based health care. *Biomedical Engineering, IEEE Transactions on*, 58(3):736–740, March 2011.

[139] D. Zhang, Z. Guo, G. Lu, , and W. Zuo. An online system of multispectral palmprint verification. *Instrumentation and Measurement, IEEE Transactions on*, 59(2):480–490, Feb 2010. 7

Appendices

Appendix A

The Design of the Monochrometer

A monochrometer is an optical device which allows for the mechanical selection of different narrowband wavelength portions of a spectrum. In this work the Czerny-Turner implementation of the monochrometer is used with a minor modification in which a spectrograph is used to disperse the light and a selection mechanism is then scanned across the focal plane of the spectrograph.

The spectrograph consists of an entrance aperture out of which broadband light diverges. The light then encounter a collimating element which transforms the diverging beam of light into planar wavefronts. This collimated beam encounters the grating which disperses the light into its wavelength constituents. The dispersed light beams, which are still collimated, are focused and therefore the spectrum of the light can be observed at the focal plane of the spectrometer.

A slit or a pinhole of appropriate width can be placed at the focal plane of the spectrograph and scanned across the focal plane to allow for the selection and admission of different wavelengths of light. It was postulated that the detector can be well characterized across the spectral region of interest in five nm steps. Therefore, the required spectral resolution is set to be 5 nm which corresponds to a dimensionless spectrometer resolving power of

$$R = \frac{\lambda_c}{d\lambda} = \frac{500}{3} = 167, \tag{A.1}$$

which is an extremely low resolving power and quite easily achievable. Working in this low

resolving power regime relaxes some of the constraints on the optical power of some of the components used in the system such as lenses and the grating.

A spectrograph is basically and imaging instrument which produces an image of the input aperture at various wavelengths ranges depending on the dispersing power of the grating which is determined by its groove density. Higher groove density means higher dispersing power. The spectral resolution limit of 5 nm means that each spectral spot imaged by the spectrograph should contain 5 nm of the spectrum. To this end a 300 ln/mm grating was chosen since it would work in both the visible and the NIR wavelength range. The size of the grating is 25 mm $\times$ 25 mm.

A fiber optics cable with a 50 μm core was used to deliver the broadband light to the spectrograph. The fiber optic has a numerical aperture (NA), diverging power, of 0.22 which corresponds to an f/# 2.27 using

$$f/\# = \frac{1}{2NA}. \tag{A.2}$$

The NA of the collimating lens should match the NA of the fiber for best performance and highest efficiency. The desired size of the collimated beam is 22 mm in diameter in order to avoid any edge effects on the grating and adhering to the clear aperture (90% of diameter) of the collimating lens making the diameter of the lens 25 mm. Since

$$f/\# = \frac{f_{collimator}}{D_{collimator}}, \tag{A.3}$$

where $f_{collimator}$ is the focal length and $D_{collimator}$ is the aperture of the collimating lens. The required focal length of the lens is determined to be 49.9 mm. To this end a lens of diameter 25 mm and focal length of 50 mm was chosen as the collimating optical element. In general, for best performance f/$\#_{collimator} \leq$ f/$\#_{fiber}$ which is satisfied in this case as 2 $\leq$ 2.27.

The grooves of the grating are blazed at 17.5° which means that the first order of dispersion will be about the blaze angle with maximum efficiency. Alternatively, the blaze angle describes the deflection angle of the optical axis after encountering the grating.

The grating equation that describes the dispersion of light is

$$j\lambda = d(sin\alpha + sin\beta), \tag{A.4}$$

where j is the diffraction order, d is the distance between two adjacent grooves, and α and β are the angles of the incident and outgoing beams with respect to the normal of the grating, respectively. In Littrow configuration $\alpha = \beta$ therefore the grating equation can be written as

$$Gj\lambda = 2sin\beta, \tag{A.5}$$

where G is the groove density or $\frac{1}{d}$.

The extent of the dispersion of light can be calculated using

$$\beta(\lambda) = sin^{-1}(\frac{\lambda}{d} - sin\alpha) \qquad for\ j = 1. \tag{A.6}$$

Operating in the visible range at 400 nm and 700 nm $\beta(\lambda)$ is 6.9° and 12.2° about α which would be equal to the blaze angle, respectively.

A focusing lens of diameter of 50 mm (45 mm clear aperture) was used to accommodate the extent of the dispersed beams. Based on the total dispersion angle of $\sim 6°$, it is calculated that the focusing lens has to be situated $\sim$ 400 mm from the grating if both of the blue and red ends of the spectrum are to fall within the clear aperture of the lens while being sufficiently separated.

The slit available for use in the scanning mechanism that would sample the focal plane of the spectrograph has a width of 75 μm. Therefore, the size of the spot of the focusing lens should correspond to the width of the slit. Therefore the inverse linear dispersion is

$$\left(\frac{dl}{d\lambda}\right)^{-1} = \frac{d\ cos\theta_B}{j\ f_{focus}}, \tag{A.7}$$

where θ_B is the Blaze angle and f_{focus} is the focal length of the focusing lens. The desired inverse linear dispersion is $\frac{5\ nm}{75\ \mu m}$. This then imposes the following constraint on the focal length of the focusing lens

$$f_{focus} > \frac{d\ cos\theta_B}{j}\left(\frac{dl}{d\lambda}\right). \tag{A.8}$$

Using the appropriate values of the design with the constraints imposed, it can be determined that for an optimal design of the spectrograph the focal length of the focusing

lens has to be $>$ 50 mm. Using the constraint of size of the scanning slit, the imposed focused spot size should be 75 μm and ergo the focal length of the focusing lens can be calculated using

$$f_{focus} = \frac{S_o}{S_i}\ f_{collimator}, \tag{A.9}$$

where S_o is the size of the focused spot, 75 μm, and S_i is the size of the input spot, 50 μm. Therefore, the focal length of the focusing lens can be calculated to be 75 mm which satisfies the constraint of being larger than 50 mm state above.

With the low dispersing power of the grating the angular dispersion of the spectrograph is

$$\frac{d\theta}{d\lambda} = \frac{57nm}{\circ}, \tag{A.10}$$

and therefore at the focal length of the lens, 75 mm, the linear dispersion can be calculated to be 0.05 nm/μm. With a spot size, or spatial resolution, of 75 μm the spectral resolution can be calculated to be 3.75 nm which exceeds the requirement of 5 nm / 75 μm spectral resolution.

The sampling slit is placed on a linear translation stage which enables the manual scanning of the focal plane of the spectrograph. Immediately behind the slit a 50/50 beamsplitting plate is placed that would transmit half of the light emerging from the slit and reflect the rest orthogonal to the direction of the propagation of the beam. The reflected portion of the beam is coupled into a off-the-shelf spectrometer which acts as the wavelength control unit. The transmitted half of the beam is available for imaging by the imaging device the detector of which is to be characterized.

Appendix B

The Usage of the Monochrometer

In this work the monochrometer is used in the characterization process of the spectral sensitivity of the color filter array of the detector of the imaging device. The imaging device is situated and fixed with respect to the slit of the monochrometer while observing the output of the slit through the beamsplitter. The front focal length of the lens of the imaging device is placed at infinity in an attempt to collimate the beam observed on the detector to maximize the area in which the slit is imaged and produce a uniform distribution of the light impinging on the detector pixels.

Using the linear stage, the slit is scanned from the blue end of the spectrum, produced by the spectrograph, to the red end. The emerging light from the slit is sampled by the spectrometer to ensure that the correct wavelength of light is being observed by the imaging device. An image is captured by the imaging device at each specific wavelength. The slit is moved along the focal plane of the spectrograph by a distance corresponding to a 5 nm wavelength shift as observed on the spectrometer and the image of the next monochromatic beam is captured. This process is repeated until the most red wavelength produced by the spectrograph is imaged.

Appendix C

List of Components

This is a list of the optical equipment used in the system presented in this work:

Part #	Manufacturer	Description
ME2S-P01	Thorlabs Inc.	Square Silver Mirror
FGS900S	Thorlabs Inc.	Bandpass Filter, 315 - 710 nm
FGL1000S	Thorlabs Inc.	Longpass Filter, 900 nm
43-953	Edmund Optics Inc.	Longpass Filter, 700 nm
69-221	Edmund Optics Inc.	850nm Dichroic Shortpass Filter
BPF-850-60	Kunming Yulong Co.	Bandpass Filter, 850 $\pm$ 15 nm